



January 2015

# Tracking Star Formation In Dwarf Cluster Galaxies

Cody Millard Rude

Follow this and additional works at: <https://commons.und.edu/theses>

---

## Recommended Citation

Rude, Cody Millard, "Tracking Star Formation In Dwarf Cluster Galaxies" (2015). *Theses and Dissertations*. 1829.  
<https://commons.und.edu/theses/1829>

This Dissertation is brought to you for free and open access by the Theses, Dissertations, and Senior Projects at UND Scholarly Commons. It has been accepted for inclusion in Theses and Dissertations by an authorized administrator of UND Scholarly Commons. For more information, please contact [zeinebyousif@library.und.edu](mailto:zeinebyousif@library.und.edu).

TRACKING STAR FORMATION IN DWARF CLUSTER GALAXIES

by

Cody Millard Rude

Bachelor of Science, University of Minnesota Duluth, 2009

A Dissertation

Submitted to the Graduate Faculty

of the

University of North Dakota

in partial fulfillment of the requirements

for the degree of

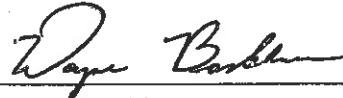
Doctor of Philosophy

Grand Forks, North Dakota

August

2015

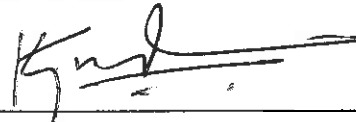
This dissertation, submitted by Cody Rude in partial fulfillment of the requirements for the Degree of Doctor of Philosophy from the University of North Dakota, has been read by the Faculty Advisory Committee under whom the work has been done and is hereby approved.



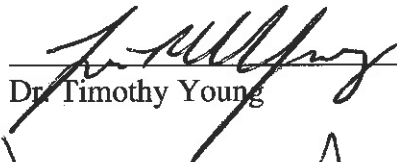
Dr. Wayne Barkhouse



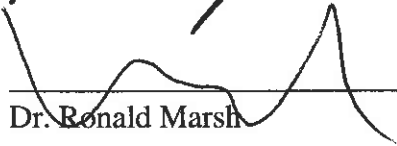
Dr. Ju Kim



Dr. Kanishka Marasinghe

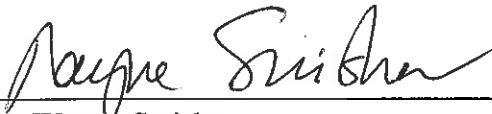


Dr. Timothy Young

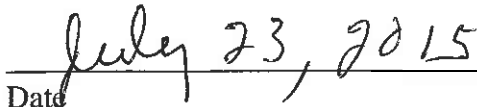


Dr. Ronald Marsh

This dissertation is being submitted by the appointed advisory committee as having met all of the requirements of the School of Graduate Studies at the University of North Dakota and is hereby approved.



Dr. Wayne Swisher,  
Dean of the School of Graduate Studies



Date

## PERMISSION

Title           Tracking Star Formation in Dwarf Cluster Galaxies

Department   Physics and Astrophysics

Degree         Doctor of Philosophy

In presenting this dissertation in partial fulfillment of the requirements for a graduate degree from the University of North Dakota, I agree that the library of this University shall make it freely available for inspection. I further agree that permission for extensive copying for scholarly purposes may be granted by the professor who supervised my dissertation work or, in their absence, by the chairperson of the department or the dean of the School of Graduate Studies. It is understood that any copying or publication or other use of this dissertation or part thereof for financial gain shall not be allowed without my written permission. It is also understood that due recognition shall be given to me and to the University of North Dakota in any scholarly use which may be made of any material in my dissertation.

Cody Rude  
06/25/2015

## TABLE OF CONTENTS

LIST OF FIGURES . . . . .	vi
LIST OF TABLES . . . . .	xii
ACKNOWLEDGMENTS . . . . .	xiii
ABSTRACT . . . . .	xiv
CHAPTER	
1. INTRODUCTION . . . . .	1
1.1 Galaxy Properties . . . . .	2
1.1.1 Morphology . . . . .	2
1.1.2 Dwarf Galaxies . . . . .	3
1.1.3 Star Formation . . . . .	5
1.2 Galaxies in Clusters . . . . .	6
1.3 Luminosity Function . . . . .	10
1.4 Recent Observations . . . . .	11
1.5 Motivation . . . . .	14
1.6 Outline . . . . .	15
2. TARGET CLUSTERS AND DATA REDUCTION . . . . .	17
2.1 Data . . . . .	17
2.2 Data Reduction . . . . .	34
2.2.1 Source Extractor . . . . .	34
2.2.2 Scamp . . . . .	35
2.2.3 SWarp . . . . .	36
2.2.4 Ellipse . . . . .	37
2.2.5 Picture Processing Package . . . . .	38
2.3 Additional Corrections . . . . .	45

3. CALIBRATION MEASUREMENTS . . . . .	48
3.1 Photometric Calibration . . . . .	48
3.2 Magnitude Limits . . . . .	50
3.3 Comparing Sizes and Magnitudes between Galaxy Clusters . . . . .	53
3.3.1 K-Correction . . . . .	53
3.3.2 Luminosity and Angular Size Distances . . . . .	55
3.4 Cluster Red-Sequence . . . . .	58
3.5 Cluster Richness . . . . .	62
3.6 Dynamical Radius . . . . .	75
4. RESULTS . . . . .	78
4.1 Combined Red-Sequence . . . . .	78
4.2 Luminosity Functions . . . . .	79
4.2.1 Measurement Uncertainties . . . . .	80
4.2.2 Combined Luminosity Function . . . . .	81
4.2.3 Fitting the Luminosity Function . . . . .	82
4.2.4 <i>r</i> -band Composite Luminosity Functions . . . . .	83
4.2.5 <i>u</i> -band Composite Luminosity Functions . . . . .	87
4.2.6 Possible Biases . . . . .	93
4.3 Dwarf-to-Giant Ratio . . . . .	100
4.4 Galaxy Color . . . . .	104
5. CLASH CLUSTERS . . . . .	109
5.1 Data . . . . .	109
5.2 Calibrations . . . . .	111
5.3 Results . . . . .	113
6. DISCUSSION . . . . .	120
6.1 Field and Cluster Luminosity Functions . . . . .	120
6.2 Comparisons of Dwarf-to-Giant Ratios . . . . .	123
6.3 Colors of Galaxies versus Density . . . . .	124
6.4 Butcher-Oemler Effect . . . . .	124
6.5 Star Formation in Dwarf Cluster Galaxies . . . . .	128
7. SUMMARY . . . . .	133
8. FUTURE WORK . . . . .	137
BIBLIOGRAPHY . . . . .	141

## LIST OF FIGURES

Figure		Page
1	The Hubble tuning fork diagram. . . . .	3
2	Morphological classification of dwarf galaxies. . . . .	5
3	Ultraviolet image of IC 3148 showing a tidal tail streaming to the lower left. . . . .	9
4	Luminosity functions for varying annuli of the Coma cluster. . . . .	13
5	Response of the Megacam filters. . . . .	18
6	Redshift of galaxies in the direction of cluster Abell 350. . . . .	18
7	<i>r</i> -band image of Abell 76. . . . .	20
8	Two possible central locations for the cluster are in the top and bottom of this <i>r</i> -band image of Abell 98. . . . .	21
9	Chandra x-ray data shows two extended sources in Abell 98. . . . .	21
10	<i>r</i> -band image of Abell 350. . . . .	22
11	<i>r</i> -band image of Abell 351. . . . .	23
12	<i>r</i> -band image of Abell 362. . . . .	24
13	<i>r</i> -band image of Abell 655. . . . .	25
14	<i>r</i> -band image of Abell 795. . . . .	26
15	<i>r</i> -band image of Abell 1920. . . . .	27
16	<i>r</i> -band image of Abell 1940. . . . .	28
17	<i>r</i> -band image of Abell 2100. . . . .	29
18	<i>r</i> -band image of Abell 2107. . . . .	30
19	<i>r</i> -band image of Abell 2147. . . . .	31
20	<i>r</i> -band image of Abell 2199. . . . .	32
21	<i>r</i> -band image of Abell 2688. . . . .	33
22	An example of deblending of a detection. . . . .	36

23	The eccentric anomaly for point P on the ellipse is given by E. . . . .	38
24	The top panel shows the original image, the middle figure shows the model determined by <code>Ellipse</code> , and the bottom panel shows the image after the model was subtracted from the original image. . . . .	39
25	$C_2$ classification versus instrumental magnitude. . . . .	43
26	Example of a k-d tree for two dimensions. . . . .	45
27	Sample pixels whose face shows the pixel counts. . . . .	46
28	Three star masks and a satellite trail mask are depicted in black. . . . .	47
29	Comparison of SDSS and CFHT $r$ -band magnitudes for Abell 1940 after the zeropoint was applied. . . . .	49
30	Comparison of SDSS and CFHT $u$ -band galaxy magnitudes for galaxies with errors $< 0.1$ magnitude located in the Abell 1940 image after the recalibrated zeropoint was applied. . . . .	50
31	Comparison of CFHTLS and SDSS $u$ -band galaxy magnitudes for galaxies with errors $< 0.1$ magnitude located in the Abell 1940 image. . . . .	51
32	Comparison of CFHTLS and CFHT $u$ -band galaxy magnitudes for galaxies with errors $< 0.1$ magnitude located in the Abell 1940 image. . . . .	52
33	Comparison of CFHTLS and CFHT $r$ -band galaxy magnitudes for galaxies with errors $< 0.1$ magnitude located in the Abell 1940 image. . . . .	53
34	Count of galaxies versus $r$ -band magnitude for Abell 1940. . . . .	54
35	The error in the color as a function of $r$ -band magnitude for Abell 1940. . . . .	55
36	The $r$ -band k-corrections for redshifts 0.03 (red solid line), 0.10 (green dotted line), and 0.18 (blue dot dashed line). . . . .	57
37	The $u$ -band k-corrections for redshifts 0.03 (red solid line), 0.10 (green dotted line), and 0.18 (blue dot dashed line). . . . .	58
38	Histogram of galaxy color for all galaxies brighter than the magnitude limit. 59	
39	Color-Magnitude diagram for Abell 1940. . . . .	60
40	Rectified color-magnitude diagram for Abell 1940. . . . .	63
41	Background corrected color histogram for Abell 76 for galaxies within $0.5 r_{200}$ of the cluster center. . . . .	63



42	Background corrected color histogram for Abell 98N for galaxies within $0.5 r_{200}$ of the cluster center. . . . .	64
43	Background corrected color histogram for Abell 98S for galaxies within $0.5 r_{200}$ of the cluster center. . . . .	64
44	Background corrected color histogram for Abell 350 for galaxies within $0.5 r_{200}$ of the cluster center. . . . .	65
45	Background corrected color histogram for Abell 351 for galaxies within $0.5 r_{200}$ of the cluster center. The small group at a rectified color of $-0.75$ is a lower redshift system. . . . .	65
46	Background corrected color histogram for Abell 362 for galaxies within $0.5 r_{200}$ of the cluster center. . . . .	66
47	Background corrected color histogram for Abell 655 for galaxies within $0.5 r_{200}$ of the cluster center. . . . .	66
48	Background corrected color histogram for Abell 795 for galaxies within $0.5 r_{200}$ of the cluster center. . . . .	67
49	Background corrected color histogram for Abell 1920 for galaxies within $0.5 r_{200}$ of the cluster center. . . . .	67
50	Background corrected color histogram for Abell 1940 for galaxies within $0.5 r_{200}$ of the cluster center. . . . .	68
51	Background corrected color histogram for Abell 2100 for galaxies within $0.5 r_{200}$ of the cluster center. . . . .	68
52	Background corrected color histogram for Abell 2107 for galaxies within $0.5 r_{200}$ of the cluster center. . . . .	69
53	Background corrected color histogram for Abell 2147 for galaxies within $0.5 r_{200}$ of the cluster center. . . . .	69
54	Background corrected color histogram for Abell 2199 for galaxies within $0.5 r_{200}$ of the cluster center. . . . .	70
55	Background corrected color histogram for Abell 2688 for galaxies within $0.5 r_{200}$ of the cluster center. The small group at a rectified color of $-0.6$ is a lower redshift system. . . . .	70
56	The $\lambda$ richness versus X-ray luminosity for Abell 76, 655, 795, 2107, 2199, and 2147. . . . .	75
57	A linear line was fit to $\log(\lambda)$ versus $\log(r_{200})$ to estimate $r_{200}$ for the rest of the sample. . . . .	77

58	Color magnitude diagram measured using cluster galaxies within $0.5 r/r_{200}$ .	79
59	The tails of the arrows show the starting point of a sample of 100 galaxies within $0.5 r/r_{200}$ of Abell 1940. . . . .	80
60	The $r$ -band LF for the $0.0 \leq r/r_{200} < 0.2$ region. . . . .	84
61	The $r$ -band LF for the $0.2 \leq r/r_{200} < 0.4$ region. . . . .	85
62	The $r$ -band LF for the $0.4 \leq r/r_{200} < 0.6$ region. . . . .	85
63	The $r$ -band LF for the $0.6 \leq r/r_{200} < 1.0$ region. . . . .	86
64	The $r$ -band LF for the $0.0 \leq r/r_{200} < 0.14$ region. . . . .	87
65	The $r$ -band LF for the $0.0 \leq r/r_{200} < 1.0$ region. . . . .	88
66	The $u$ -band LF for the $0.0 \leq r/r_{200} < 0.14$ region. . . . .	89
67	The $u$ -band LF for the $0.0 \leq r/r_{200} < 1.0$ region. . . . .	89
68	The response of the <i>GALAX</i> NUV filter (left) and the CFHT $u$ filter (right).	90
69	The $u$ -band LF for the $0.25 \leq r/r_{200} < 1.0$ region. . . . .	90
70	The $u$ -band LF for the $0.0 \leq r/r_{200} < 0.2$ region. . . . .	91
71	The $u$ -band LF for the $0.2 \leq r/r_{200} < 0.4$ region. . . . .	92
72	The $u$ -band LF for the $0.4 \leq r/r_{200} < 0.6$ region. . . . .	92
73	The $u$ -band LF for the $0.6 \leq r/r_{200} < 1.0$ region. . . . .	93
74	The $r$ -band LF for the $0.0 \leq r/r_{200} < 1.0$ region using original background (black dashes) and using background fields from the CFHTLS Deep Fields (red X's). . . . .	94
75	The $u$ -band luminosity function for the $0.0 \leq r/r_{200} < 1.0$ region using original background (black dashes) and using background fields from the CFHTLS Deep Fields (blue X's). . . . .	95
76	The uncertainty in magnitude for galaxies within $0.5 r/r_{200}$ . . . . .	96
77	The $u$ -band LF from the simulated galaxy cluster is shown as black dashed markers, and the LF after the simulated uncertainty was applied is shown as red X's. The simulated LF with errors was offset by 0.1 magnitudes for visualization purposes. . . . .	97
78	Galaxies in the volume B1 and B2 are projected onto volume A. . . . .	97
79	Schematic cross section of the Napkin Ring Problem. . . . .	98

80	The original and deprojected $r$ -band LFs for the $0.0 \leq r/r_{200} < 0.2$ region.	100
81	The original and deprojected $u$ -band LFs for the $0.0 \leq r/r_{200} < 0.2$ region.	100
82	The Schechter fits to the deprojected LFs in the $0.0 \leq r/r_{200} < 0.2$ region.	101
83	The $r$ -band (red dashes) and $u$ -band (blue X's) dwarf-to-giant ratios in four radial bins. . . . .	102
84	The ratio of $u$ -band giants to $r$ -band giants. . . . .	103
85	The ratio of $u$ -band dwarfs to $r$ -band dwarfs. . . . .	103
86	Histogram of dwarf galaxy color within $-19.5 \leq M_r < -17$ for the $0 \leq r/r_{200} < 0.2$ region. . . . .	104
87	Histogram of dwarf galaxy color within $-19.5 \leq M_r < -17$ for the $0.2 \leq r/r_{200} < 0.4$ region. . . . .	105
88	Histogram of dwarf galaxy color within $-19.5 \leq M_r < -17$ for the $0.4 \leq r/r_{200} < 0.6$ region. . . . .	105
89	Histogram of dwarf color within $-19.5 \leq M_r < -17$ for the $0.6 \leq r/r_{200} < 1.0$ region. . . . .	106
90	Histogram of giant galaxy color within $-26 \leq M_r < -19.5$ for the $0.6 \leq r/r_{200} < 1.0$ region. . . . .	106
91	Blue fraction versus cluster-centric radii for dwarfs (red dashed markers) and giants (black X symbols). . . . .	108
92	Response of F435W (black solid line), F475W (red dashed line) and SDSS $g$ -band (blue dot dashed line) filters. . . . .	111
93	Response of F775W (black solid line), F814W (red dashed line) and SDSS $i$ -band (blue dot dashed line) filters. . . . .	112
94	Absolute magnitude is plotted versus $z_{\text{galaxy}} - z_{\text{cluster}}$ for all clusters. . . . .	113
95	Estimated $k$ -corrections for passive galaxies in the $g$ -band (green solid line), star forming galaxies in the $g$ -band (blue dashed line), passive galaxies in the $i$ -band (red dotted line), and star forming galaxies in the $i$ -band (black dot dashed line). . . . .	114
96	Histogram of the color of all CLASH galaxies within $z \pm 0.1$ of a target cluster. . . . .	114
97	CLASH LF for the red-band fit with a single Schechter function. . . . .	115
98	CLASH LF for the blue-band fit with a single Schechter function. . . . .	115

99	CLASH LF for clusters $0.4 < z < 0.7$ using a cut of $z_{\text{cluster}} \pm 0.1$ (black dashed markers) and a cut of $z_{\text{cluster}} \pm 0.2$ (red x markers). . . . .	116
100	CLASH LF using a cut of $z_{\text{cluster}} \pm 0.1$ (black dashed markers) for all clusters and using a cut of $z_{\text{cluster}} \pm 0.2$ for clusters within $0.4 < z < 0.7$ (red x markers) . . . . .	117
101	Histogram of galaxy color within a magnitude range of $-19.91 \leq M_r < -17.41$ . . . . .	119
102	The $r$ -band LF for the $0.6 \leq r/r_{200} < 1.0$ region of the CFHT clusters (black markers) shown with the field LF from Blanton et al. (2001; solid red line). . . . .	121
103	The $u$ -band LF for the $0.6 \leq r/r_{200} < 1.0$ region of the CFHT clusters (black markers) shown with the field LF from Blanton et al. (2001; solid blue line). . . . .	121
104	$r$ -band (red solid line) and $u$ -band (blue dashed line) LFs for field galaxies from Blanton et al. (2001). . . . .	122
105	Galaxy color as a function of magnitude and local density. . . . .	125
106	Blue fraction versus redshift from the CNOC1 sample of clusters. . . . .	126
107	Blue fraction for three redshift bins measured from CFHT and CLASH clusters within $0.2 r/r_{200}$ . . . . .	127
108	Blue galaxy fraction for dwarfs (squares), giants (triangles), and dwarfs + giants (filled circle) reproduced from Barkhouse et al. (2009). . . . .	128
109	Blue fraction versus limiting magnitude cut for Cl 1604+42. . . . .	131
110	The passive (solid), quenching (dashed), and post starburst (dot-dashed) lines trace the change in $u - r$ of a simulated galaxy with time. . . . .	137
111	The passive (solid), quenching (dashed), and post starburst (dot-dashed) lines trace the change in the equivalent of $H\alpha$ and $u - r$ . . . . .	138
112	Specific star formation rates from Brinchmann et al. (2004) versus $u - r$ . . . . .	139

LIST OF TABLES

Table		Page
1	Target clusters selected for this project. . . . .	19
2	Magnitude zeropoints for target clusters. . . . .	50
3	Coefficients used in determining the $r$ -band k-corrections. . . . .	55
4	Coefficients used in determining the $u$ -band k-corrections. . . . .	56
5	Magnitude limits for the cluster sample. . . . .	59
6	Measured properties of target clusters. . . . .	61
7	Parameters derived from fitting Schechter functions in the $r$ -band. . . . .	84
8	Parameters derived from fitting Schechter functions in the $u$ -band. . . . .	91
9	CLASH target clusters. . . . .	110
10	Parameters derived from fitting a single Schechter function to the red and blue LF. . . . .	115

## ACKNOWLEDGMENTS

This dissertation would not be possible without the help and support of numerous people. I would like to express my gratitude to my adviser, Dr. Wayne Barkhouse, who was always available to discuss my research and provided invaluable guidance. My thanks to my committee members: Dr. Ju Kim, Dr. Kanishka Marasinghe, Dr. Timothy Young, and Dr. Ronald Marsh, for their advice and comments.

I have been very lucky to have incredible teachers that always provided help and encouragement. Many thanks to Allen Heine and Dr. Richard Gran, who have been indispensable to my success. Without their guidance, I would not have become a physicist.

I am very grateful to my friends and family, who have always been there for me.

My thanks to Madeline Shaft and Haylee Archer, who graciously checked object catalogs.

The majority of this work was completed using free (open source) software. I would be lost without the GNU operating system and GNU Emacs. For this research, I also used GNU Parallel.

To my parents, Dave and Tammy,  
who have always supported me.

## ABSTRACT

The evolution of galaxies in dense environments can be affected by close encounters with neighboring galaxies and interactions with the intracluster medium (ICM). Dwarf galaxies may be especially susceptible to these effects due to their low mass. The goal of my dissertation research is to look for signs of star formation in cluster dwarf galaxies by measuring and comparing the  $r$ - and  $u$ -band luminosity functions of 15 low redshift Abell galaxy clusters using archival data from the Canada-France-Hawaii Telescope (CFHT). Luminosity functions, dwarf-to-giant ratios, and blue fractions are measured in four cluster-centric annuli from stacked cluster data. To account for differences in cluster optical richness, each cluster is scaled according to  $r_{200}$ , where  $r_{200}$  is the radius of a sphere, centered on the cluster, whose average density is 200 times the critical density of the universe. The outer region of the cluster sample shows an increase in the faint-end slope of the  $u$ -band luminosity function relative to the  $r$ -band, indicating star formation in dwarf galaxies. The blue fraction for dwarf galaxies steadily rises with increasing cluster-centric radii. The change in the blue fraction of giant galaxies also increases, but at a lower rate. Additionally, the inner regions of clusters ranging from  $0.185 < z < 0.7$  from the “Cluster Lensing and Supernova survey with Hubble (CLASH)” are used to generate blue- and red-band luminosity functions, dwarf-to-giant ratios, and blue fractions. Comparisons of the inner region of the CLASH and CFHT clusters show an increase in the blue fraction of dwarf galaxies with redshift that is not present in giant galaxies.



## CHAPTER 1

### INTRODUCTION

One of the main goals of extragalactic astronomy is to understand how galaxies evolve. The evolutionary process is very slow, relative to human timescales, and so different galaxies are studied at various stages of their lives in order to piece together their evolution. As a result, our understanding of galaxies has gone hand-in-hand with increases in telescope aperture, which allows looking further back in the universe's history.

Although once dubbed "island universes," galaxies do not all live in isolation. The first evidence that some galaxies cluster together was found when Charles Messier cataloged bright nebulae in the 1700's, long before they were known to be external galaxies beyond the Milky Way. Due to the high density of galaxies and the pressure of an intracluster medium (ICM) of hot gas, galaxy clusters play a vital role in understanding environmental effects on galaxy evolution. In addition, galaxy clusters are used as laboratories to study physics on a grand scale. The Coma cluster provided the first evidence that the mass of the universe is primarily made up of dark matter that does not directly interact with light (Zwicky, 1933).

It wasn't until the 1920's, using photographic plates, that direct evidence was obtained that some of the fuzzy objects in Messier's catalog are galaxies like our own (Hubble, 1925). Today, CCD cameras attached to telescopes with mirrors that are meters in diameter and can take hundreds of gigabytes of data in a single night over a large area.

In order to understand all of these data, automated tools are used to detect and measure the properties of astronomical objects.

Under the  $\Lambda$ -Cold-Dark-Matter model of our universe ( $\Lambda$ CDM), objects are initially built up around quantum fluctuations in an otherwise smooth distribution of dark matter. The dark matter coalesces around the fluctuations via gravity, building up mass and attracting baryonic matter. Larger structures, such as galaxy filaments and clusters, are built up from collections of galaxies. This type of structure formation is known as the hierarchical (bottom-up) scenario, where larger structures are built from smaller ones (Kravtsov & Borgani, 2012). Although most of the mass in a galaxy is composed of dark matter, the primary way of understanding galaxy evolution is by observing the normal matter; stars, gas, and dust.

## **1.1 Galaxy Properties**

### ***1.1.1 Morphology***

The Hubble tuning fork diagram, with elliptical galaxies as the handle of a fork which splits into barred and unbarred spiral galaxies (Fig. 1), successfully catalogs 90% of nearby luminous galaxies (Abraham & van den Bergh, 2001). At higher redshifts, as seen in the Hubble Deep Fields where the *Hubble Space Telescope* (HST) took long exposures of a seemingly empty part of the sky (Williams et al., 1996), the number of merging and peculiar galaxies that aren't classified by the Hubble tuning fork diagram increases to  $\approx 30\%$ . Additionally, grand design and barred spiral galaxies are rare at high redshift (Abraham & van den Bergh, 2001).

It has long been known that elliptical galaxies are more commonly found in clusters, and that spirals dominate the field (Hubble & Humason, 1931). This relationship

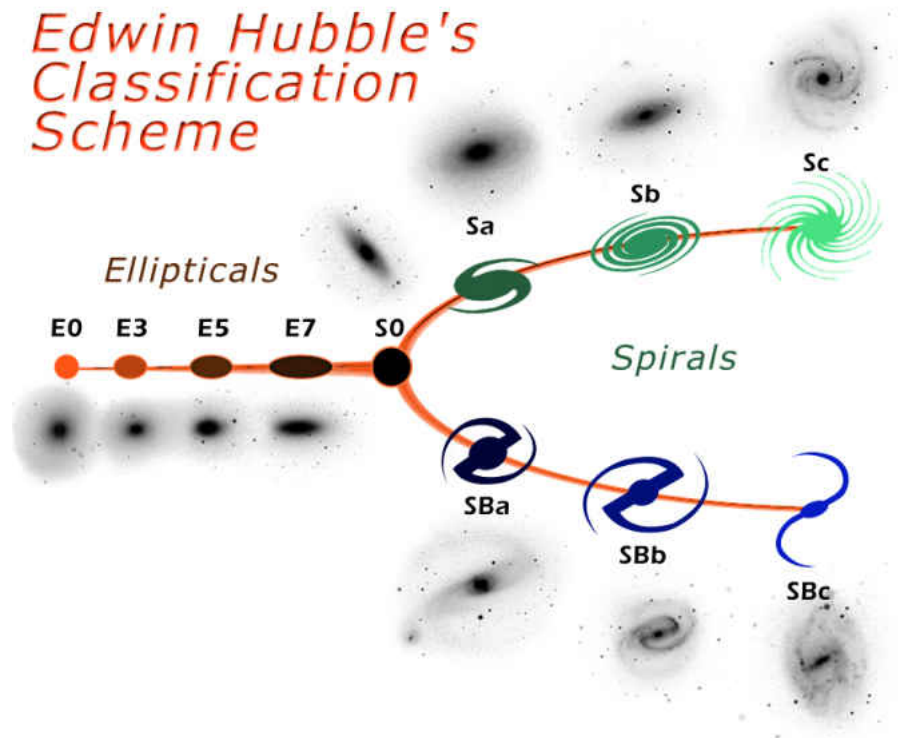


Figure 1. The Hubble tuning fork diagram. This graphic was created by the Space Telescope Science Institute for NASA.

was shown to be a function of local galaxy density, and is known as the morphology-density relationship (Dressler, 1980). At a redshift of  $\sim 0.5$ , the relationship breaks down in irregular clusters, and is only valid in massive concentrated clusters (Dressler et al., 1997).

### 1.1.2 Dwarf Galaxies

While luminous galaxies are classified according to the Hubble tuning fork diagram, faint galaxies are not. Sandage & Binggeli (1984) made additions to the diagram to account for dwarf galaxies using observations of the Virgo cluster. The diagram reproduced in Fig. 2 shows the additional classifications relative to the original Hubble sequence.

Dwarf elliptical galaxies (dE) are considered a continuation of the giant elliptical type. They are the most common type of galaxy in the local universe (Ferguson &

Binggeli, 1994). dEs have smooth brightness profiles (the change in surface brightness with radius), as opposed to dwarf irregulars. Unlike their brighter giant elliptical counterparts, dE's have a more exponential brightness profile. Normal elliptical galaxies have a de Vaucouleurs profile, where the light falls off as  $r^{(1/4)}$ . Additionally, a dE may contain a nucleus.

dE galaxies are not only very numerous, but they are also strongly clustered (Vader & Sandage, 1991). Additionally, fainter dEs and brighter dE's with a nucleus ( $M_{BT} > -14.2$ ) are more common and pervade dense regions, while the brighter dE's without a nucleus are typically found in less-dense regions (Ferguson & Sandage, 1989).

Sandage & Binggeli (1984) also introduced the dS0 galaxy type, which is the dwarf version of an S0 galaxy. Morphologically, a S0 galaxy is between the ellipticals and spirals. They have a nucleus and a disk, but contain no spiral structure. Similarly, dS0s are similar to dwarf elliptical galaxies that contain a disk. They may also contain a visible bar, or possess a brightness profile that is composed of two components, i.e. the brightness profile is not well-fit with a single Sérsic function. A Sérsic function is a generalized de Vaucouleurs profile where the surface brightness decreases by  $r^{(1/n)}$ . dS0s are much less common than the dE type. To make matters more complicated, deep observations of some dwarf elliptical galaxies reveal disk-like structures (Lisker et al., 2006).

Late type dwarf galaxies, also known as dwarf irregulars or dIs, are an extension of the sequence of spiral galaxies (Fig. 2). Late type dwarfs are separated from giant spiral galaxies by their lack of spiral arms. dI galaxies also contain clumpy regions of active star formation.

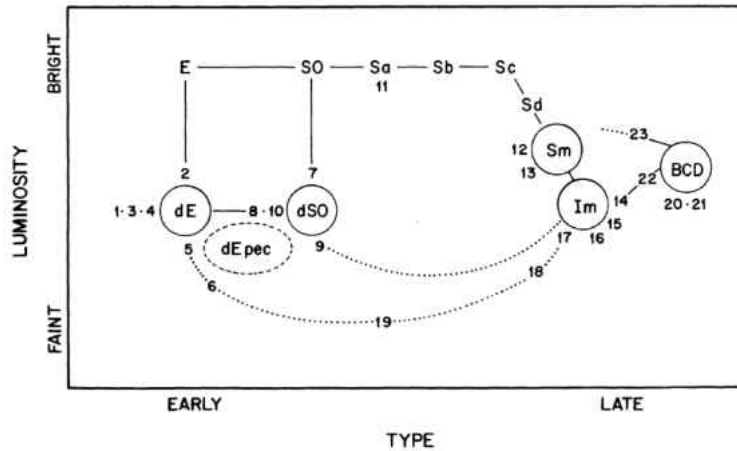


Figure 2. Morphological classification of dwarf galaxies. The Hubble tuning fork diagram has been compressed to a single line for late type galaxies. Dotted lines indicate possible connections. Dwarf irregulars are of type Im on the chart. Reproduced from Sandage & Binggeli (1984).

### 1.1.3 Star Formation

Stars are formed in the collapse of hydrogen gas (McKee & Ostriker, 2007). The gas can be affected by shock waves from supernova explosions, or by gravitational tidal forces caused by encounters with other galaxies. Stars formed in clusters in a collapsing gas cloud can drift away from the cluster over time. As a result, star formation is often associated with clumpy stellar distributions. After time, the stellar distribution smooths out, and the clumpy structure dissipates.

Galaxy morphology has been shown to correlate with star formation history (Kennicutt, 1998). Elliptical galaxies typically have little gas and dust, and host an old population of stars. The disks of spiral galaxies host sites of active star formation. Early type spiral galaxies are host to a nuclei whose stellar population resembles that of elliptical galaxies. Later type spirals, however, can host psuedo bulges whose stellar population is more disk-like (Kormendy & Kennicutt, 2004). Due to the correlation between stellar history and morphological type, it should come as no surprise that there is

a star-formation-density relationship (Quadri et al., 2012) similar to the density-morphology relationship.

Hot, massive stars live short lives, on the order of a few million years, and emit light primarily in the ultraviolet, while smaller cool stars have long lives, and emit light primarily in the infrared (Carroll & Ostlie, 2006). Blue colors generally indicate recent star formation, as the hot O- and B-type stars dominate the light. Color, then, can be used to separate galaxies into star forming and non-star forming populations (Kennicutt, 1998). The age of a stellar population is not the only factor in determining galaxy color. Stellar metallicity, which describes the relative abundance of elements heavier than helium, also plays a role. Stars with lower metallicity are hotter and bluer than their higher metal counterparts (Bruzual & Charlot, 2003; Tinsley, 1980).

## **1.2 Galaxies in Clusters**

All galaxy clusters discovered thus far contain a population of passively evolving galaxies that adhere to a tight linear color magnitude relation (López-Cruz et al., 2004). Since the population of galaxies are red, this is referred to as the red-sequence.

One feature of the red-sequence is its downward slope (e.g. fainter galaxies on the red-sequence are bluer than brighter ones). Since both a younger stellar age and lower metallicity can cause galaxies to be bluer, Kodama & Arimoto (1997) used population synthesis models to determine that metallicity, and not differences in stellar age, causes this effect. One possible explanation for a decrease in metallicity with decreasing mass is that smaller galaxies lose their enriched interstellar material from winds generated by supernova (Carlberg, 1984).

Blueward of the red-sequence on a color-magnitude diagram (CMD) are the more

active star forming galaxies. They do not form a tight linear sequence, but form a “blue cloud” on the CMD. Recently, ultraviolet data has revealed a population of galaxies between the red-sequence and the blue cloud, which is referred to as the green valley (Salim, 2014). It has been suggested that external processes are transitioning these galaxies from the blue cloud to the red-sequence.

Butcher & Oemler (1978) showed that the fraction of blue spiral galaxies in two clusters at a redshift of 0.39 and 0.46 was higher than in the Coma cluster. More recently, Ellingson et al. (2001) used a sample of 15 rich galaxy clusters with redshifts between 0.18 and 0.55 to show a significant increase in the blue fraction with increasing redshift of galaxies beyond  $0.5 r_{200}$ , where  $r_{200}$  is the radius of a sphere centered on the cluster whose density is 200 times the critical density of the universe (Cole & Lacey, 1996). This increase in the fraction of blue galaxies with increasing redshift is known as the Butcher-Oemler Effect.

Another important class of galaxies are k+a type, whose name comes from the fact that their continuum is dominated by K type stars, but have absorption features from A type stars. They are associated with a burst of star formation  $\approx 10^9$  years prior to observation (Dressler & Gunn, 1983). These post-starburst galaxies appear to be more common at moderate redshifts ( $\approx 0.5$ ) where they are an order of magnitude more abundant than in the field at a similar redshift (Dressler et al., 1999). In the local universe, luminous k+a galaxies appear to be rare. In clusters, k+a galaxies are also found to be less centrally concentrated than passive galaxies, though more so than star forming galaxies.

Galaxy clusters are also host to a hot intracluster medium (ICM). The gas in a cluster has a temperature around  $\approx 7 \times 10^7 K$ , and has an electron density of  $\approx 10^{-3} cm^{-3}$

(Forman & Jones, 1982).

Ram pressure stripping is the removal of gas from a galaxy due to the pressure of the ICM on the gas in the galaxy. Gunn & Gott (1972) estimated that a typical large spiral moving at a velocity of 1700 km/s will be stripped of gas if the number density of the ICM exceeds  $5 \times 10^{-4}$  atoms/cm<sup>3</sup>. Galaxies that fall into clusters are expected to be star forming, and ram pressure can truncate star formation. Thus, only galaxies that have recently entered the cluster will be blue. The Butcher-Oemler effect could be due to the reduction in the number of galaxies falling into the cluster with decreasing redshift.

This scenario has been backed up by numerical simulations of infalling spiral galaxies in the Coma cluster. Using a galaxy model similar to the Andromeda Galaxy, Quilis et al. (2000) found that the diffuse HI gas can be completely stripped on timescales of 100 million years for an ICM similar to the Coma cluster. These results hold even if the galaxy is inclined 20 degrees with respect to the direction of motion.

The most common type of galaxy in a cluster is the dE. dEs are rarely, if ever, found in isolation. dIs, however, are found both in isolation and in clusters, though less so in clusters. It was proposed by Lin & Faber (1983) that ram pressure stripping could turn dwarf irregulars into dwarf spheroidals by the removal of gas from dI galaxies. Observations of the dI galaxy IC 3418 in the nearby Virgo cluster has revealed a stream of material coming out of the galaxy due to ram pressure stripping (Kenney et al., 2014). In Fig. 3, an image of IC 3418 is shown in the near ultraviolet. The galaxy experienced a burst of star formation followed by truncation  $\approx 300$  Myr ago.

Another physical mechanism expected to be important in the cluster environment is galaxy harassment. The dense cluster environment provides many opportunities for





Figure 3. Ultraviolet image of IC 3148 showing a tidal tail streaming to the lower left. Reproduced from Hester et al. (2010).

galaxy interaction. Due to the high speed of galaxies in a cluster (velocity dispersion of  $\approx 500 - 1000$  km/s; Struble & Rood, 1999) mergers of galaxies is unlikely, and instead galaxies will experience repeated interactions with high speed neighbors. Moore et al. (1996) ran simulations of a Sd galaxy interacting with larger galaxies, and showed that this type of harassment can turn an Sd into a dE galaxy. This has been proposed as one origin of dE galaxies. At a redshift of  $\approx 0.4$ , galaxies fainter than  $M_* - 2$  (where  $M_*$  is the characteristic turnover of the galaxy luminosity function, see Sec. 1.3) are primarily Sd galaxies, i.e. faint spiral galaxies with essentially no bulge.

A third environmental effect is galaxy starvation, or strangulation (Larson et al., 1980). The star formation rate in spiral galaxies is large enough to deplete all the gas in their disk in  $\approx 2$  Gyr. It has been proposed that spiral galaxies are embedded in an extended gas halo which feeds the disk. Galaxy starvation, then, is the removal of this gas.

Once the gas in the disk runs out, star formation ceases. This effect, along with ram pressure stripping, has been seen in simulations of cluster galaxies (Tonnesen et al., 2007).

Dwarf galaxies are particularly important for understanding the physical processes involved in galaxy clusters. Not only are dE galaxies the most numerous type of galaxy in the universe, their low mass makes them more susceptible to external influences. McGee et al. (2009) used a simulation to show that massive galaxies tend to fall into a cluster as part of a galaxy group, which means massive galaxies can be preprocessed in the group environment before they enter the cluster. Lower mass galaxies, however, can enter the cluster environment in isolation, which can yield a cleaner look at the environmental processes in clusters while not being contaminated by processes at work in the group environment.

### **1.3 Luminosity Function**

Along with color, the probability function of galaxy brightness in clusters and in the field is of interest. Once posited that the luminosity function shape is universal (Schechter, 1976), it has been shown that the luminosity function differs for the various morphological types of galaxies (Binggeli et al., 1988). Since the relative distribution of morphological galaxy type depends on density, the resulting luminosity functions must also be different for field and cluster galaxies (i.e. low versus high density environments). In recent times, luminosity functions are typically measured for either all galaxy types or galaxies selected by color, due to difficulties with classifying faint galaxies.

The luminosity function for a cluster is typically characterized by two Schechter

functions (Schechter, 1976; Barkhouse et al., 2007). A Schechter function is given by

$$n(M)dM = kN^* e^{k(\alpha+1)(M^*-M) - \exp[k(M^*-M)]} dM, \quad (1.1)$$

where  $k = 0.4 \ln 10$ . One Schechter function is fit to the giant galaxy population and one is fit to the dwarf population. The shape of the luminosity function is determined by two main parameters;  $M^*$  and  $\alpha$ . The characteristic magnitude,  $M^*$ , sets where the slope changes dramatically for bright galaxies, and  $\alpha$  characterizes the faint-end slope.

The faint-end of the luminosity function in the cluster environment varies as a function of cluster-centric radii, as was shown by Barkhouse et al. (2007) on a stacked sample of 57 Abell galaxy clusters. Due to projection effects, luminosity functions must be corrected for background and foreground galaxies that appear to be in the cluster. Typically a background field is used to estimate statistically the number of non-cluster galaxies in front of and behind the cluster at the expense of increased scatter (compared to using redshift measurements to determine cluster membership). Due to the small number of net galaxies per luminosity bin, it is necessary to stack multiple cluster luminosity functions to get statistically robust results.

#### 1.4 Recent Observations

Martin et al. (2000) used a narrow band filter centered on an [OII] emission line in order to measure the star formation rate of galaxies in Abell 851 ( $z = 0.41$ ). They found a population of star forming galaxies, which are most likely dwarf galaxies undergoing a burst of star formation. Their star formation rate, however, is lower than those of field galaxies, indicating that possible environmental effects are limiting their star formation.

They compared a population of star bursting galaxies to Virgo cluster galaxies and found that the population of star bursting galaxies was not large enough to account for all of the dEs found in local clusters. This implies that the dwarf population in local clusters cannot be totally described by the population of star bursting galaxies at moderate redshifts.

In the local universe, Haines et al. (2006) used spectroscopy from the Sloan Digital Sky Survey Data Release 4 (SDSS DR4) to measure the mean stellar age of galaxies in Abell 2199 ( $z = 0.03$ ). They found that the fraction of passive galaxies increased with local density for both giants and dwarfs.

Beijersbergen et al. (2002) measured deep luminosity functions in various cluster-centric regions centered on the Coma cluster. They constructed luminosity functions from data in three different bands for each region. In the outer region of the cluster they found an increase in the faint-end of the  $U$ -band luminosity function relative to the  $r$ -band (Fig. 4).

One possible cause of this increase in slope is enhanced star formation in dwarf galaxies. Enhanced star formation will brighten dwarf galaxies in the  $u$ -band, while leaving the  $r$ -band magnitudes relatively unchanged. Fainter galaxies, which would normally be too faint to be detected, may pile up at the faint-end of the luminosity function, resulting in an increased slope.

Popesso et al. (2006) measured  $g$ ,  $r$ ,  $i$ ,  $z$ -band luminosity functions from a composite sample of nearby galaxy clusters in SDSS. They split their sample into red and blue galaxies using a  $u-r$  color cut. They report a flattening of the faint-end of the luminosity function in the central region, indicating a disruption of dwarf galaxies. Additionally, they found that the number of blue dwarf galaxies relative to red dwarfs

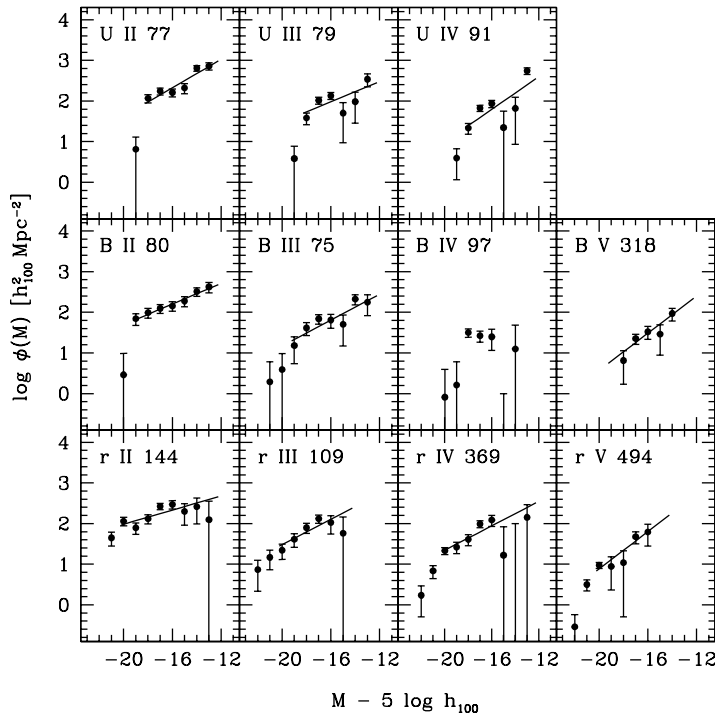


Figure 4. Luminosity functions for varying annuli of the Coma cluster. There is an increase in the slope at the faint-end in the  $U$ -band relative to the  $r$ -band in area IV, which is the outer region of the cluster. Reproduced from Beijersbergen et al. (2002).

increases with increasing cluster-centric radius.

The dwarf-to-giant ratio (DGR), which is the ratio of the number of dwarf galaxies to the number of giant galaxies, is another method of studying the cluster population.

Barkhouse et al. (2009) saw an increase in the DGR for red, and red + blue galaxy populations with increasing cluster-centric radius. The DGR for blue galaxies was mostly constant with respect to radius. Barkhouse et al. also computed the blue fraction of dwarf galaxies as a function of cluster-centric radius and found a dip in the blue fraction in the very core of the cluster. Like Popesso et al. (2006), they observed an increase in the blue fraction of galaxies with increasing radius.

Hammer et al. (2012) constructed deep ultraviolet luminosity functions of the

Coma cluster using observations from the *GALEX* space telescope. They found that the luminosity function of star forming dwarf galaxies falls off between  $-14 < M_{uv} < -12$ . This turnover of the luminosity function is not seen in the field, and so it may indicate that environmental effects are truncating star formation.

## 1.5 Motivation

Due to their low mass, dwarf galaxies can be used to probe environmental effects of galaxy clusters. As dwarf galaxies fall into the cluster environment they may experience ram pressure and galaxy harassment. These mechanisms can influence star formation and galaxy morphology. Ram pressure from the ICM could: 1) completely remove the gas in a dwarf galaxy, stifling star formation, 2) compress the gas in the galaxy, enhancing star formation, or 3) compress and then remove the gas resulting in a burst and then truncation of star formation. Star formation close to the cluster center would indicate ram pressure stripping since the ICM density is highest in the core. Alternatively, star formation in the outer region of the cluster would imply galaxy harassment, as the ICM is less dense in this region.

While star formation activity in clusters is lower in the local universe, it is still present today. In the southwest corner of the Coma cluster, for example,  $\approx 29\%$  of galaxies surveyed were post-starburst (Caldwell & Rose, 1997). A sample of nine low luminosity systems in the Coma cluster had a wide range of star formation histories, with two of them being post-starburst (Caldwell & Rose, 1998).

Although spectroscopy is the most direct way of measuring star formation rates, it is difficult to measure spectra of a large sample of faint galaxies. By utilizing photometric color as an indicator of star formation activity, it is possible to use archival data to study

the dwarf population of Abell clusters.

## 1.6 Outline

Although there have been previous studies investigating star formation and luminosity functions of galaxy clusters, they typically use a small sample of clusters (Beijersbergen et al., 2002; Haines et al., 2006), or don't probe deep into the dwarfs (Barkhouse et al., 2007). In the case of Popesso et al. (2006), they utilize SDSS  $u$ -band to make color cuts using  $u-r$  color. Although they use a large sample size, the  $u$ -band in SDSS suffers from red light leak (Kowalski et al., 2009), thus degrading galaxy magnitudes. Additionally, SDSS is a large survey using a 2-meter class telescope with 54 second exposures per image, which doesn't go as deep as targeted observations, forcing the use of only the lowest redshift clusters for measuring the dwarf population. By looking at a sample of galaxy clusters using deep images from a 4-meter class telescope, clusters out to a redshift of  $\approx 0.20$  can be used.

My research goal is to look for evidence of enhanced star formation in infalling cluster dwarf galaxies. A sample of 15 Abell galaxy clusters with a redshift range of 0.03 to 0.18 from the Canada-France-Hawaii Telescope (CFHT) is reduced and analyzed. The dispersion of the red-sequence for the cluster sample is measured and used to cut background objects from subsequent analysis. Background corrected luminosity functions in the  $r$ - and  $u$ -band are constructed for different cluster-centric radii and compared. For the higher redshift clusters in the sample, the region surrounding the cluster is used as the background field to better estimate the effects of large scale structure. Evidence of enhancement/quenching in the outer regions would then imply galaxy harassment or starvation. Additional metrics, such as the DGRs and the blue fractions are also presented.

Additionally, higher redshift galaxy clusters ( $0.185 < z < 0.7$ ) observed in the “Cluster Lensing and Supernova survey with Hubble” (Postman et al., 2012) are analyzed and compared to the lower redshift clusters.

An increase in the slope of the  $u$ -band luminosity function relative to the  $r$ -band indicates enhanced star formation. Combining data from several galaxy clusters provides the necessary statistics to compare the different regions of the cluster sample. The resulting analysis is compared with field luminosity functions to see if star formation is enhanced or quenched.

This thesis is organized into eight chapters. The target clusters and data reductions are described in Chapter 2. Calibration measurements are presented in Chapter 3, and the analysis of the 15 Abell clusters are given in Chapter 4. The description and measurements of the CLASH clusters are presented in Chapter 5. The results are discussed in Chapter 6, and the thesis is summarized in Chapter 7. Finally, future work is described in Chapter 8. Unless otherwise indicated, I adopt a cosmology of  $\Omega_m = 0.3$ ,  $\Omega_\Lambda = 0.7$ , and  $H_0 = 70 \text{ km s}^{-1} \text{ Mpc}^{-1}$ .



## CHAPTER 2

### TARGET CLUSTERS AND DATA REDUCTION

#### 2.1 Data

The data for this project comes from the archives of the Canada-France-Hawaii 3.6 meter telescope. Many of these target clusters were imaged as part of an accepted observing proposal from Barkhouse et al. to look for star formation in dwarf cluster galaxies. All of the observations were taken using the Megacam CCD mosaic camera. Megacam has 36 chips, each with 2048x4612 pixels. Galaxy clusters were selected from the catalog created by Abell et al. (1989). All of the clusters have  $u$ - and  $r$ -band (Fig. 5) data available in the archives with an adequate exposure time, and a redshift between 0.03 and 0.185. This ensures that the cluster would fit within the one square degree field of view of the telescope and detector, and that the dwarf population was observable. All of the clusters also overlap with SDSS for calibration purposes. Finally, each cluster has at least ten red-sequence galaxies within one Mpc of the cluster center. This ensures that each cluster is not two separate groups at different redshifts. An overview of the data can be found in Table 1.

All redshifts, except Abell 350, were obtained from the NASA Extragalactic Database.<sup>1</sup> The redshift for Abell 350 was estimated from the median value of photometric redshifts of galaxies that were between  $z=0.14$  and  $z=0.18$  (Fig. 6).

---

<sup>1</sup><http://ned.ipac.caltech.edu/>

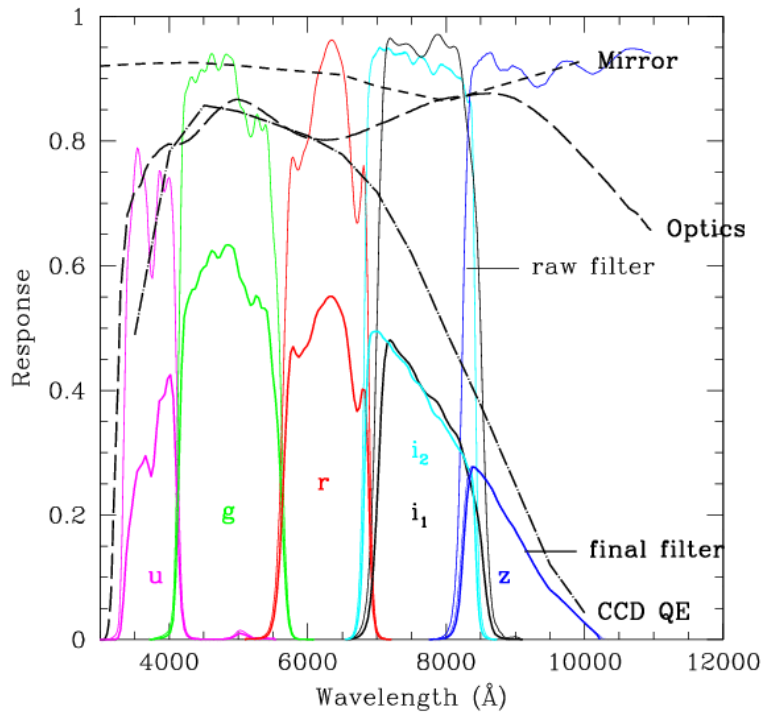


Figure 5. Response of the Megacam filters. Reproduced from the Canadian Astronomy Data Centre (2015).

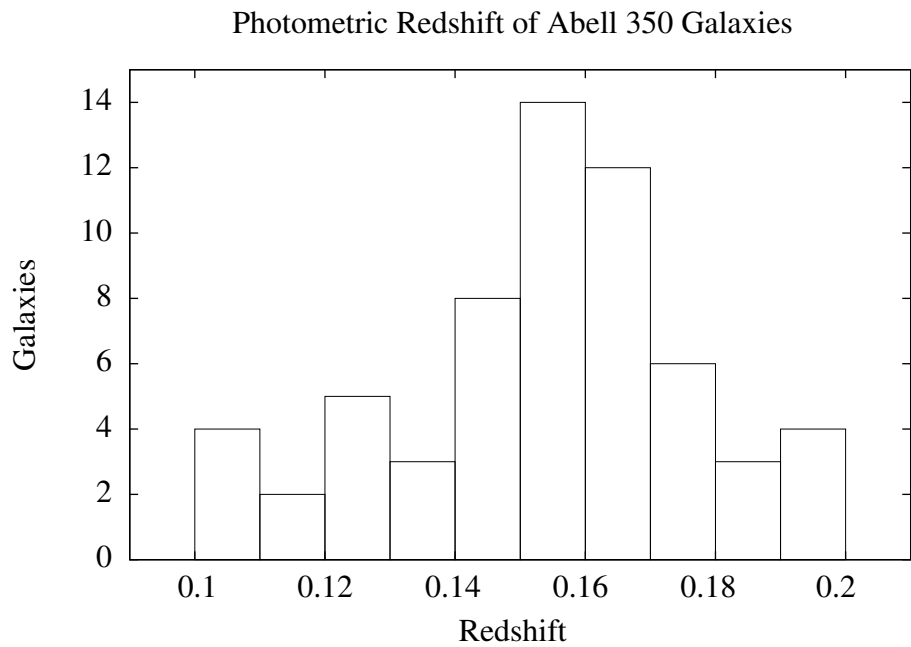


Figure 6. Redshift of galaxies in the direction of cluster Abell 350. Data taken from SDSS.

Table 1. Target clusters selected for this project.

Cluster	RA (degrees)	Dec (degrees)	z	r-band exposure (s)	u-band exposure (s)
A76	9.98315	6.8486	0.041	240	1200
A98N	11.6031	20.6218	0.104	2160	2160
A98S	11.6221	20.4680	0.104	2160	2160
A350	36.2721	-9.8366	0.157	2000	3000
A351	36.3331	-8.7218	0.111	2000	4200
A362	37.9215	-4.8827	0.184	2500	3000
A655	126.3712	47.1337	0.127	2940	3320
A795	141.0222	14.1727	0.136	2880	700
A1920	216.8524	55.7502	0.131	4000	6000
A1940	218.8686	55.1312	0.140	2000	3000
A2100	234.0773	37.6438	0.153	1600	1600
A2107	234.9127	21.7827	0.041	600	3600
A2147	240.5709	15.9747	0.035	600	3060
A2199	247.1594	39.5513	0.030	1600	1600
A2688	0.0318	15.8342	0.151	2160	2160

The central coordinates given in Table 1 are for the brightest cluster galaxy (BCG).

If X-ray data is available, it was used to confirm that the choice of BCG was correct. For all clusters except one (Abell 98), choosing the BCG was straightforward. Images of all clusters are shown in Figs. 7-21. Abell 98 has two potential centers (Fig. 8). An image from the *Chandra X-Ray Observatory* shows sub-structure in the cluster (Fig. 9).

In order to analyze the cluster sample, the inner and outer regions are compared using circular annuli. This presupposes a spherical symmetric cluster. Since Abell 98 is bimodal, it is treated as two separate clusters. The north and south components are differentiated by appending an “N” and “S,” respectively. The image was split in the y-coordinate, halfway between the two centers.

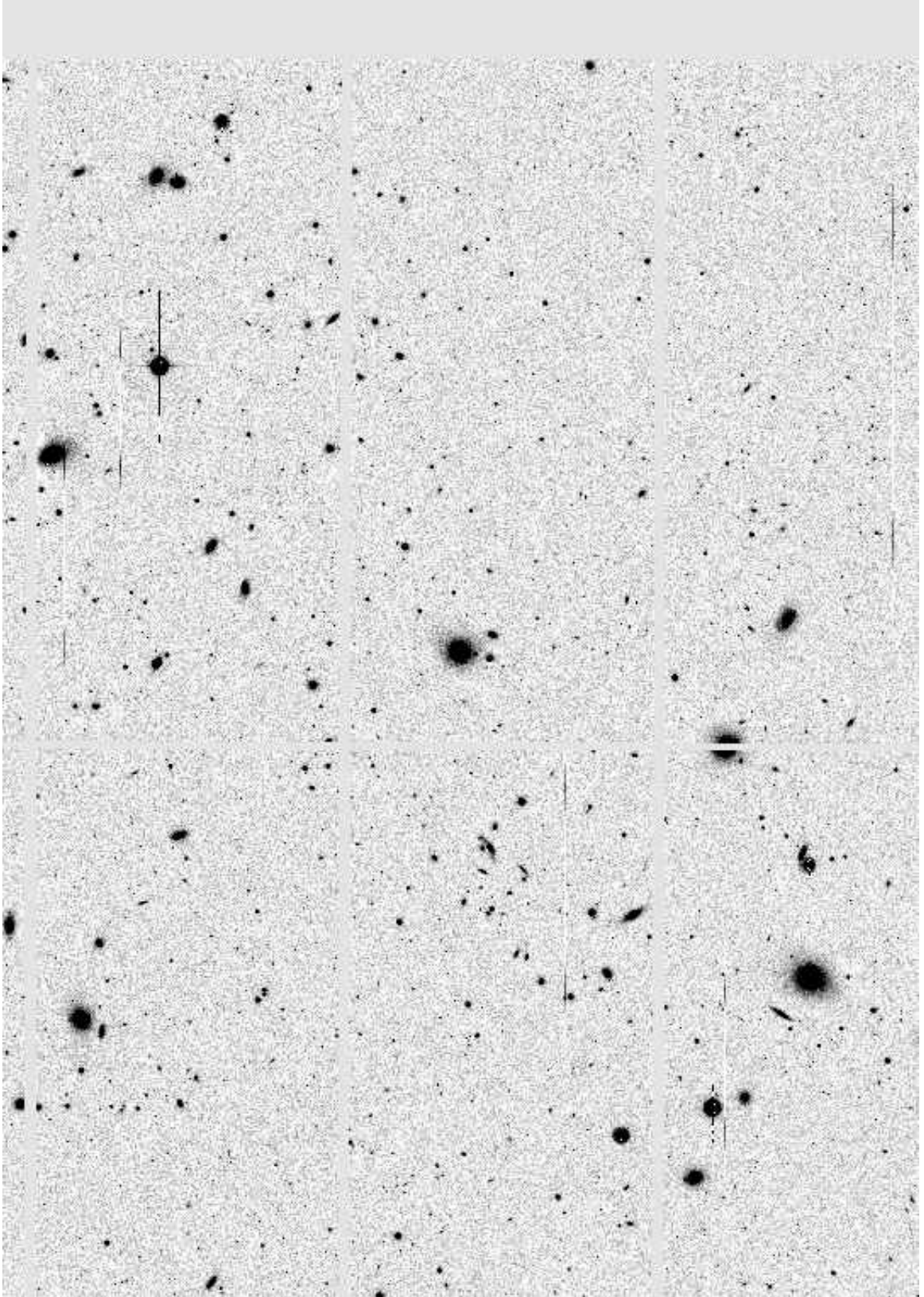


Figure 7. *r*-band image of Abell 76. At the distance of the cluster ( $z=0.041$ ), the image spans 1.0 Mpc across.

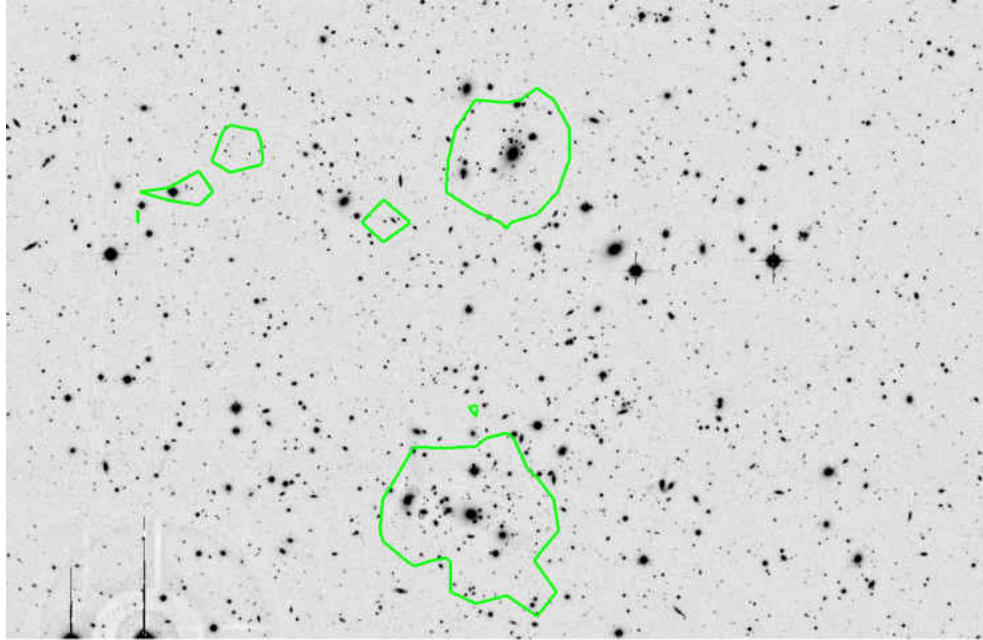


Figure 8. Two possible central locations for the cluster are in the top and bottom of this *r*-band image of Abell 98. The green lines are contours derived from the X-ray data. At the distance of the cluster ( $z=0.104$ ), the image spans 3.2 Mpc across.

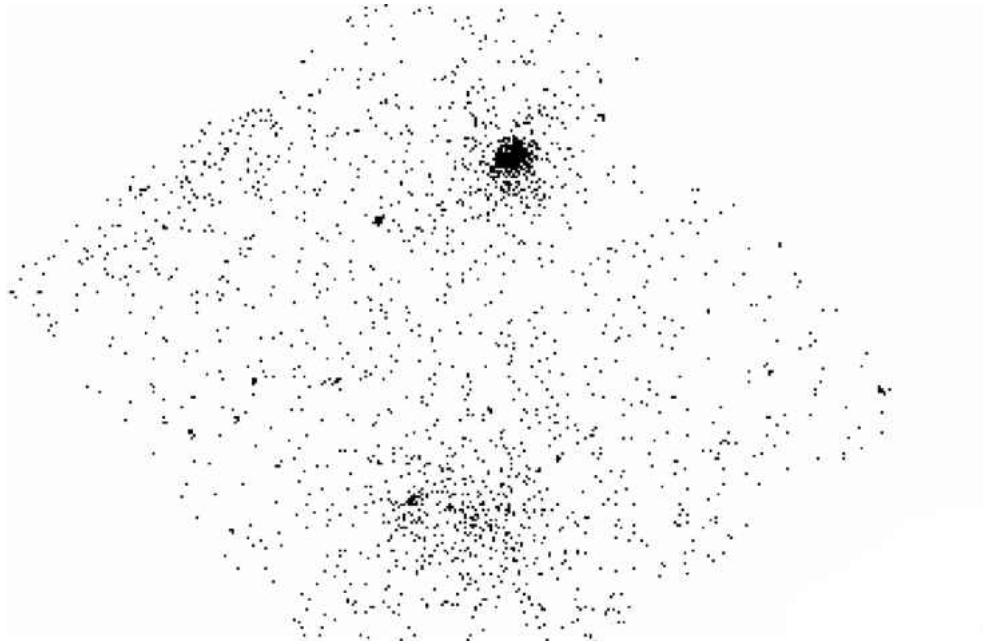


Figure 9. Chandra x-ray data shows two extended sources in Abell 98.

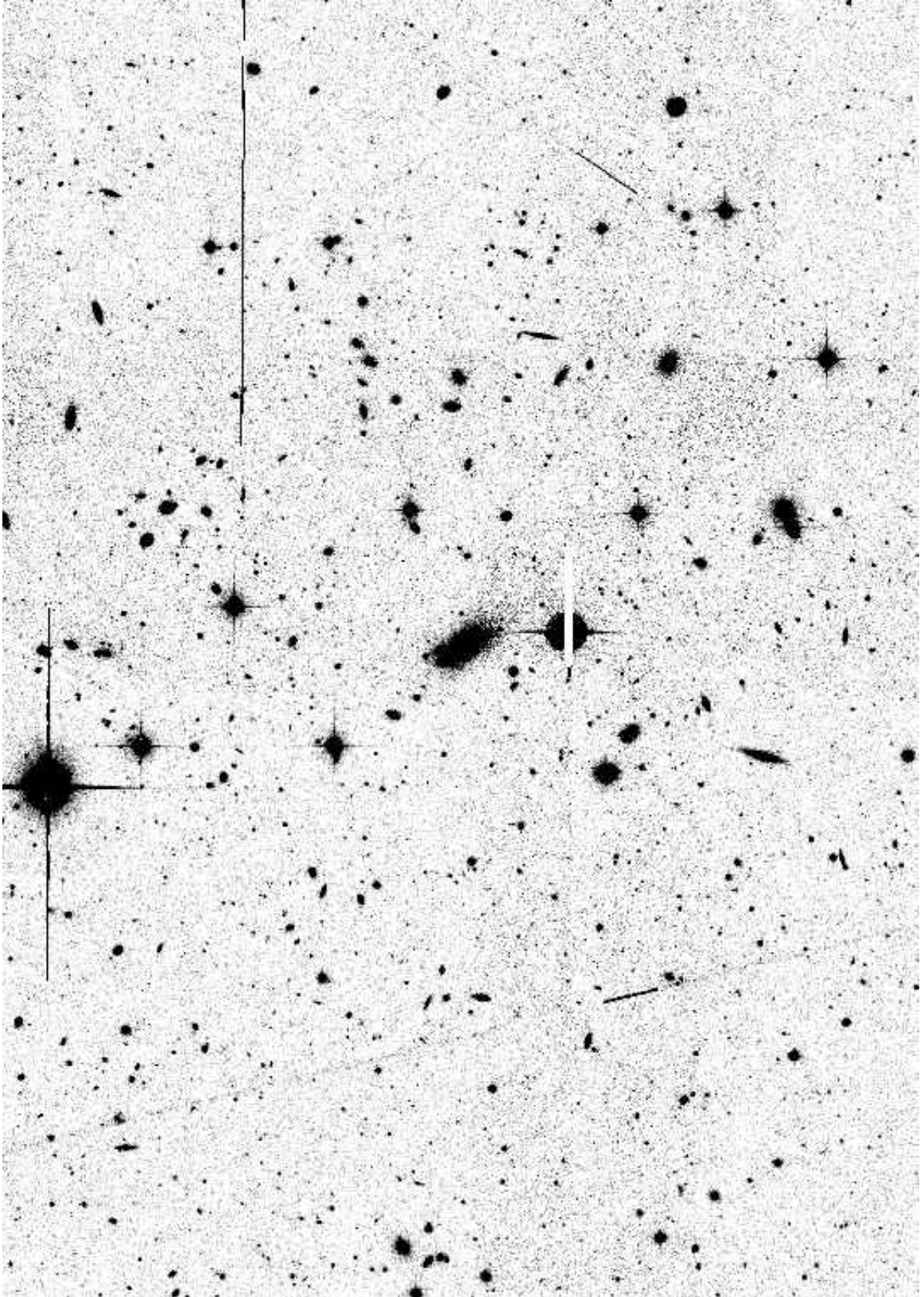


Figure 10. *r*-band image of Abell 350. At the distance of the cluster ( $z=0.157$ ), the image is 1.6 Mpc across.



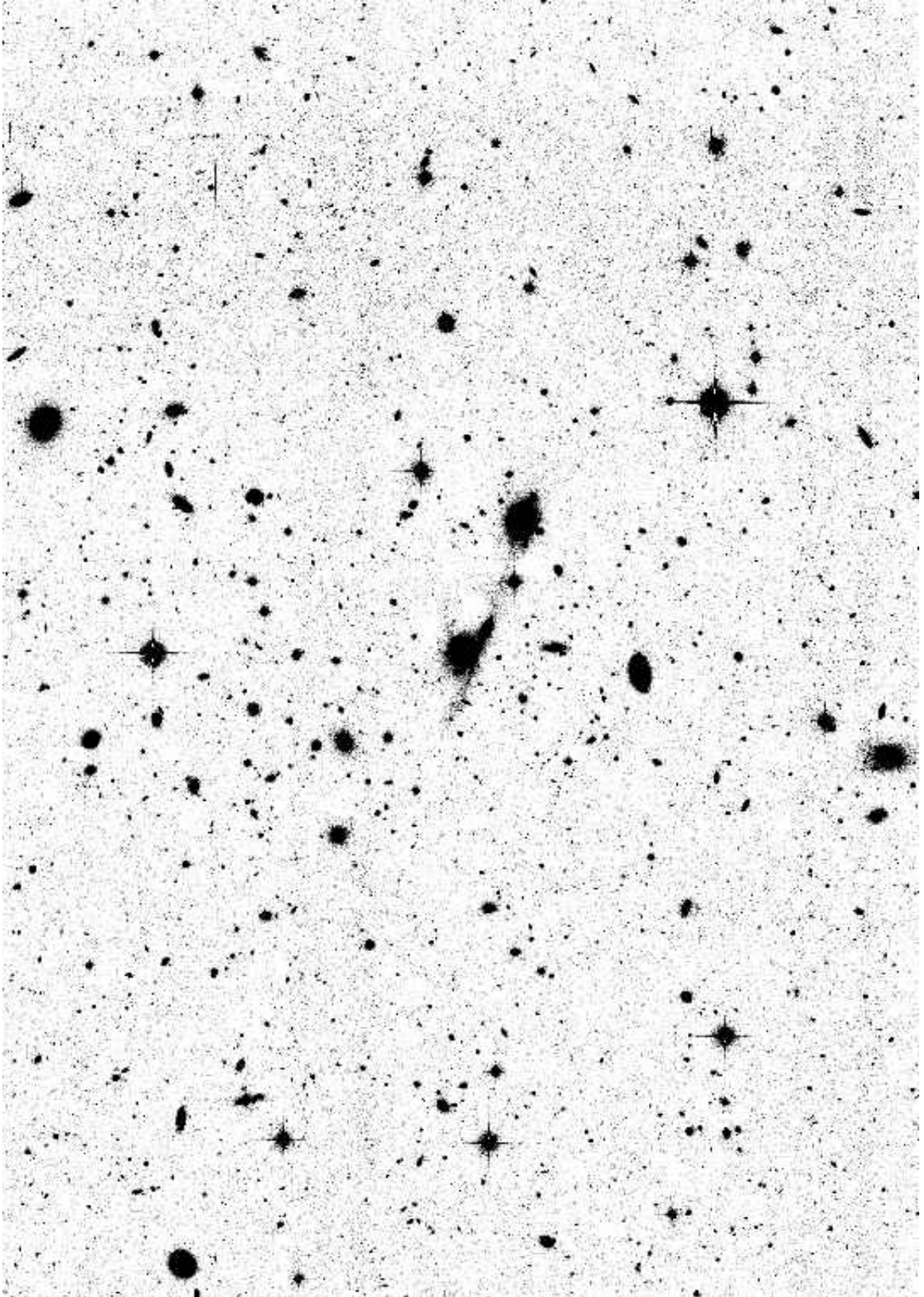


Figure 11. *r*-band image of Abell 351. At the distance of the cluster ( $z=0.111$ ), the image is 1.6 Mpc across.

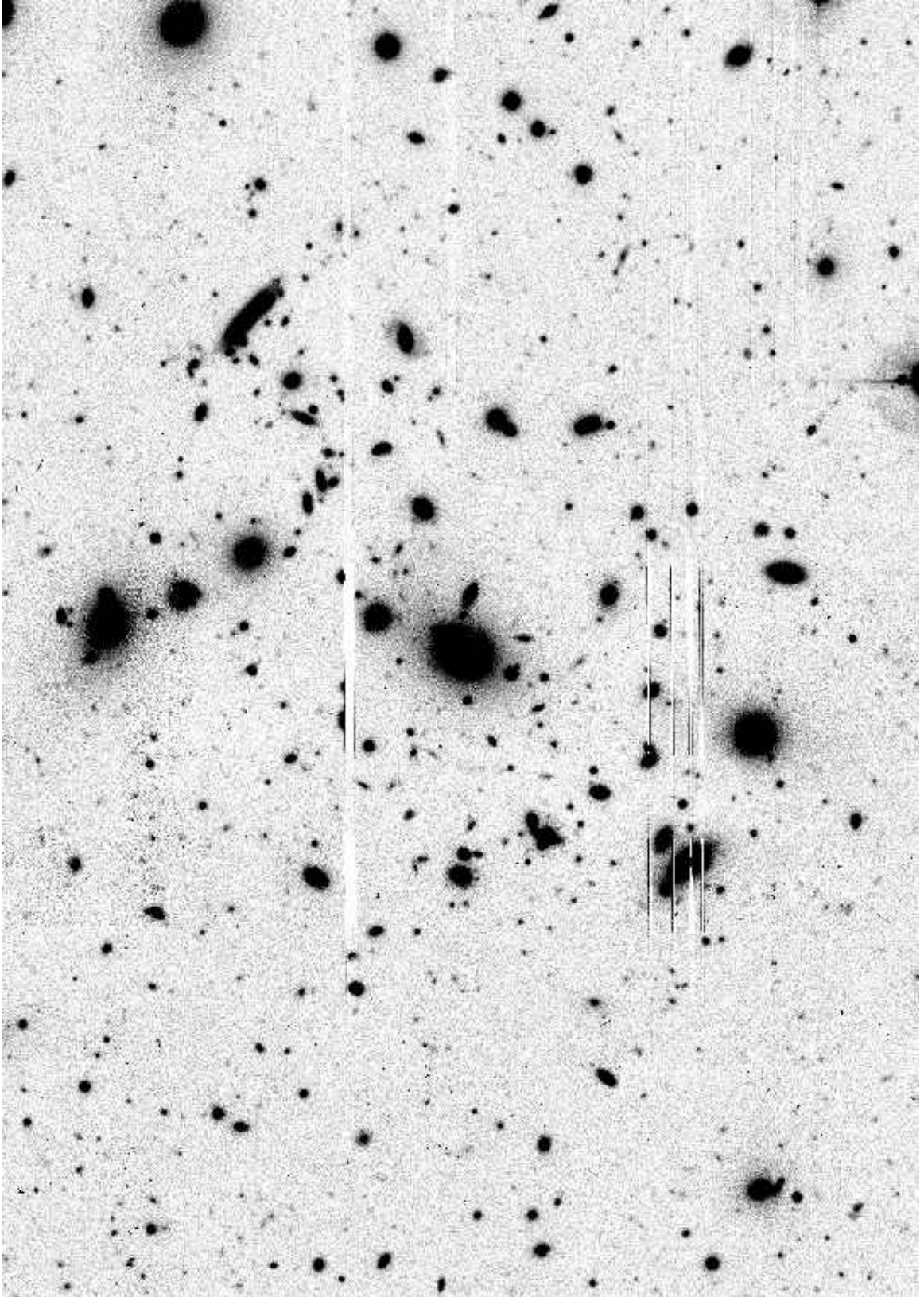


Figure 12. *r*-band image of Abell 362. At the distance of the cluster ( $z=0.184$ ), the image is 0.7 Mpc across.



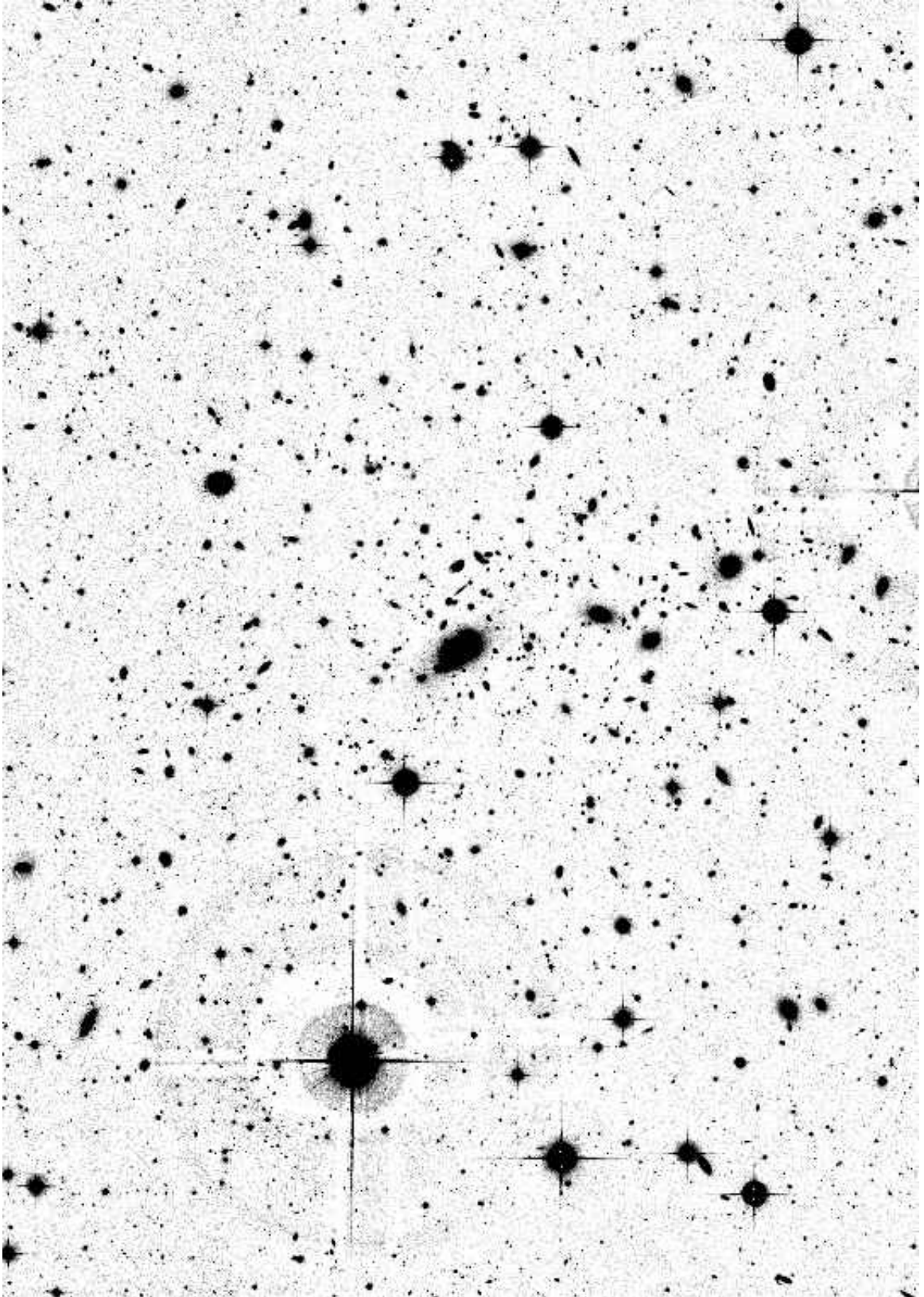


Figure 13. *r*-band image of Abell 655. At the distance of the cluster ( $z=0.127$ ), the image is 2.0 Mpc across.

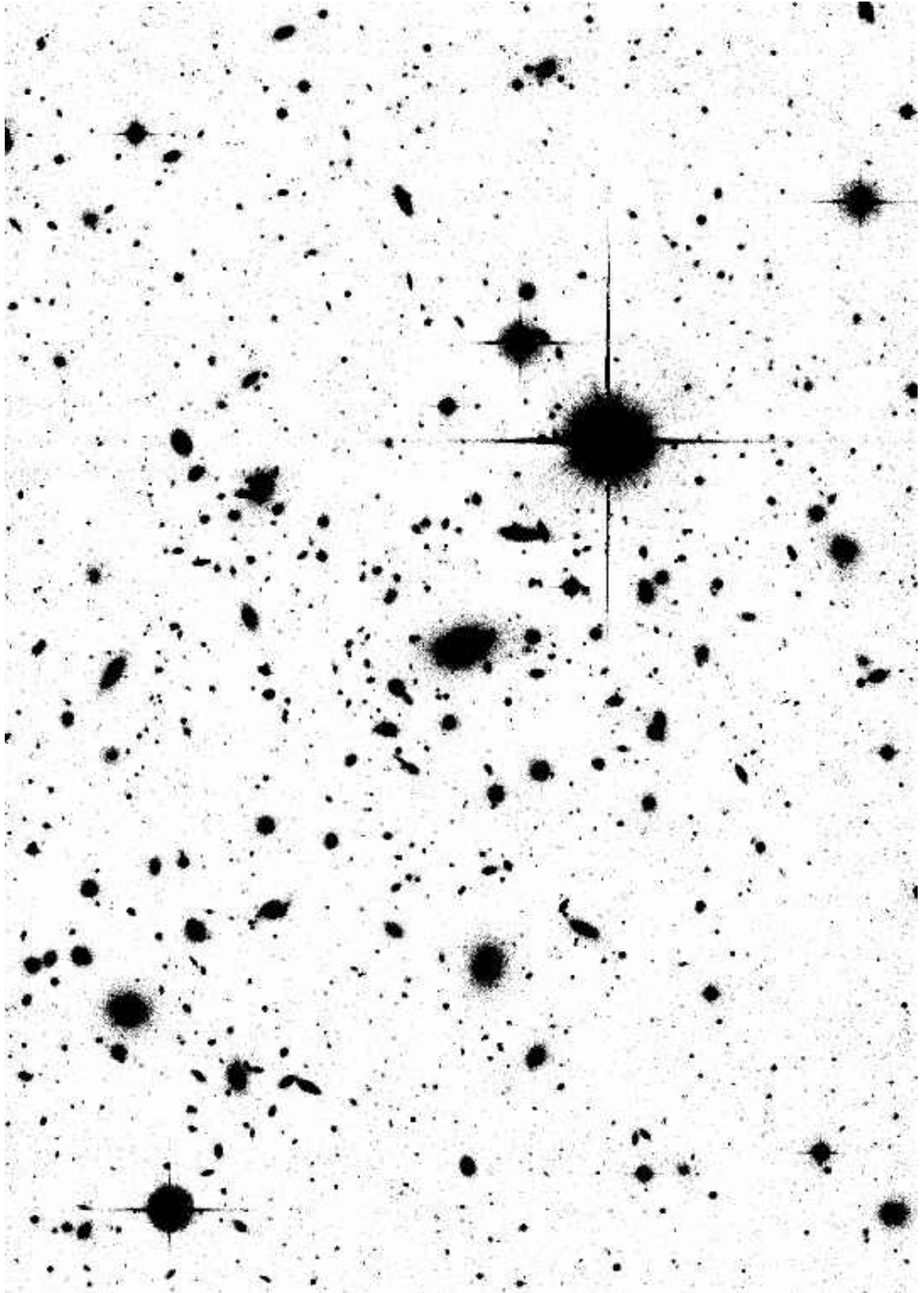


Figure 14. *r*-band image of Abell 795. At the distance of the cluster ( $z=0.136$ ), the image is 1.0 Mpc across.

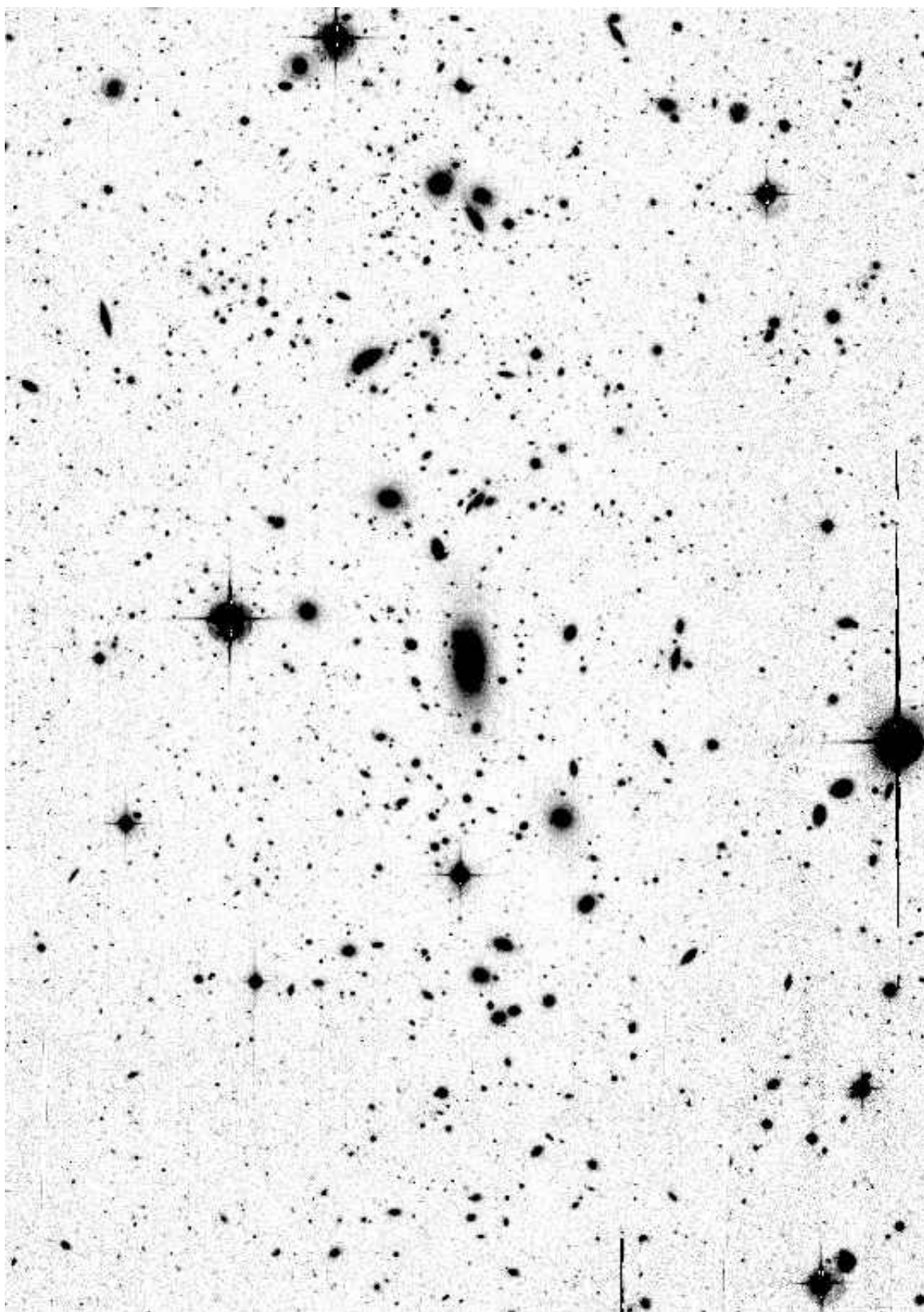


Figure 15. *r*-band image of Abell 1920. At the distance of the cluster ( $z=0.131$ ), the image is 1.3 Mpc across.

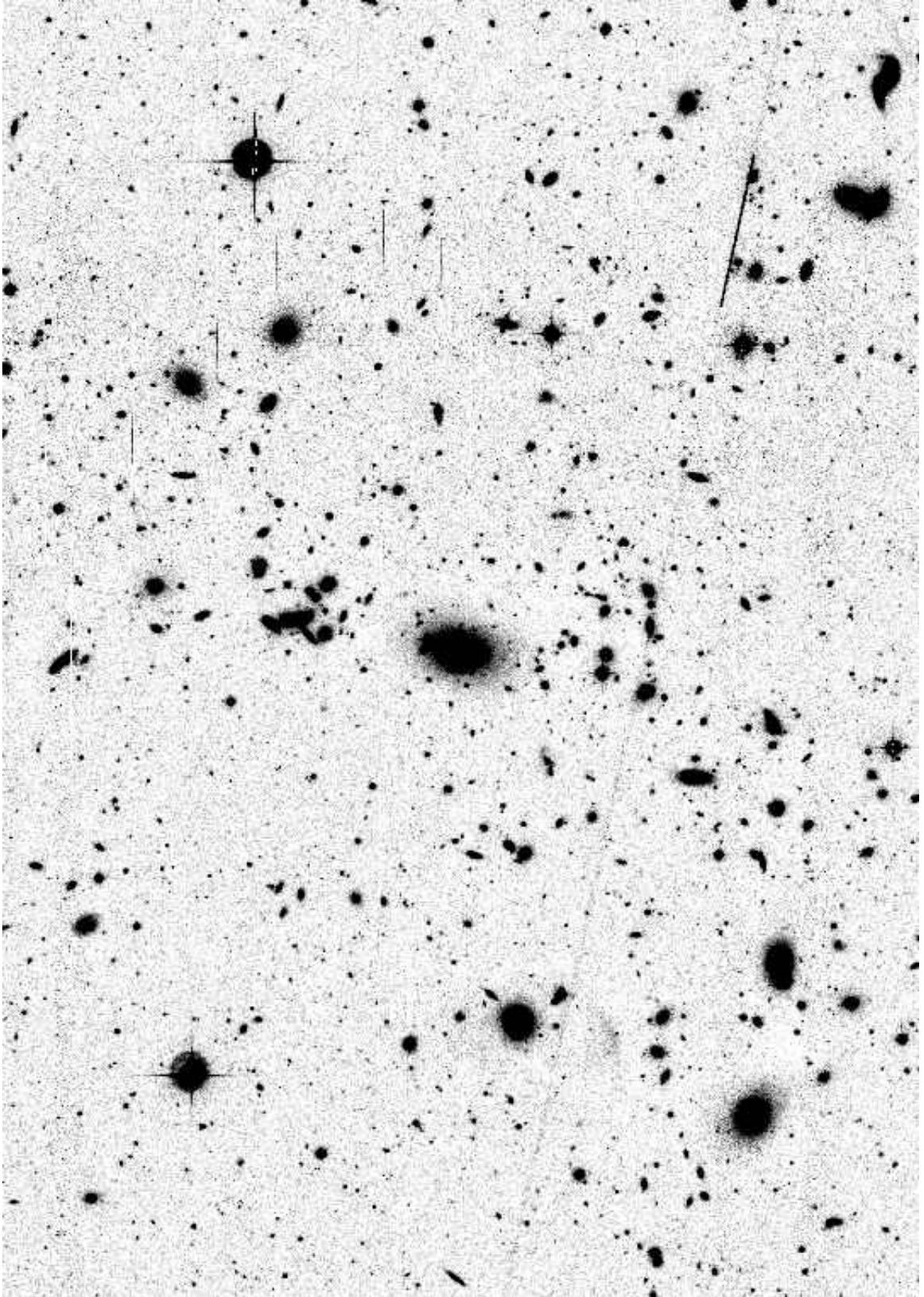


Figure 16. *r*-band image of Abell 1940. At the distance of the cluster ( $z=0.140$ ), the image is 1.3 Mpc across.



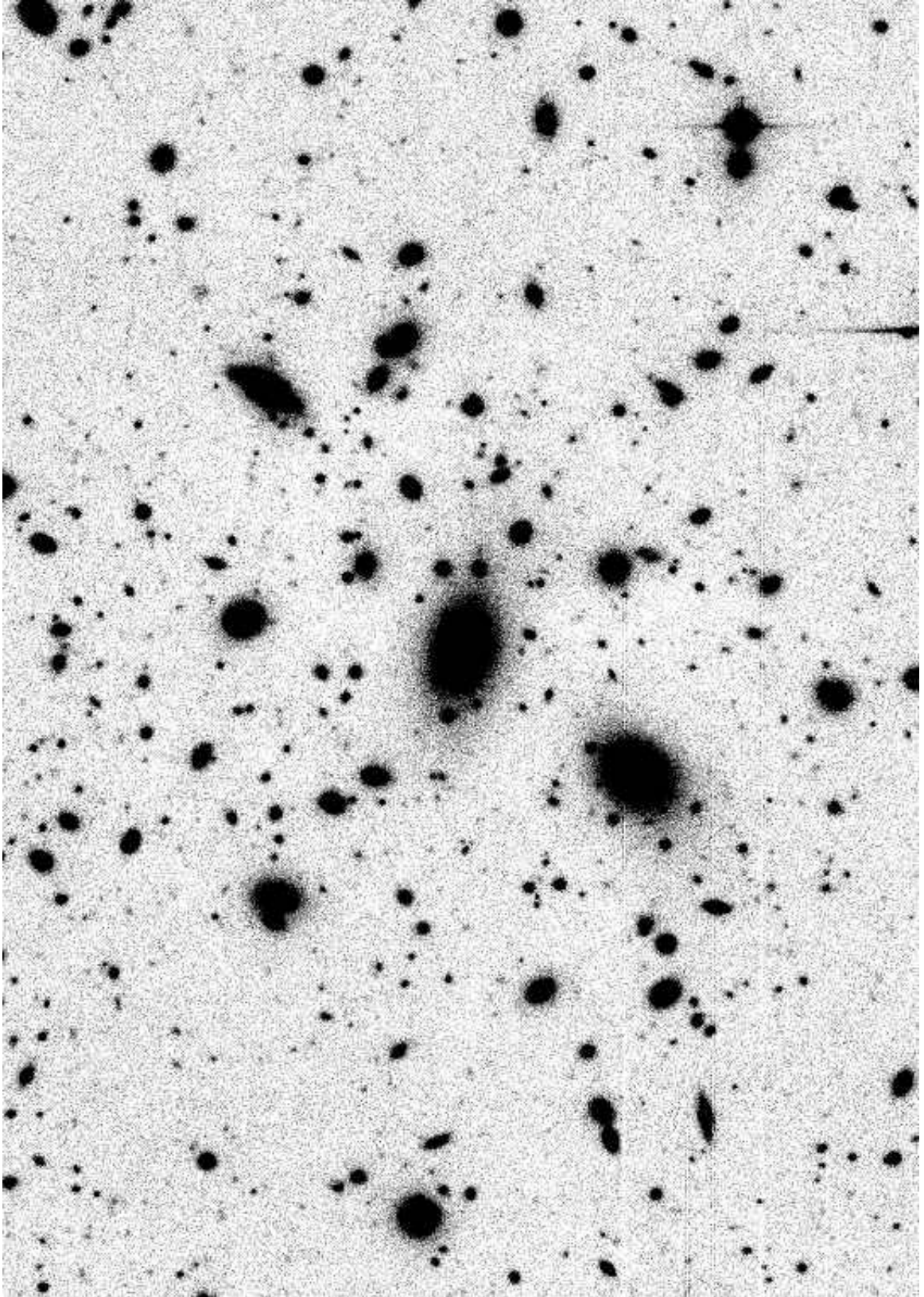


Figure 17. *r*-band image of Abell 2100. At the distance of the cluster ( $z=0.153$ ), the image is 0.6 Mpc across.

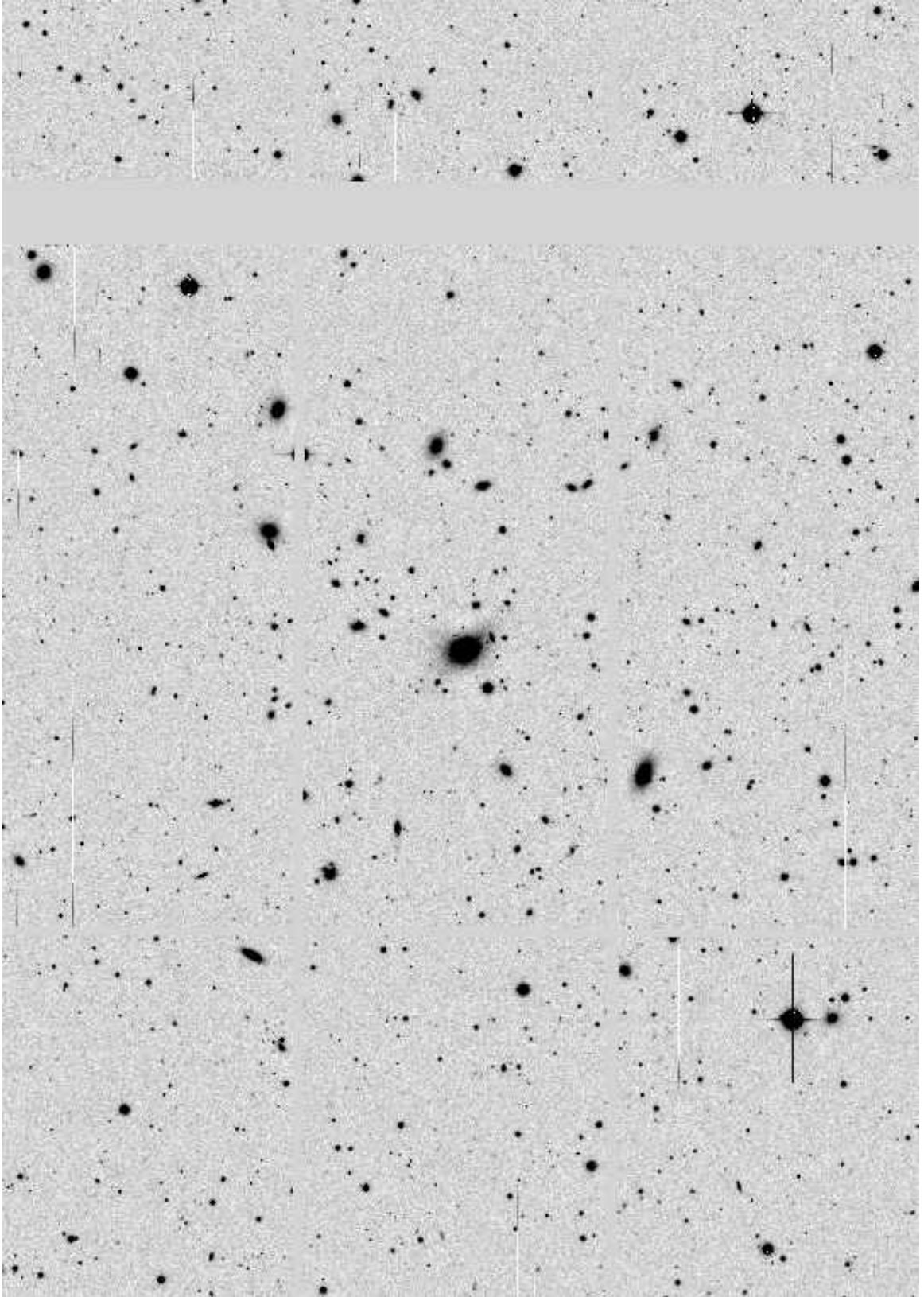


Figure 18. *r*-band image of Abell 2107. At the distance of the cluster ( $z=0.041$ ), the image is 1.0 Mpc across.

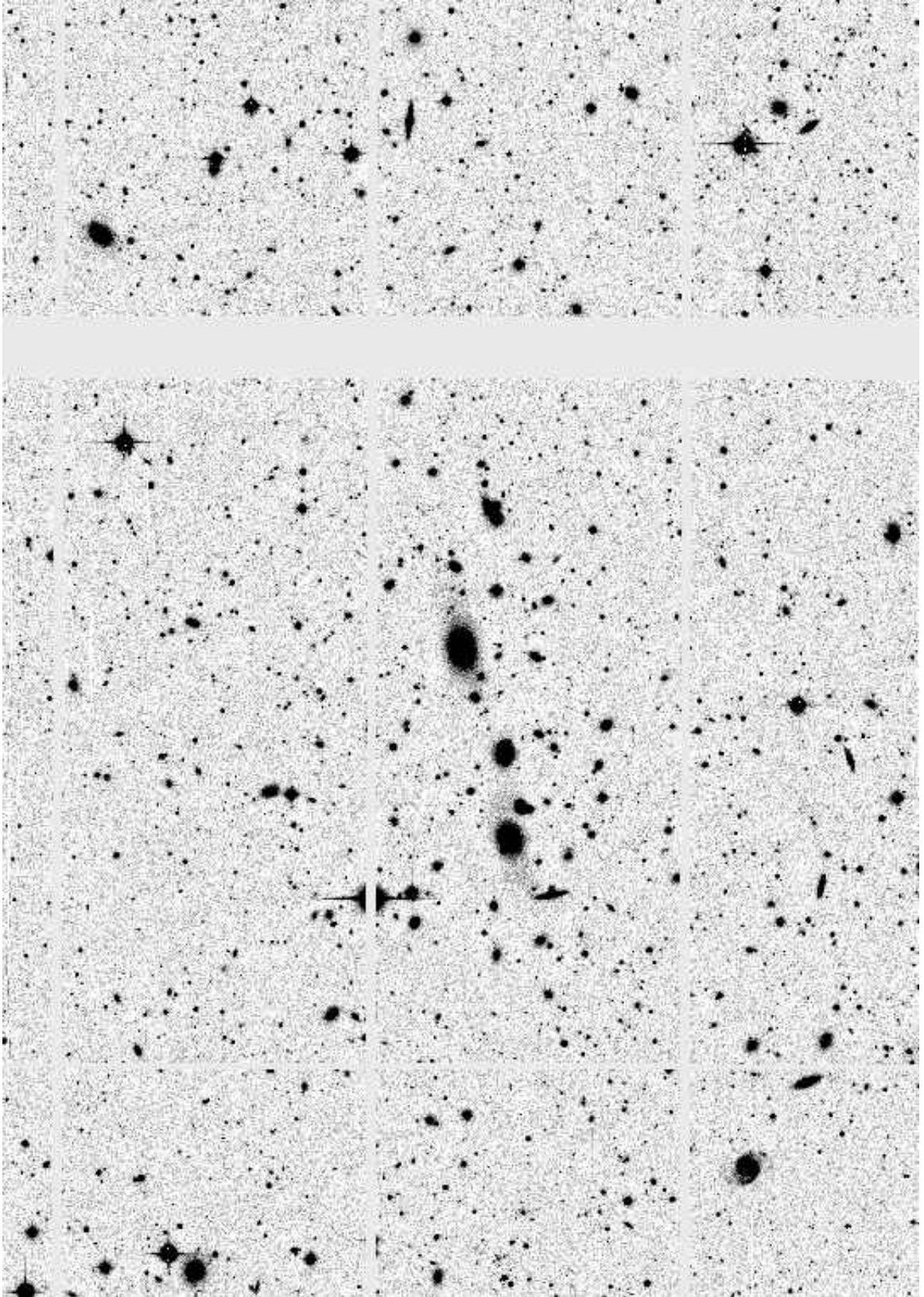


Figure 19. *r*-band image of Abell 2147. At the distance of the cluster ( $z=0.035$ ), the image is 0.8 Mpc across.



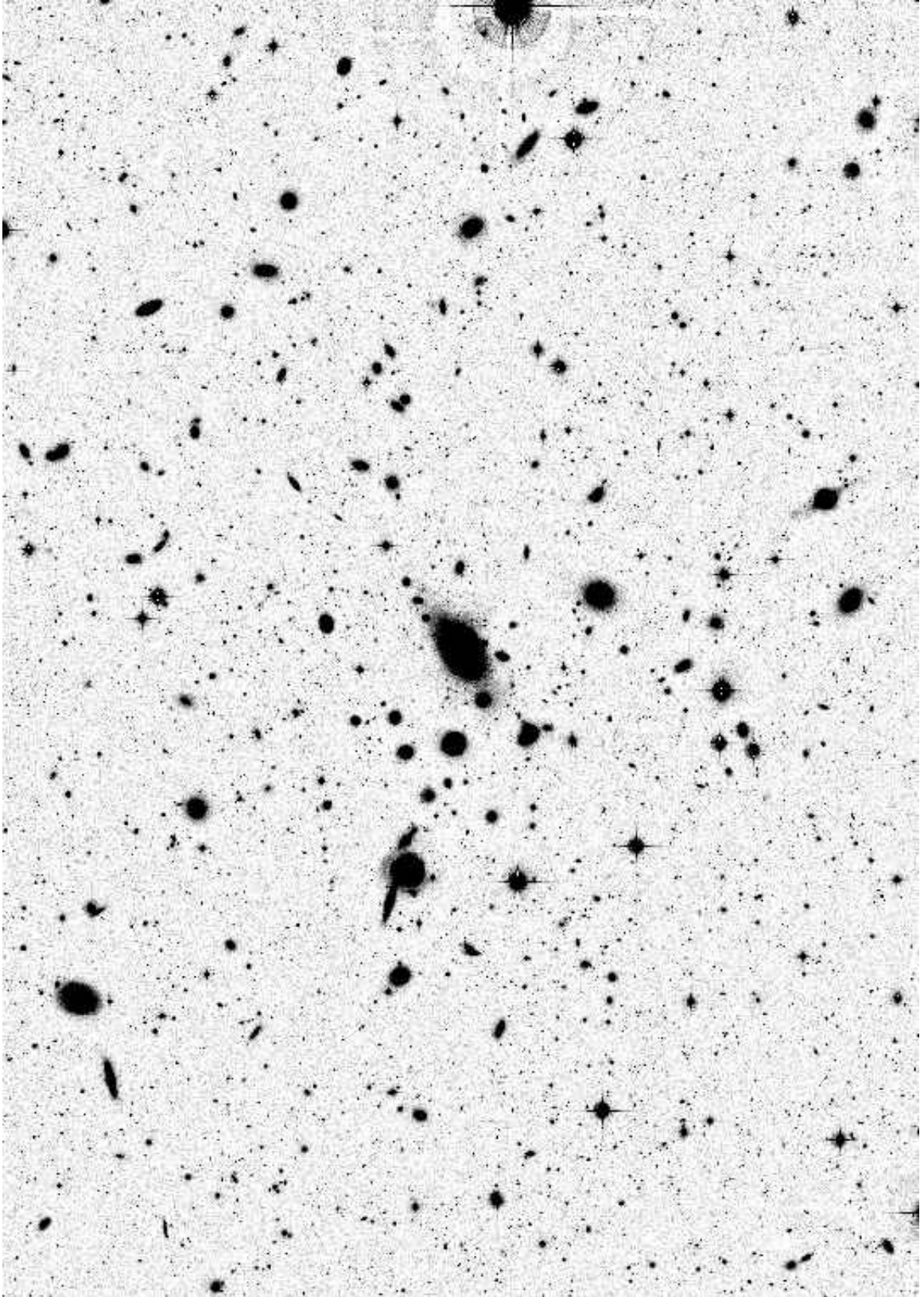


Figure 20. *r*-band image of Abell 2199. At the distance of the cluster ( $z=0.030$ ), the image is 0.7 Mpc across.



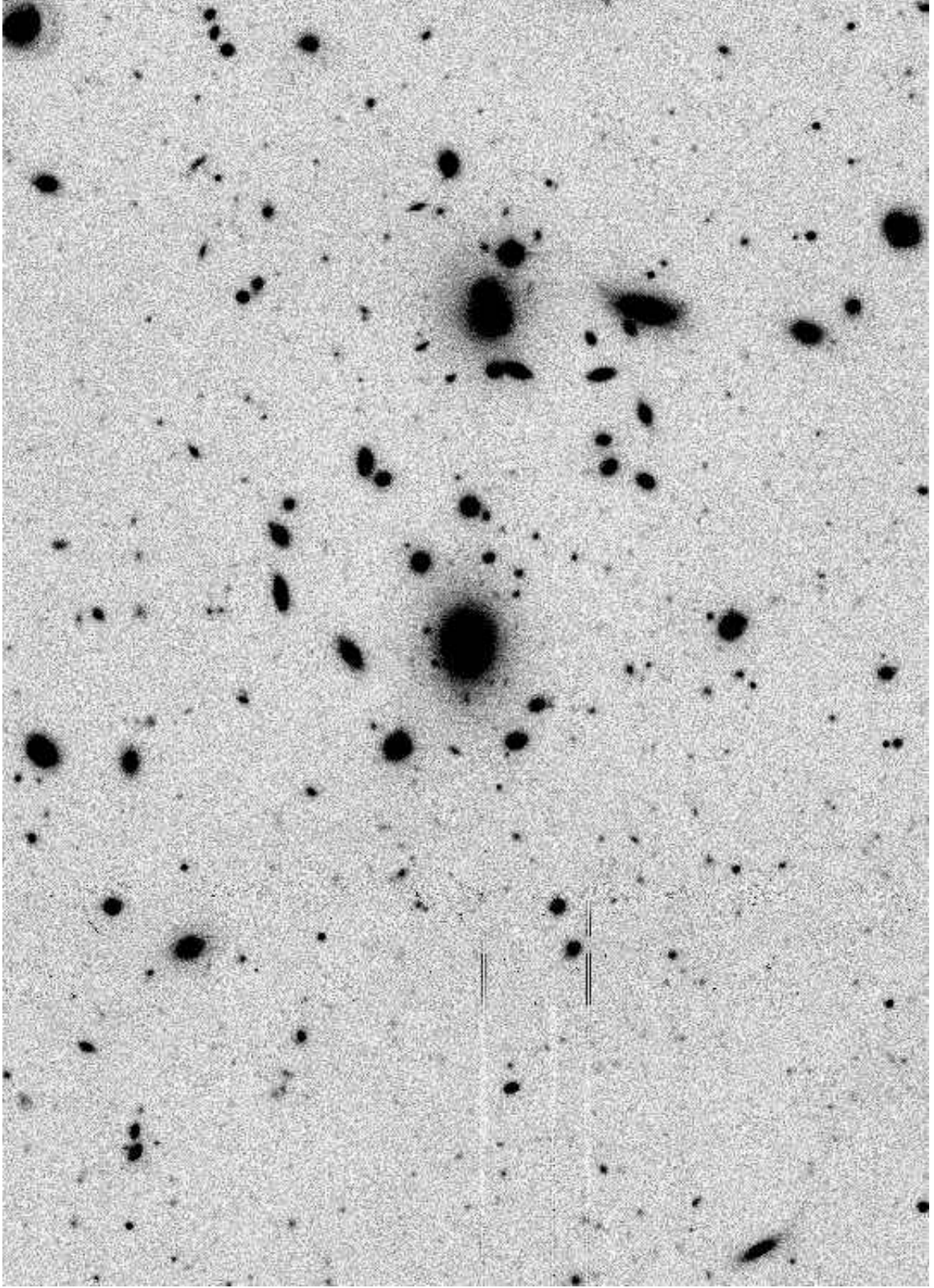


Figure 21. *r*-band image of Abell 2688. At the distance of the cluster ( $z=0.151$ ), the image is 0.6 Mpc across.

## 2.2 Data Reduction

The data from the CFHT archives have been calibrated via bias subtracting and flat-fielding. The total exposure times listed in Table 1 are the sum of the exposure times of individual images. In order to create the final science image, the individual exposures are combined using the software packages `Source Extractor`, `Scamp`, and `SWarp`. Once the final images are produced, the `Picture Processing Package (PPP)` is used to produce the final object catalog, perform magnitude measurements, and classify objects.

### 2.2.1 Source Extractor

`Source Extractor (SE)` is used to build an initial list of objects in the image (Bertin & Arnouts, 1996). First, SE splits the image into a grid mesh and computes the background in each section. The background is determined by creating a histogram of all the pixel counts in a individual element and iteratively removing outliers. This process is repeated until all points are within  $\pm 3\sigma$  (Holwerda, 2005; Bertin, 2010b). If the standard deviation changes by less than 20%, then the grid is not considered crowded, and the mean value is used as the background. If the grid is crowded the background is computed using

$$mode = 2.5 \times median - 1.5 \times mean.$$

Bright stars can contaminate an individual section in the grid. To overcome this, the background value for each element is determined by a median filter. The median value is computed by comparing background values from neighboring sections. Finally, the background is computed for an arbitrary location by fitting a bicubic spline to the backgrounds in the grid, and the background is subtracted from the image. Next, the

image is smoothed by convolving with a 3x3 discrete function given by:

$$\begin{array}{ccc} 1 & 2 & 1 \\ 2 & 4 & 2 \\ 1 & 2 & 1 \end{array}$$

SE detects objects as groups of connected pixels above background. For a pixel to be considered above background it needs to have a value  $> 1.5$  times the standard deviation of the background. SE detects objects as a grouping of at least five connected pixels above background. After objects have been detected, they are deblended by setting multiple threshold levels to create a tree of the object (Fig. 22). A detection will be split if there are at least two branches whose brightness, relative to the total brightness of the combined object, is greater than a set threshold. Each object is then checked if it still passes the detection threshold if its neighbors are removed. The nearby objects are removed by fitting them with a Moffat profile and then subtracting them from the image. The Moffat function is given by (Moffat, 1969)

$$I(r) = \frac{I_0}{(1 + (r/R)^2)^\beta}, \quad (2.1)$$

where  $R$  is the width of the profile and  $\beta$  is a constant.

### 2.2.2 *Scamp*

Scamp performs astrometric fits on an image in order to determine each object's position on the world coordinate system (WCS; Bertin 2006). The world coordinate system, which is similar to latitude and longitude, maps an object's location onto the celestial sphere using right ascension and declination coordinates. Following the procedure as described in Bertin (2010a), an object-pair catalog, which consists of every possible pair in a catalog, is

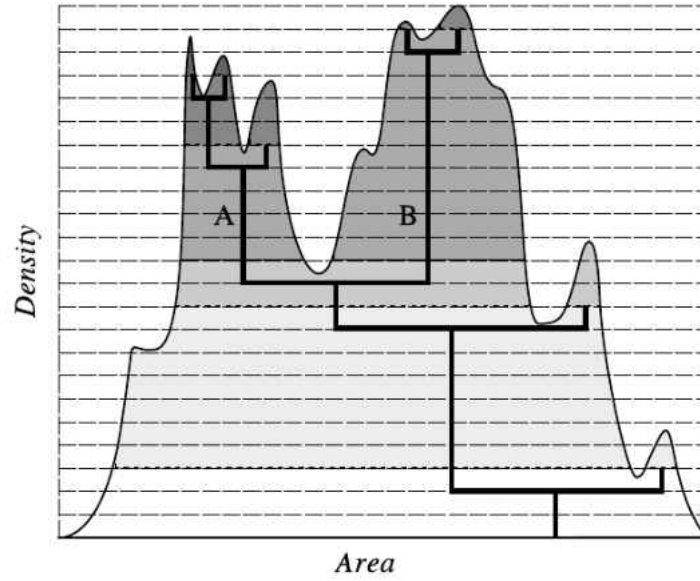


Figure 22. An example of deblending of a detection. Only peaks A and B met the requirements to be deblended into two separate objects. Reproduced from Bertin (2010b).

created for both the reference and source object list. A two dimensional histogram is created for both catalogs using the natural log of the distance and the orientation angle between pairs. The two histograms are cross correlated and band-pass filtered, and the distance scale and rotation are found using a peak finder. This same procedure is then applied to measure the relative offset in positions using histograms of source positions. Afterwards, the objects in the source and reference catalog are matched, and the astrometric fits are calculated using a 2D regression.

### 2.2.3 *SWarp*

*SWarp* is used to coadd multiple images (Bertin et al., 2002). Using the astrometry information calculated via *Scamp*, the dimensions of an output image that contains all of the input images is determined. The input images are background subtracted following the same process as described in Sec. 2.2.1. Next, each input file is mapped to a rectangular

area in the output image. The input images are filtered using a Lanczos kernel (Bertin, 2010c) and resampled. The result is saved into a temporary file and the steps are repeated for each input image. Finally, each pixel in the output image is determined by median combining all of the overlapping input images.

#### 2.2.4 *Ellipse*

The BCG is usually surrounded by several smaller galaxies. In order to measure these smaller galaxies accurately, the BCG is removed using the IRAF implemented task *Ellipse* produced by the Space Telescope Science Institute. The software models an early-type galaxy by fitting a series elliptical isophotes to the BCG (Jedrzejewski, 1987), and then subtracts the resulting model from the image (Fig. 24). Each isophote is fixed at a different semimajor axes and individually fit. Initial values for the center of the ellipse  $(x_0, y_0)$ , ellipticity  $(\epsilon)$ , and position angle  $(\phi)$  are used to sample a one dimensional intensity distribution. The distribution is fit using least squares via the eccentric anomaly (Fig. 23) to the equation

$$I = I_0 + A_1 \sin(E) + B_1 \cos(E) + A_2 \sin(2E) + B_2 \cos(2E), \quad (2.2)$$

where  $I$  is the intensity and  $E$  is the eccentric anomaly. If the errors in the fit are small, the coefficients can be used to correct the initial parameters used to generate the isophote. Let  $x'$  be the position along the major axis,  $y'$  be the position along the minor axis,  $PA$  be the position angle, and  $I'$  be the derivative of the intensity along the major axis.  $I'$  is determined by comparing the intensity profiles of a slightly larger and smaller ellipse. The

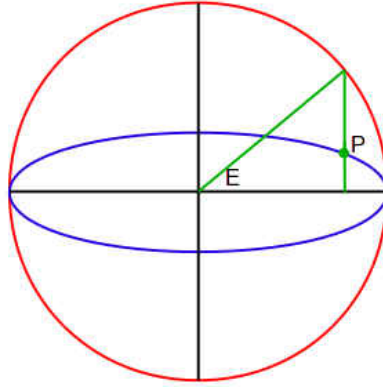


Figure 23. The eccentric anomaly for point P on the ellipse is given by E.

corrections to the fit are (Jedrzejewski, 1987)

$$\begin{aligned}
 \Delta x' &= \frac{-B_1}{I'}, \\
 \Delta y' &= \frac{-A_1(1 - \epsilon)}{I'}, \\
 \Delta \epsilon &= \frac{-2B_2(1 - \epsilon)}{a_0 I'}, \\
 \Delta PA &= \frac{2A_2(1 - \epsilon)}{a_0 I'((1 - \epsilon)^2 - 1)}.
 \end{aligned}
 \tag{2.3}$$

The quantity that has the largest offset is corrected and the isophote is fit again. The process is repeated until a sufficiently good fit is found.

### 2.2.5 *Picture Processing Package*

Once all the images in an individual exposure have been combined using SWarp, the image is sectioned into four quarters, with a 200 pixel overlap. The Picture Processing Package (PPP; Yee 1991; Yee, Ellingson, & Carlberg 1996) is used to generate an object catalog for each section. First, the image is smoothed using a tapered box car filter. Then, PPP iterates through all the local maximum pixel values and measures

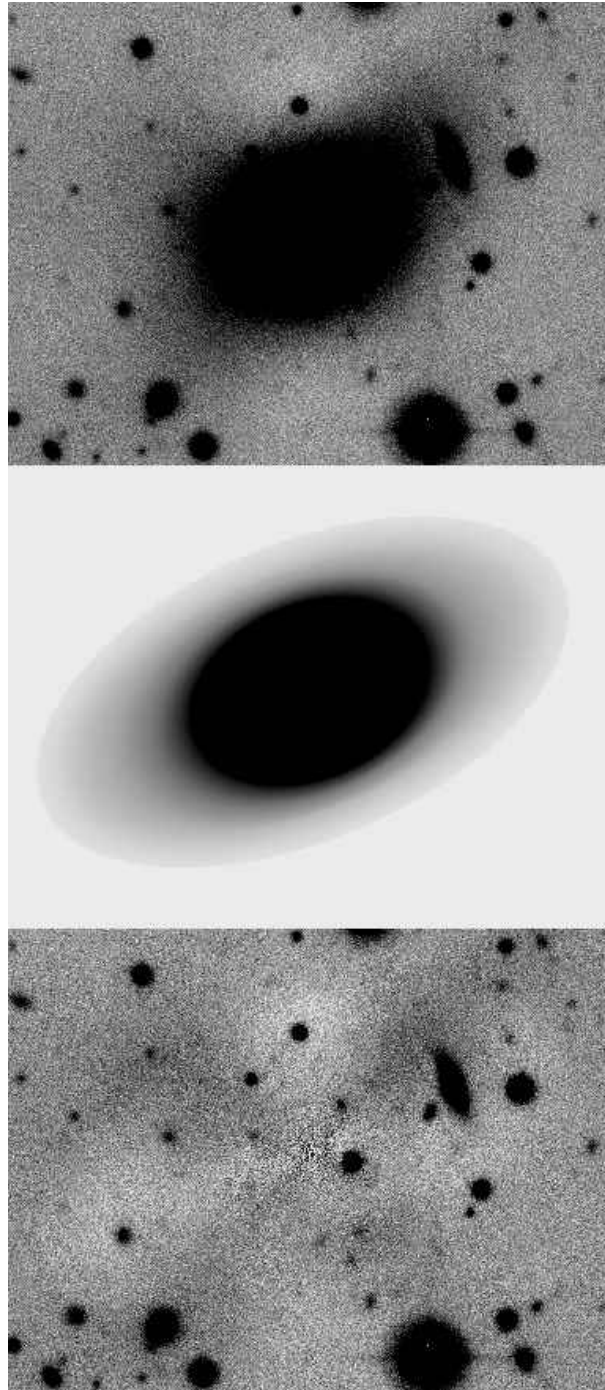


Figure 24. The top panel shows the original image, the middle figure shows the model determined by `Ellipse`, and the bottom panel shows the image after the model was subtracted from the original image.

the net flux from nine pixels centered on the peak. The background flux is determined in a circular annulus around the local maximum. If the net flux is above a chosen threshold

parameter, based on the RMS of the background, it is considered a detection. The background in the annulus is computed by

$$2 \times \text{median} - \text{mean}. \quad (2.4)$$

After all detections have been made, they are overlaid on the image and checked near bright stars and galaxies for obvious missed objects, or artifacts misidentified as objects. Missed objects are added to the catalog, and bogus objects are removed.

The magnitude of each detection is measured by computing a growth curve for each object. First, all neighboring objects are masked. The minimum pixel that lies on a line between the neighbor and the galaxy being measured is found. Then, a circular mask is created, centered on the neighboring galaxy, whose radius is the distance to the minimum pixel plus a fixed number of pixels. For a neighbor that is over twice as bright as the galaxy being measured, all data is masked beyond a line orthogonal to the line connecting the neighboring galaxy and the measured galaxy. After all the neighbors have been masked, the magnitude of the object is measured using circular apertures starting with a diameter of three pixels, and successively increasing by four pixels up to a maximum diameter of 63 pixels. A comparison of the magnitudes as a function of aperture, known as a growth curve, is used to determine the final aperture for the object. The smallest aperture according to the following specifications is chosen (Yee, 1991):

1. The diameter where the growth curve's slope has increased two times in a row.
2. The diameter in which there is a downward trend in the growth curve that is inconsistent with noise fluctuations.



3. The diameter where there is no decrease in the derivative for two consecutive apertures.
4. A 12'' max diameter.

After all of the galaxies are measured, PPP re-measures all bright galaxies using a larger maximum aperture.

After the flux is measured within the determined aperture, a small correction is applied to the flux from the growth curve of a reference star. All measurements are converted to the magnitude system with

$$m = m_0 - 2.5 \text{ Log}(F), \quad (2.5)$$

where  $m$  is the magnitude,  $m_0$  is the zeropoint, and  $F$  is the aperture-corrected flux. There is an associated error in the flux which corresponds to an error in the magnitude. The conversion to magnitude with an associated error in flux is

$$\begin{aligned}
 & m_0 - 2.5 \log(F \pm \Delta F), \\
 & m_0 - 2.5 \log\left(F \left[1 \pm \frac{\Delta F}{F}\right]\right), \\
 & \underbrace{m_0 - 2.5 \log(F)}_m - \underbrace{2.5 \log\left(1 \pm \frac{\Delta F}{F}\right)}_{\Delta m}.
 \end{aligned} \quad (2.6)$$

If  $\Delta F/F$  becomes greater than one,  $\log(1 - \Delta F/F)$  becomes invalid. Looking at just the

positive sign,

$$\begin{aligned}\Delta m &= 2.5 \log\left(1 + \frac{\Delta F}{F}\right), \\ \Delta m &= \frac{2.5}{\ln(10)}\left(\frac{\Delta F}{F} - \frac{1}{2}\left[\frac{\Delta F}{F}\right]^2 + \dots\right), \\ \Delta m &\approx \left(\frac{\Delta F}{F}\right).\end{aligned}\tag{2.7}$$

Next, the error in flux is determined from the uncertainty in the background measurement. Since the uncertainty in faint galaxies is dominated by fluctuations in the background flux, the error is determined from the background flux alone. The uncertainty is calculated by (Yee, 1991)

$$\Delta F = \sigma_{sky} N_{pix}^{1/2},\tag{2.8}$$

where  $\sigma_{sky}$  is the RMS of the sky, and  $N_{pix}$  is the number of pixels inside the adopted aperture.

In order to accurately measure object colors it is important that the apertures are chosen fairly. For each cluster, a fixed aperture is chosen for all color measurements. Since PPP measures multiple apertures using a diameter step size of four, the smallest aperture that is larger than three times the full width half maximum (FWHM) of a stellar profile is used. This choice of aperture size was made to ensure that there are no seeing effects biasing color measurements. The FWHM is measured in both bands, and the larger value is chosen.

After magnitudes are measured, all objects are classified as either saturated, galaxy, star, or defect. This decision is based on each object's classification parameter,  $C_2$ , which is measured by comparing the growth curve of an object with that of a reference

star. More specifically,

$$C_2 = \frac{1}{N_a - 2} \sum_{i=3}^{N_a} (m_i^* - m_i) - C_0,$$

where  $N_a$  is the aperture number,  $m_i^*$  is the magnitude of a reference star in aperture  $i$ ,  $m_i$  is the object's magnitude for aperture  $i$ , and  $C_0$  is the difference between the magnitude of the reference star and the object being measured. After  $C_2$  values have been measured,

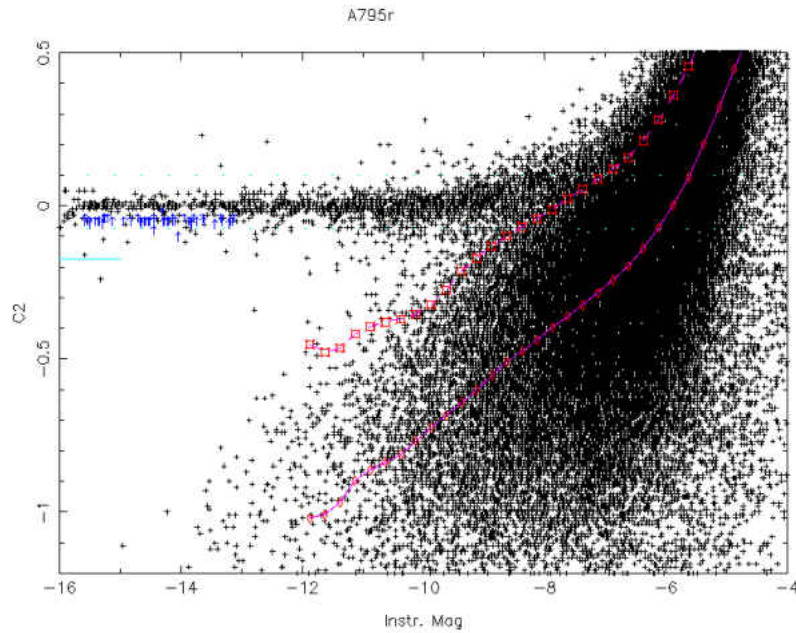


Figure 25.  $C_2$  classification versus instrumental magnitude. The lower line is the smoothed modal value of the distribution, and the upper line is determined from the RMS of the distribution. The arrows point to the reference stars used in computing  $C_2$ .

each object is assigned a class based on its  $C_2$  value. For bright objects, a galaxy is classified as having a  $C_2$  value  $\leq -0.075$ . Stars are objects whose  $C_2$  value is  $> -0.075$  and  $\geq 0.1$ . Objects whose values  $> 0.1$  are defects.

At faint magnitudes, the  $C_2$  values of stars and galaxies merge. Stars and galaxies are then separated according to a variable classifier based on the modal values of the

galaxy distribution binned in magnitude. A line going through the smoothed modal values is defined in order to track the nominal value of  $C_2$  for a galaxy (Fig. 25). A second line, which is used to classify objects, is defined  $n\sigma$  away from the first line, where  $n$  is a chosen parameter. Objects below this line are classified as galaxies, while objects above this line are classified as stars. This scheme provides, at least statistically, the correct number of classified galaxies. Since the number of galaxies is much larger than the number of stars at faint magnitudes, the contamination of stars is low.

There are two issues that arise during photometry. First, the maximum aperture may be too small for very large galaxies. Second, the apertures of smaller objects in the halos of bright objects can be grown too large. As such, the apertures used to measure magnitudes were visually checked.

After PPP is run there are separate object catalogs for the  $u$ - and  $r$ -band. However, the magnitude measurements need to be merged in order to determine object color. This is done for all objects that are not considered to be cosmic rays. Objects are classified as cosmic rays if the ratio of the peak pixel value to the neighboring pixel values is greater than a set parameter. After they are removed, the catalogs were matched by sorting the  $r$ - and  $u$ -band data into ascending order according to magnitude, and matching each  $r$ -band object with one  $u$ -band object using a maximum match radius of 6 pixels. To keep the sample complete, detections missed in one band are added to the other band's object catalog.

The size of a catalog can reach  $\approx 500000$  objects, and brute force matching by calculating the distance between every object pair in both catalogs can be time consuming. To match more efficiently, a k-d tree is employed (Bentley & Louis, 1975; Friedman et al.,

1977). A k-d tree is a type of binary tree (Fig. 26) used for multidimensional searching. Each level of the binary tree is associated with either the x or y pixel coordinate, where one of the branches holds all of the objects that are lower in the chosen coordinate, and the other branch holds objects which are larger.

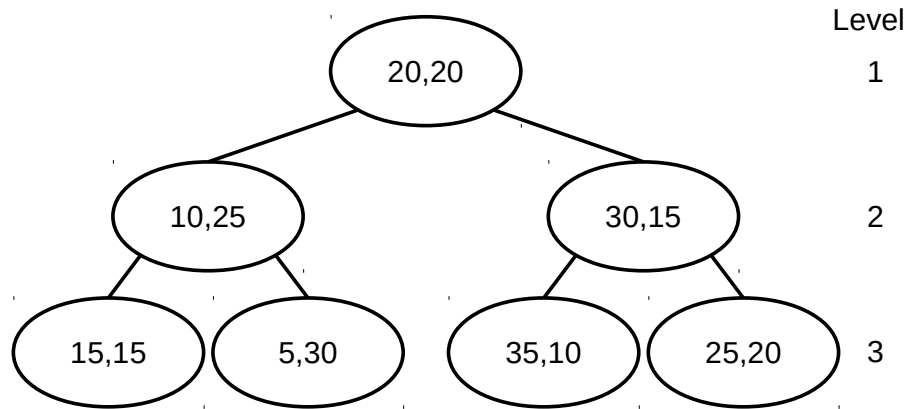


Figure 26. Example of a k-d tree for two dimensions. The first level is split on the first variable, and the second level is split on the second variable.

After the missing objects have been added in, the photometry is rerun. The resulting catalogs are once again matched, this time using a max distance of 8 pixels.

### 2.3 Additional Corrections

Sometimes saturated stars are misclassified as galaxies. The central pixel of each object, and the eight pixels that touch it, are checked to see if they surpass 60,000 counts (the saturation limit for Megacam). If any one of them surpass the limit, it is reclassified as a saturated star.

Dead columns can pose a problem for PPP's detection algorithm, which detects bogus objects along the border of dead columns. These objects were cleaned by removing all detected objects whose central pixel touches another pixel with a value that is 200 counts below the background.

Additionally, a bright star mask is created around each object that is classified as a saturated star. The radius of the star mask is determined by checking pixels diagonal from the center of the star (Fig. 27). The smallest radius where three of the four pixels are less than 100 counts above background is chosen. Masks are displayed on the image and checked for accuracy. Very large saturated stars had their masks manually adjusted. Any satellite trails are also manually masked (Fig. 28).

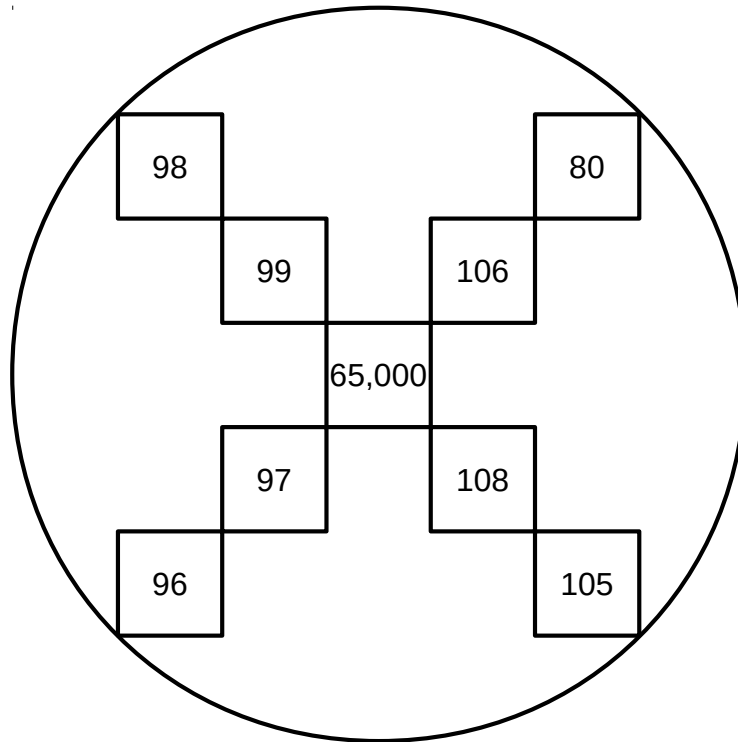


Figure 27. Sample pixels whose face shows the pixel counts. The radius of the circle used to mask the star is the smallest radius that touches 3 diagonal pixels below 100.

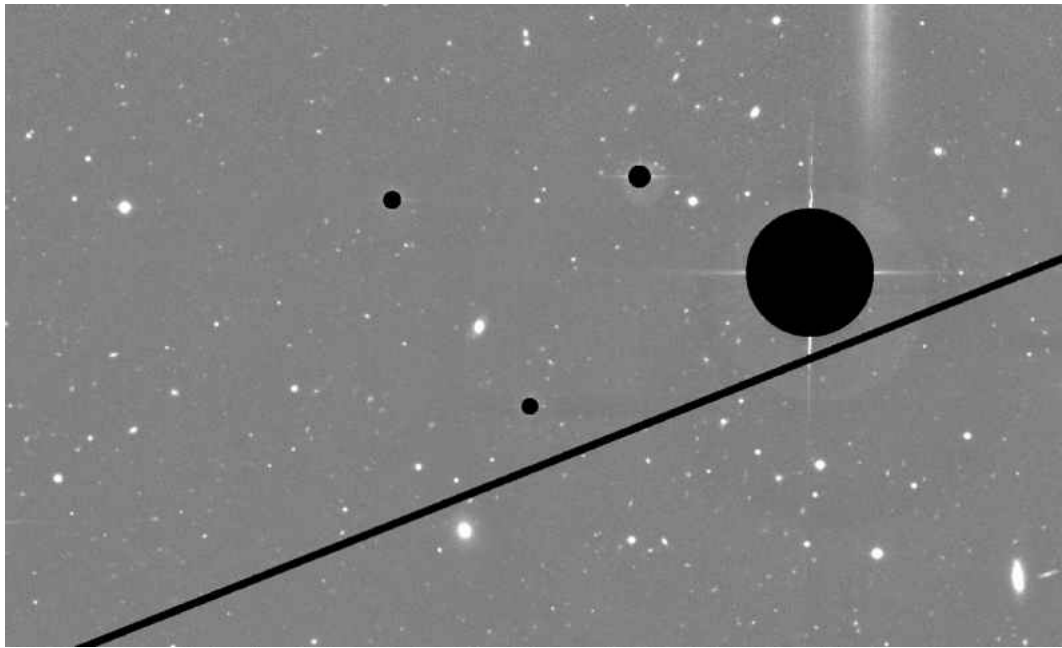


Figure 28. Three star masks and a satellite trail mask are depicted in black.

CHAPTER 3  
CALIBRATION MEASUREMENTS

**3.1 Photometric Calibration**

The first step in the calibration process is to determine the zeropoints for each image. For the  $r$ -band, stars in the images were matched to stars in the SDSS catalog by comparing each object position in the world coordinate system. The SDSS star measurements were made by fitting the brightness profile of each star with a Gaussian function (Stoughton et al., 2002). For each image, a cut was made in the SDSS  $m_r^2$  to remove fainter objects with larger errors, and in  $(m_{\text{SDSS}} - m_{\text{CFHT}})_r$  to remove outliers. The median of the difference between SDSS and CFHT was used to determine magnitude zeropoints. A plot of the magnitude differences after the zeropoint has been applied is shown in Fig. 29. The uncertainty in the zeropoints were determined by taking the standard deviation of the magnitude differences. The magnitudes from SDSS have been corrected for galactic dust using Schlegel et al. (1998), therefore the calibrated zeropoint includes an extinction correction.

While stellar magnitudes can be measured by fitting a Gaussian function, galaxy magnitudes cannot. Galaxy magnitudes in SDSS are measured using a composite of an exponential and de Vaucouleurs fit (The Sloan Digital Sky Survey, 2015). The composite

---

<sup>2</sup>In the following chapters, apparent and absolute magnitudes will be referenced frequently. Apparent magnitudes will be referred to using a lowercase  $m$ , and absolute magnitudes will be displayed as a capital  $M$ . A subscript will be used to denote the filter. Additionally, magnitudes measured for this project will use the label CFHT when compared to other works.



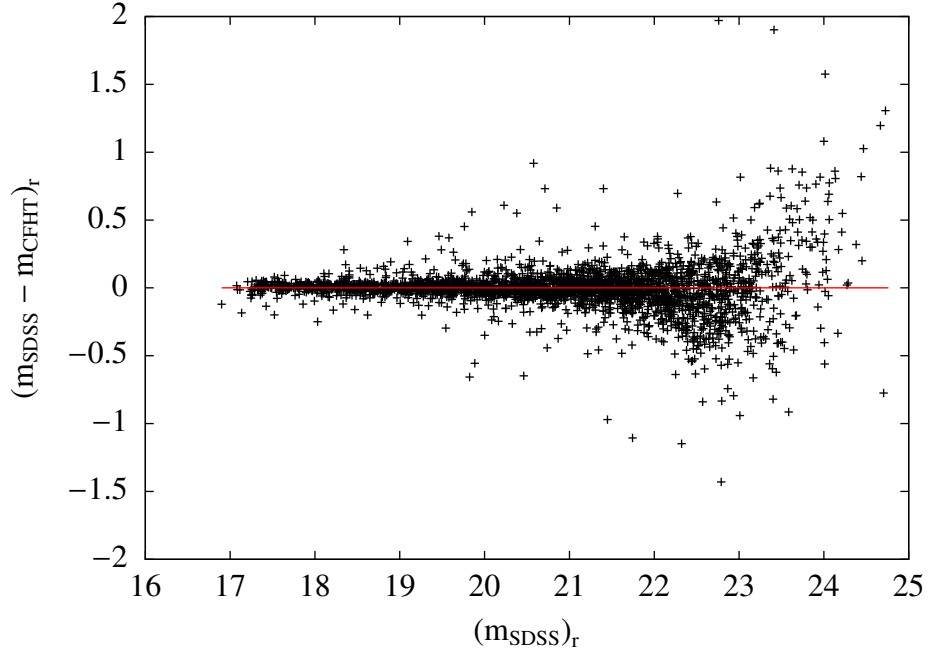


Figure 29. Comparison of SDSS and CFHT  $r$ -band magnitudes for Abell 1940 after the zeropoint was applied. A red horizontal line is shown at zero for reference.

magnitudes measured for all objects are given an offset so that, on average, the composite magnitude measured for a star is equal to the psf magnitude. However, it became apparent after calibrating the  $u$ -band that galaxy magnitudes between CFHT and SDSS differ by up to  $\approx 0.3$  magnitudes. Therefore, the  $u$ -band magnitudes were re-calibrated by only comparing galaxy magnitudes between the two catalogs. This comparison was done for galaxies whose uncertainty is  $< 0.1$  magnitude in both SDSS and CFHT. This measurement is subject to large scatter (Fig. 30), however, a large scatter is also present when comparing SDSS to the CFHT Legacy Survey (CFHTLS; Fig. 31). The magnitude difference between the CFHT and CFHTLS is not subject to the same large scatter (Fig. 32 and 33). A probable cause for this scatter is the red light leak in SDSS  $u$ -band magnitudes (Kowalski et al., 2009). The resulting magnitude zeropoints are shown in Table 2.

Table 2. Magnitude zeropoints for target clusters.

Cluster	$r$ -band zeropoint	$u$ -band zeropoint
A76	$25.94 \pm 0.04$	$25.01 \pm 0.18$
A98	$25.91 \pm 0.05$	$25.04 \pm 0.23$
A350	$25.96 \pm 0.04$	$25.33 \pm 0.14$
A351	$25.90 \pm 0.04$	$25.36 \pm 0.14$
A362	$25.96 \pm 0.05$	$25.15 \pm 0.14$
A655	$25.91 \pm 0.05$	$25.15 \pm 0.17$
A795	$25.85 \pm 0.05$	$25.23 \pm 0.18$
A1920	$25.98 \pm 0.05$	$25.28 \pm 0.16$
A1940	$25.96 \pm 0.05$	$25.30 \pm 0.18$
A2100	$25.99 \pm 0.04$	$25.18 \pm 0.16$
A2107	$25.86 \pm 0.04$	$25.10 \pm 0.14$
A2147	$25.77 \pm 0.04$	$25.22 \pm 0.19$
A2199	$25.93 \pm 0.04$	$25.21 \pm 0.16$
A2688	$25.59 \pm 0.04$	$25.10 \pm 0.19$

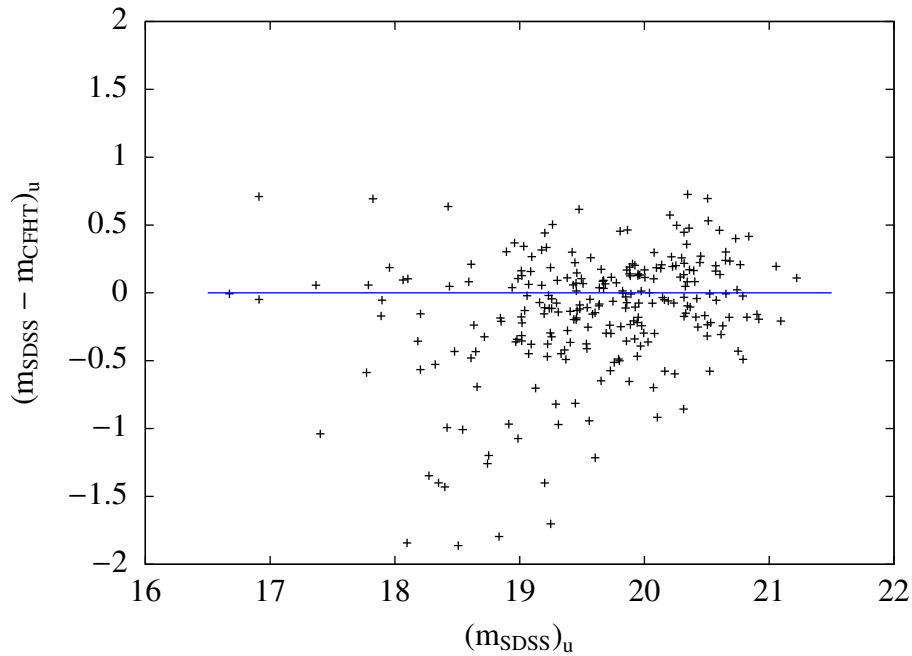


Figure 30. Comparison of SDSS and CFHT  $u$ -band galaxy magnitudes for galaxies with errors  $< 0.1$  magnitude located in the Abell 1940 image after the re-calibrated zeropoint was applied. A blue horizontal line is shown at zero as a reference.

### 3.2 Magnitude Limits

The magnitude depth of each image is checked to determine where object detection and color measurements become unreliable. First, the reliability of object detection was

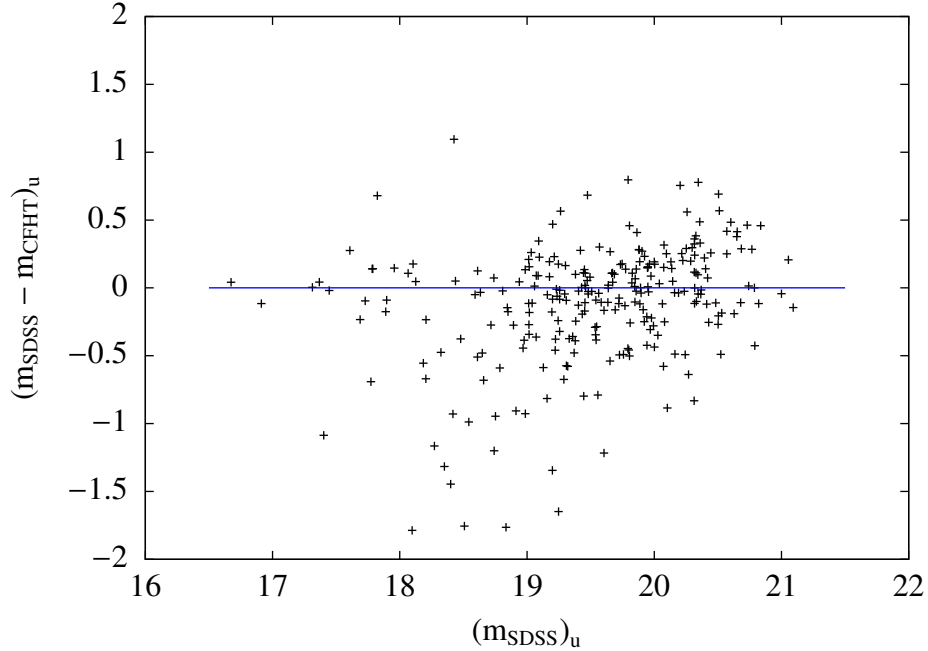


Figure 31. Comparison of CFHTLS and SDSS  $u$ -band galaxy magnitudes for galaxies with errors  $< 0.1$  magnitude located in the Abell 1940 image. A blue horizontal line is shown at zero as a reference.

determined by binning all galaxies in 0.1 magnitude bins. The number of galaxies is expected to increase as a power law with decreasing luminosity. As the data becomes incomplete at faint magnitudes, some galaxies are not detected due to their low luminosity and galaxy counts will turnover and start decreasing (Fig. 34). To ensure completeness, the catalog is considered complete 0.8 magnitude brighter than the turnover magnitude. Typically, cuts are made between 1.0 and 0.6 magnitude before the turnover. The choice of 0.8 magnitude was made to try to probe as deep into the dwarf population as possible while maintaining complete data.

The error in the color measurement is given by  $\sqrt{\sigma_r^2 + \sigma_u^2}$ , where  $\sigma_r$  and  $\sigma_u$  are the aperture magnitude error in the  $r$ - and  $u$ -band, respectively (Sec. 2.2.5). Galaxies will be cut from the catalog based on color to eliminate background clusters, therefore only objects with reasonable color errors can be used. To determine when the uncertainty in the

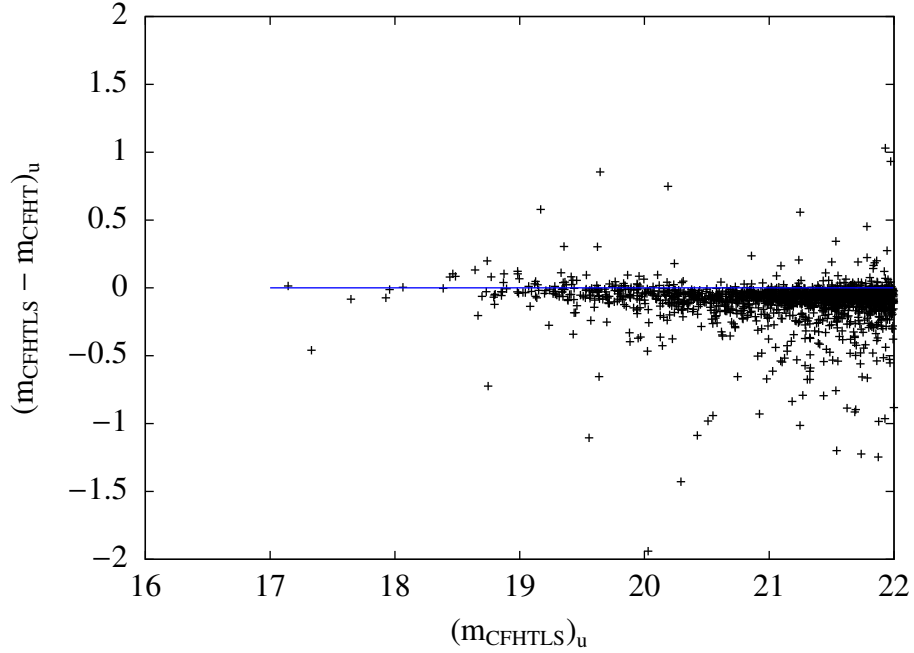


Figure 32. Comparison of CFHTLS and CFHT  $u$ -band galaxy magnitudes for galaxies with errors  $< 0.1$  magnitude located in the Abell 1940 image. A blue horizontal line is shown at zero as a reference. There is a slight offset between CFHT and CFHTLS.

color becomes large, the errors are first binned as a function of magnitude. Next, the median absolute deviation (MAD) is determined for each magnitude bin (Fig. 35). MAD, which is computed by taking the median of the all of the absolute deviations from the median, is a more robust statistic compared to the standard deviation. For normally distributed data, MAD is a factor of 1.4826 smaller than the standard deviation, and so the MAD value for each bin is increased by this factor. The median values of the binned color errors are fit using a cubic function, weighted by the inverse of the squared MAD value. From the cubic fit, the magnitude at which the color error becomes 0.2 is calculated via a root finder. The limiting magnitude for an image is either the completeness limit or the magnitude that the color uncertainty reaches 0.2 magnitude, whichever is smaller.

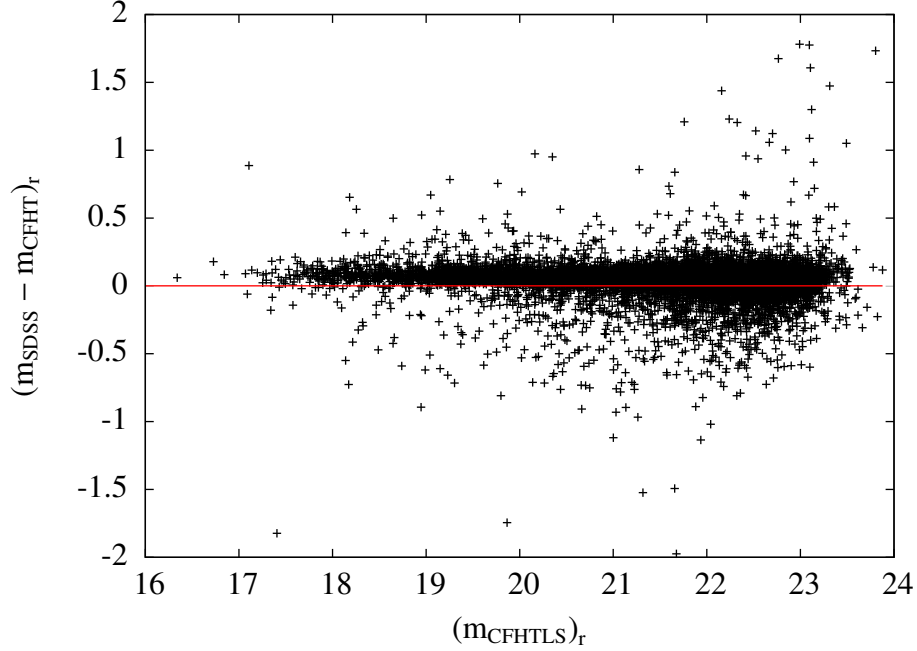


Figure 33. Comparison of CFHTLS and CFHT  $r$ -band galaxy magnitudes for galaxies with errors  $< 0.1$  magnitude located in the Abell 1940 image. A red horizontal line is shown at zero as a reference. There is a slight offset between CFHT and CFHTLS.

### 3.3 Comparing Sizes and Magnitudes between Galaxy Clusters

Due to the expansion of the universe, galaxy distance is related to redshift (Hubble, 1929).

For calculating distances, a flat  $\Lambda$ -CDM model of the universe is assumed with

$H_0 = 70 \text{ km s}^{-1} \text{ Mpc}^{-1}$ ,  $\Omega_\Lambda = 0.7$ , and  $\Omega_m = 0.3$ . The value of  $H_0$  is often parameterized

as  $H_0 = 100 h \text{ km s}^{-1} \text{ Mpc}^{-1}$ . For any quantity dependent upon  $H_0$ , I set  $h = 0.7$ .

#### 3.3.1 *K-Correction*

When observing a galaxy through a filter (e.g. Fig. 5), the rest frame wavelength of the light measured depends on the galaxy's redshift. In order to compare galaxies at various redshifts, this effect must be corrected for by applying a  $k$ -correction to each galaxy's magnitude. An exact  $k$ -correction requires information about the spectral energy distribution of the galaxy, which is unavailable for broad-band photometric data. The

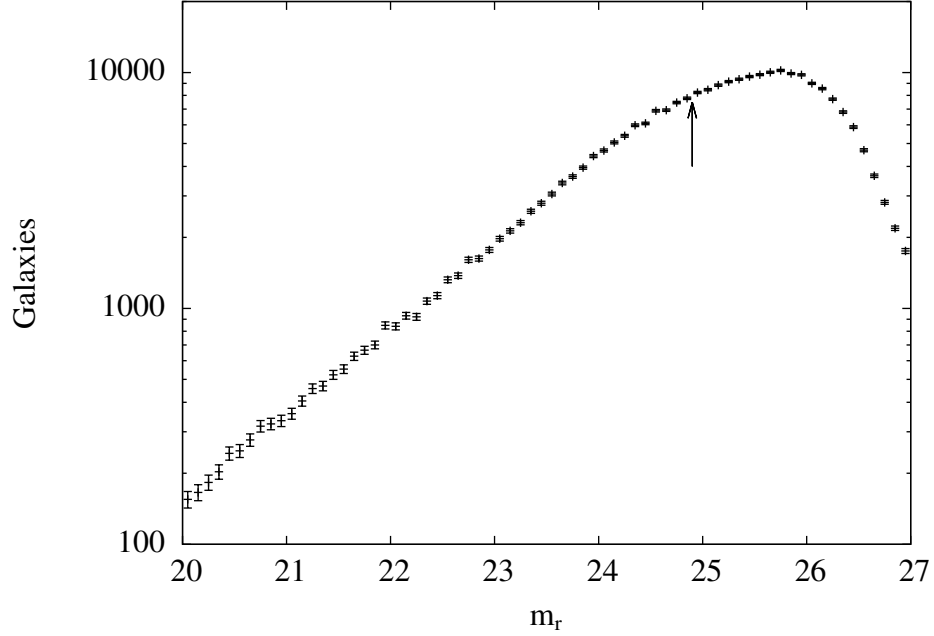


Figure 34. Count of galaxies versus  $r$ -band magnitude for Abell 1940. The completeness limit is taken to be 0.8 magnitude brighter than the turnover. The arrow indicates the completeness limit at  $m_r = 24.9$ .

usual strategy is to fit various spectral energy templates to the colors of each galaxy (Blanton & Roweis, 2007). However, this is impossible with only one color. Instead, a two dimensional polynomial in redshift and color is used to estimate the k-correction (Chilingarian et al., 2010; Chilingarian & Zolotukhin, 2012). The form of the correction is given by

$$\sum_{i=0}^5 \sum_{j=0}^3 a_{ij} z^i c^j, \quad (3.1)$$

where  $a_{ij}$  is the coefficient,  $z$  is the redshift, and  $c$  is the  $u - r$  color. The coefficients were fit to k-corrections measured on a large sample of galaxies in SDSS and the UKIRT Infrared Deep Sky Survey (Lawrence et al., 2007). The coefficients can be found in Tables 3 and 4.

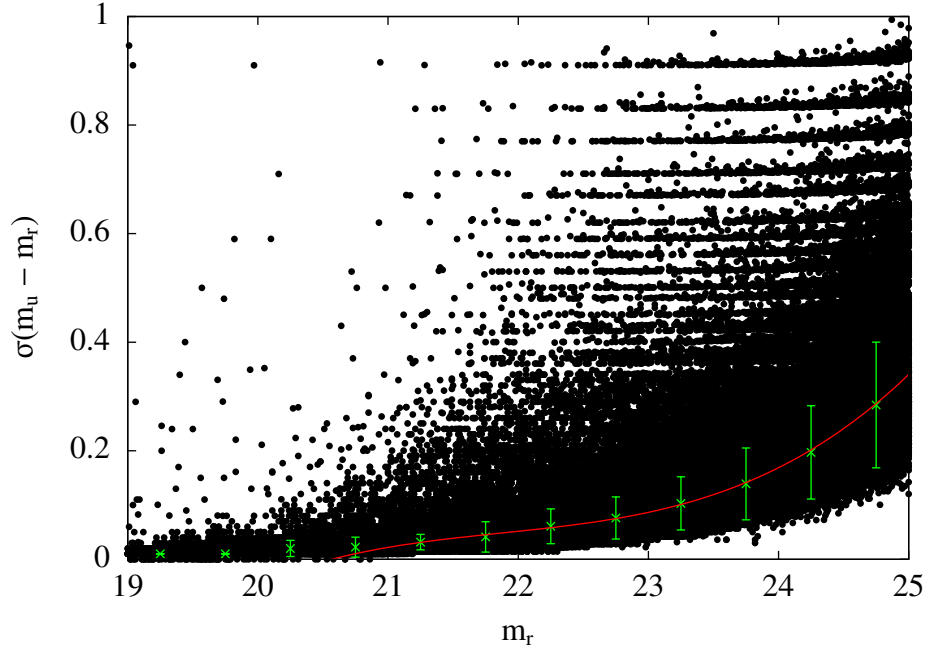


Figure 35. The error in the color as a function of  $r$ -band magnitude for Abell 1940. The data was binned in magnitude, and the median and the median absolute deviations were measured for color errors in each bin. A cubic function is used to interpolate when the median color uncertainty reaches 0.2 mag.

Table 3. Coefficients used in determining the  $r$ -band k-corrections. Values were obtained from <http://kcor.sai.msu.ru/>.

$a_{ij}$	$j=0$	1	2	3
$i=0$	0	0	0	0
1	3.03458	-1.50775	0.576228	-0.0754155
2	-47.8362	19.0053	-3.15116	0.286009
3	154.986	-35.6633	1.09562	0
4	-188.094	28.1876	0	0
5	68.9867	0	0	0

### 3.3.2 Luminosity and Angular Size Distances

In a  $\Lambda$ -CDM model, the distance used in determining absolute magnitudes and angular sizes of objects differ. They are both determined from the comoving distance,  $\chi$ , between the Earth and the galaxy cluster. The comoving distance scales with the expansion of the universe, so it remains constant between two objects that are not moving with respect to the Hubble flow (Hogg, 1999). The expansion of the universe is characterized by a scale

Table 4. Coefficients used in determining the  $u$ -band k-corrections. Values were obtained from <http://kcor.sai.msu.ru/>.

$a_{ij}$	$j=0$	1	2	3
$i=0$	0	0	0	0
1	10.3686	-6.12658	2.58748	-0.299322
2	-138.069	45.0511	-3.15116	0.95854
3	540.494	-43.7644	3.84259	0
4	-1005.28	10.9763	0	0
5	710.482	0	0	0

factor,  $a = \frac{1}{1+z}$ , where the scale of the universe at the present time is one. The comoving distance between the Earth and an object at a scale factor of  $a$  is given by

$$\chi = \frac{1000c}{H_0} \int_a^1 \frac{da}{\sqrt{a\Omega_m + a^4\Omega_\Lambda}}. \quad (3.2)$$

The luminosity distance,  $D_L$ , used in determining the total luminosity of an object is  $(1+z)\chi$ . When converting to absolute magnitude, which is the apparent magnitude of an object if it was 10 parsecs away, is determined using the distance modulus,  $\mu = 5 \log(d) - 5$ . The absolute magnitude is calculated by

$$M = m - \mu - \text{k-correction}. \quad (3.3)$$

The angular diameter distance is used to determine angular size as a function of redshift. It is related to the comoving distance by  $D_A = \chi/(1+z)$ . When computing the total area of a cluster, the quantity of interest is the scale when the galaxies emitted the light in degrees / Mpc. This scale is given by

$$\Theta \text{ Mpc}^{-1} = \frac{a}{D_A} \frac{180}{\pi}. \quad (3.4)$$



The scale factor  $a$  converts a comoving distance of one megaparsec into the correct physical distance at the redshift of the cluster.

The magnitude limit for each image is measured in terms of apparent magnitude, however, the limit in terms of absolute magnitude is also needed. The conversion to absolute magnitude is complicated by the k-correction. A comparison of k-corrections as a function of color for three different redshifts is presented in Fig. 36 for the  $r$ -band and in Fig. 37 for the  $u$ -band. Since the maximum k-correction occurs at the color extremum, the absolute magnitude limit is determined using the maximum possible k-correction computed between a very red and very blue color. The blue extremum is calculated at a color of 0, and the red extremum is computed using a color three  $\sigma$  redder than the color of the red-sequence (Sec. 3.4). The magnitude limits for each cluster are shown in Table 5

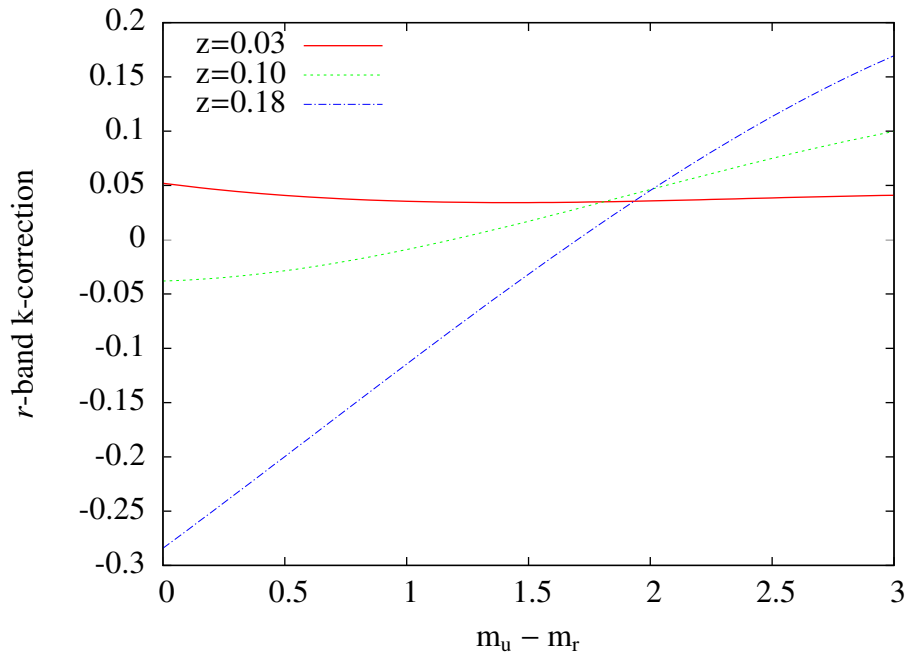


Figure 36. The  $r$ -band k-corrections for redshifts 0.03 (red solid line), 0.10 (green dotted line), and 0.18 (blue dot dashed line).

Since the k-corrections are fit as polynomials, faint galaxies with erroneously blue

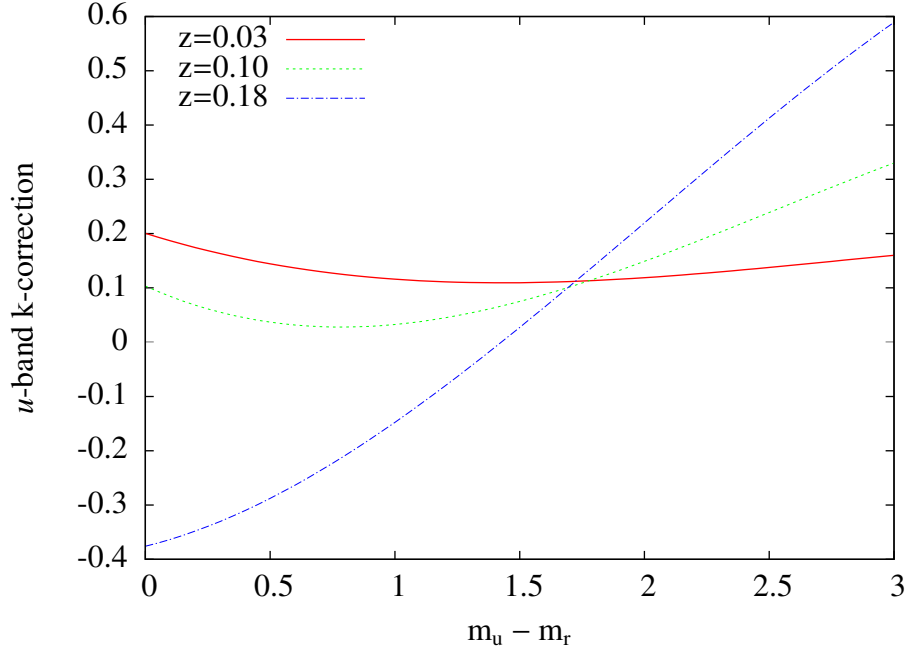


Figure 37. The  $u$ -band k-corrections for redshifts 0.03 (red solid line), 0.10 (green dotted line), and 0.18 (blue dot dashed line).

colors due to the high uncertainty in their magnitudes can lead to extremely large k-corrections. As will be seen in subsequent analysis, galaxies with colors redder than the red-sequence are cut, as they are background contamination. No such cut can be made for blue galaxies. A color histogram of all galaxies within the magnitude limit is shown in Fig. 38. Since the number of galaxies drops off sharply as galaxy color approaches zero, any galaxy with a color bluer than zero has its k-correction computed using a color of zero.

### 3.4 Cluster Red-Sequence

Each red-sequence is measured via a linear fit. First, the data is converted to absolute magnitudes, and then red-sequence galaxies are selected using two linear color-magnitude cuts (Fig. 39). This fit was carried out on galaxies within a radius of 0.5 Mpc of the cluster center. Additionally, the red-sequence was measured in terms of apparent magnitudes as several measurements require color cuts utilizing apparent magnitudes. These

Table 5. Magnitude limits for the cluster sample.

Cluster	$m_r$	$m_u$	$M_r$	$M_u$
A76	22.71	22.71	-13.60	-12.57
A98N	22.51	22.51	-15.96	-14.85
A98S	22.51	22.51	-15.96	-14.83
A350	24.34	24.34	-15.11	-14.52
A351	24.33	24.33	-14.29	-13.55
A362	24.35	24.35	-15.55	-15.14
A655	23.76	23.76	-15.16	-14.42
A795	23.00	23.00	-16.12	-15.13
A1920	24.30	24.30	-14.71	-14.06
A1940	24.24	24.24	-14.92	-14.26
A2100	24.20	24.20	-15.20	-14.75
A2107	23.03	23.03	-13.32	-12.43
A2147	23.25	23.25	-12.74	-11.83
A2199	23.94	23.94	-11.71	-10.76
A2688	22.39	22.39	-17.01	-15.96

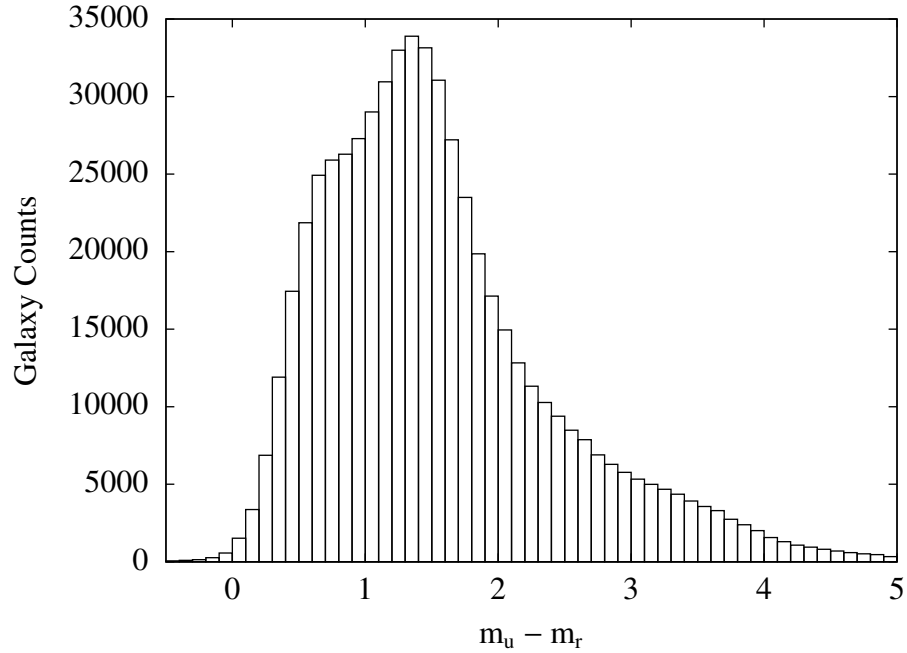


Figure 38. Histogram of galaxy color for all galaxies brighter than the magnitude limit.

red-sequences were fit within either a 0.5 or 1.0 Mpc radius of the cluster center. All of the slopes ( $m$ ) and y-intercepts ( $b$ ) can be found in Table 6. The standard errors were calculated using a bootstrap analysis with 1000 runs (Efron, 1979). The labels for the

parameters carry a subscript M or m, denoting that the fits were made with absolute or apparent magnitudes, respectively.

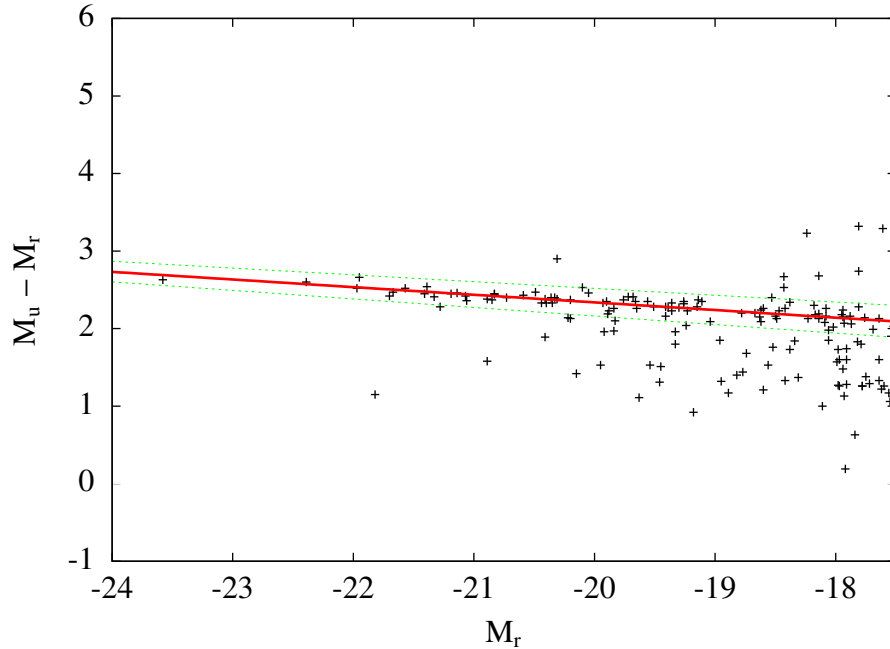


Figure 39. Color-Magnitude diagram for Abell 1940. The green dashed lines show the color cuts used when fitting the red-sequence. The resulting fit is shown as a red line.

Next, the dispersion of the red-sequence was measured utilizing red-sequence fits made with absolute magnitudes. The objects were translated and rotated so that the red-sequence is centered on a color of zero (Fig. 40). A histogram of rectified colors was constructed for each cluster using galaxies that are within 0.5 Mpc of the cluster center and brighter than  $M_r = -18$ . An additional background histogram is measured by using the same procedure on a background field. For galaxy clusters with redshifts  $\geq$  that of Abell 351, the background was taken from the same image as the cluster, three Mpc away from the cluster center. For lower redshift clusters, there is less surrounding area to determine the background count, so a composite background is constructed from all of the backgrounds of the higher redshift clusters. Only the backgrounds whose limiting

Table 6. Measured properties of target clusters.

Cluster	$m_M^a$	$b_M^a$	$\sigma$	$m_m^b$	$b_m^b$	$\lambda$	$\sigma_v$ (km/s)	$r_{200}$ (Mpc)
A76	$-0.120 \pm 0.012$	$-0.07 \pm 0.24$	0.072	$-0.132 \pm 0.007$	$4.56 \pm 0.11$	$44.0 \pm 7.0$	$492^{+74}_{-74}$	$1.19 \pm 0.18$
A98N	$-0.080 \pm 0.013$	$0.49 \pm 0.26$	0.102	$-0.065 \pm 0.015$	$3.45 \pm 0.26$	$57.3 \pm 8.9$		$1.49 \pm 0.66$
A98S	$-0.122 \pm 0.008$	$-0.31 \pm 0.16$	0.089	$-0.103 \pm 0.019$	$4.21 \pm 0.33$	$116.8 \pm 12.3$		$1.97 \pm 0.90$
A350	$-0.091 \pm 0.006$	$0.53 \pm 0.12$	0.075	$-0.100 \pm 0.012$	$4.57 \pm 0.24$	$26.5 \pm 5.2$		$1.10 \pm 0.43$
A351	$-0.093 \pm 0.013$	$0.55 \pm 0.26$	0.079	$-0.111 \pm 0.015$	$4.68 \pm 0.29$	$35.3 \pm 6.0$	$510^{+118}_{-118}$	$1.20 \pm 0.28$
A362	$-0.061 \pm 0.010$	$1.17 \pm 0.21$	0.098	$-0.093 \pm 0.012$	$4.61 \pm 0.24$	$90.4 \pm 9.6$		$1.78 \pm 0.80$
A655	$-0.102 \pm 0.007$	$0.23 \pm 0.14$	0.090	$-0.105 \pm 0.012$	$4.44 \pm 0.22$	$111.2 \pm 10.6$	$736^{+78}_{-78}$	$1.71 \pm 0.18$
A795	$-0.074 \pm 0.008$	$0.87 \pm 0.16$	0.104	$-0.089 \pm 0.010$	$4.28 \pm 0.19$	$116.1 \pm 11.0$	$778^{+61}_{-50}$	$1.80 \pm 0.13$
A1920	$-0.097 \pm 0.006$	$0.43 \pm 0.11$	0.090	$-0.103 \pm 0.012$	$4.55 \pm 0.24$	$66.0 \pm 8.2$	$562^{+84}_{-84}$	$1.31 \pm 0.27$
A1940	$-0.098 \pm 0.006$	$0.37 \pm 0.12$	0.084	$-0.110 \pm 0.010$	$4.67 \pm 0.19$	$77.8 \pm 8.8$	$785^{+118}_{-118}$	$1.82 \pm 0.27$
A2100	$-0.085 \pm 0.007$	$0.62 \pm 0.13$	0.080	$-0.095 \pm 0.009$	$4.42 \pm 0.17$	$54.6 \pm 7.6$		$1.46 \pm 0.64$
A2107	$-0.114 \pm 0.005$	$0.07 \pm 0.10$	0.064	$-0.103 \pm 0.008$	$4.15 \pm 0.13$	$43.6 \pm 7.0$	$674^{+67}_{-52}$	$1.64 \pm 0.14$
A2147	$-0.118 \pm 0.007$	$0.01 \pm 0.13$	0.105	$-0.120 \pm 0.007$	$4.33 \pm 0.11$	$77.3 \pm 10.3$	$821^{+123}_{-123}$	$2.00 \pm 0.30$
A2199	$-0.112 \pm 0.006$	$0.20 \pm 0.11$	0.113	$-0.124 \pm 0.004$	$4.47 \pm 0.07$	$85.1 \pm 9.7$	$780^{+52}_{+44}$	$1.90 \pm 0.12$
A2688	$-0.078 \pm 0.011$	$0.82 \pm 0.22$	0.122	$-0.090 \pm 0.010$	$4.39 \pm 0.19$	$34.1 \pm 5.9$		$1.22 \pm 0.50$

<sup>a</sup> Measured using absolute magnitudes.

<sup>b</sup> Measured using apparent magnitudes.

magnitude is  $\geq$  the cluster being measured are used. The background histograms are scaled by the ratio of the cluster area to the total background area, and then subtracted from the cluster histograms. The error on the number of measured cluster galaxies is calculated by  $\sqrt{N}$ , where  $N$  is the number of galaxies. This error analysis assumes the formation of galaxies is a Poisson process (Schechter, 1976). The error in the number of background counts is the square root of the number of background galaxies expected in the cluster area, as it also follows a Poisson distribution. Finally, a Gaussian function is fit to the red-sequence in the color histogram for each cluster using the Levenberg–Marquardt method (Marquardt, 1963). The results are displayed in Table 6 under the  $\sigma$  heading. The histograms with the Gaussian fit overlaid are shown in Figs. 41–55.

All of the background subtracted measurements require measuring the total angular area covered by a set of data. Each area was computed by checking if each pixel in the image satisfies the following requirements in the  $r$ -band image:

1. The center of the pixel is within the area of interest.
2. The pixel contains valid data.
3. The pixel is not located in any mask.

If the pixel passed these checks, the pixel coordinates are translated to the world coordinate system and then into the physical coordinates of the associated  $u$ -band image. If the  $u$ -band pixel passes those same conditions, the pixel area is added to the total.

### 3.5 Cluster Richness

The ideal property for comparing clusters is total mass. This property, however, is difficult to measure directly, and instead a mass proxy, richness, is used. Each cluster’s richness is

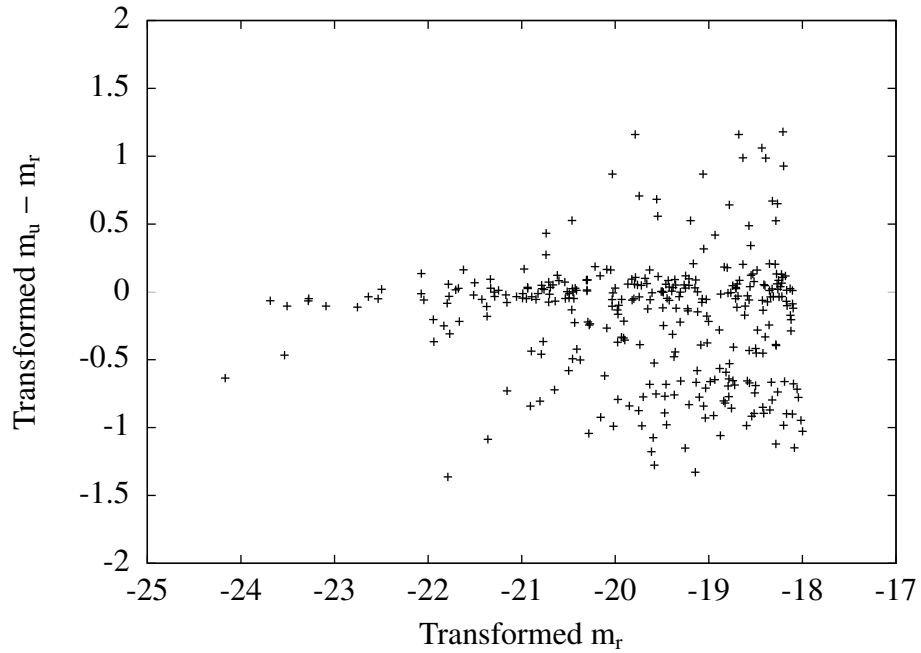


Figure 40. Rectified color-magnitude diagram for Abell 1940. The color and magnitude of each object has been translated and rotated so that the red-sequence slope is zero.

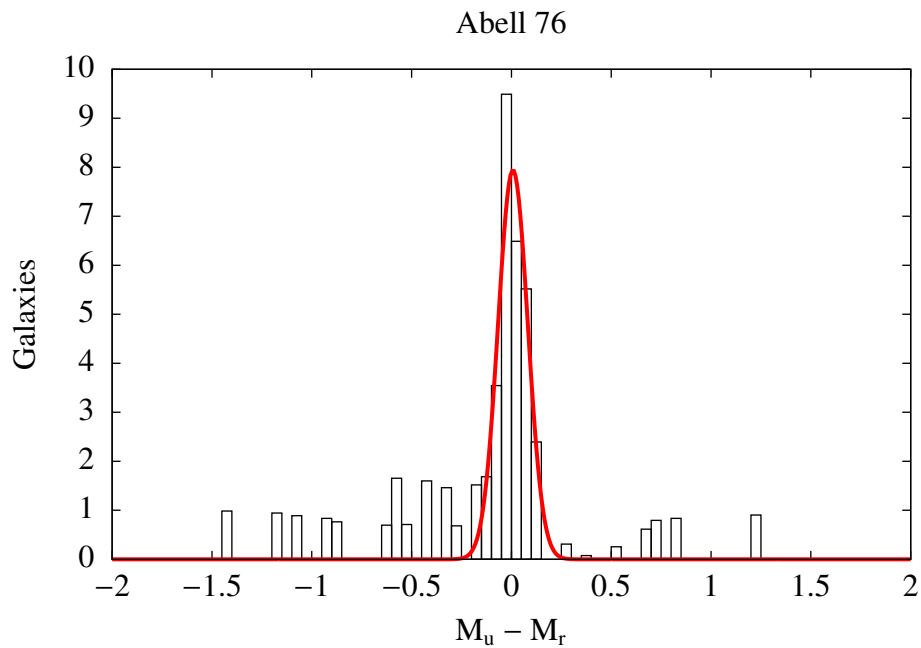


Figure 41. Background corrected color histogram for Abell 76 for galaxies within  $0.5 r_{200}$  of the cluster center.

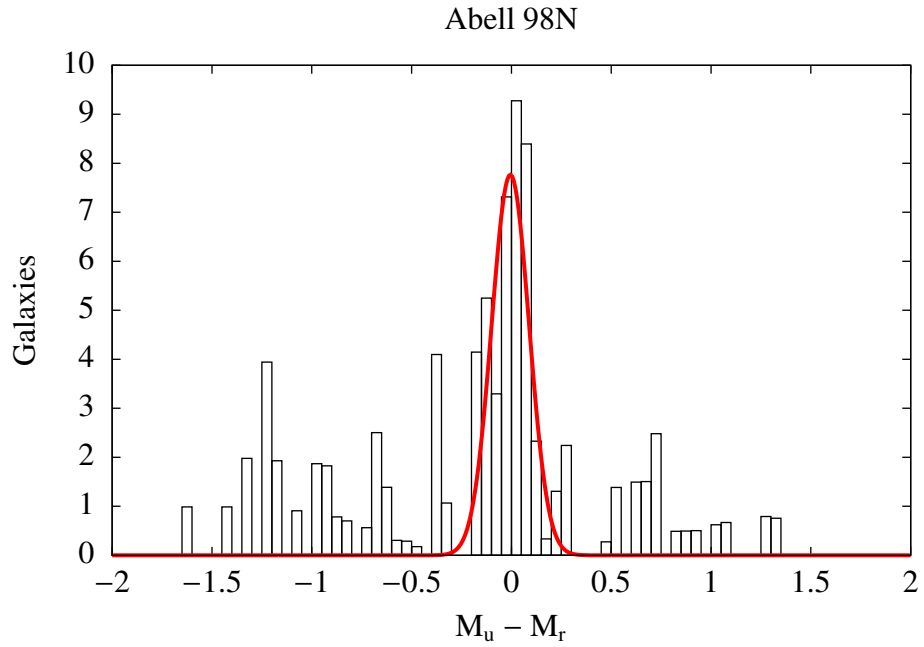


Figure 42. Background corrected color histogram for Abell 98N for galaxies within  $0.5 r_{200}$  of the cluster center.

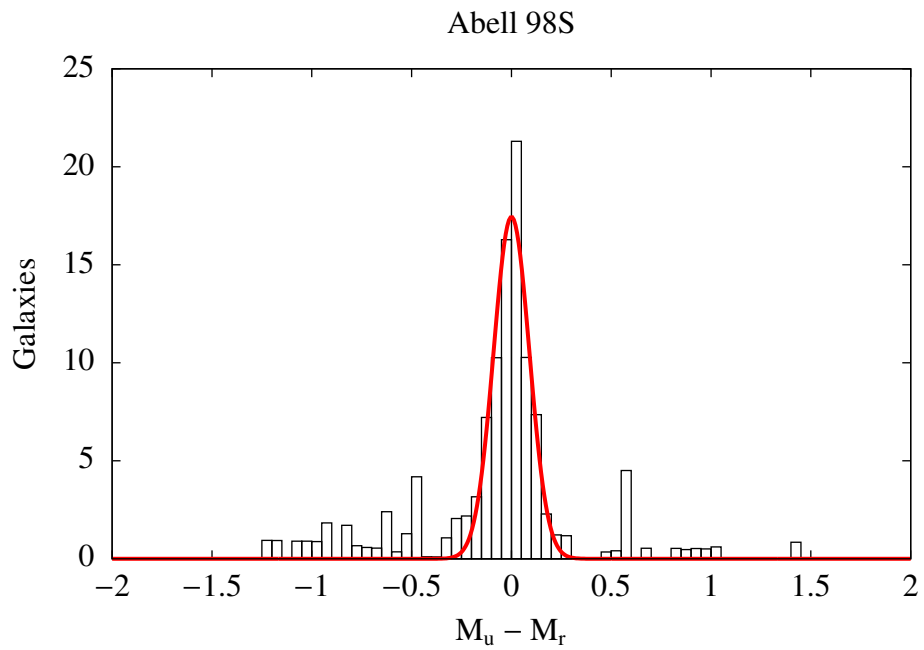


Figure 43. Background corrected color histogram for Abell 98S for galaxies within  $0.5 r_{200}$  of the cluster center.



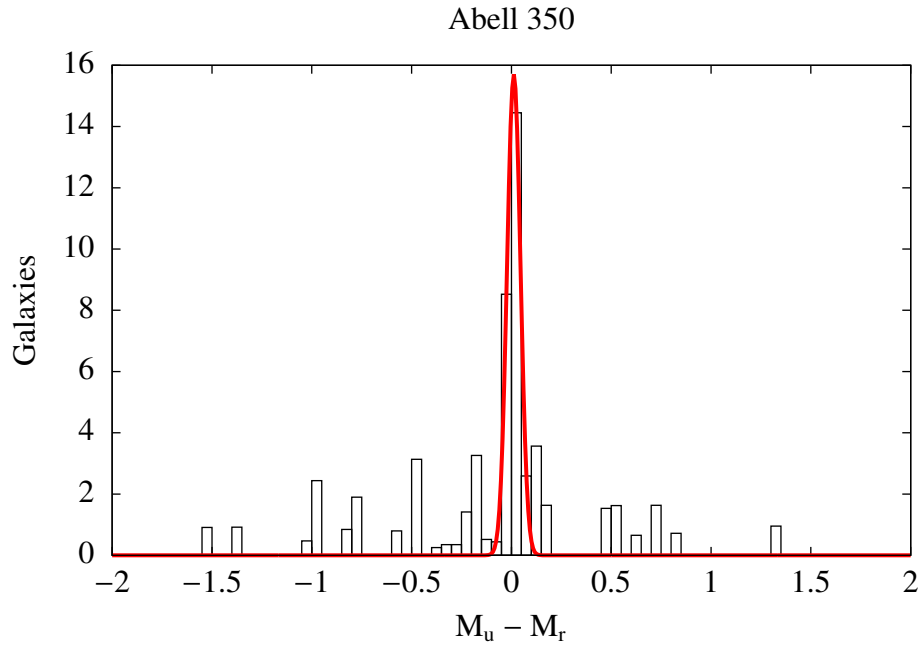


Figure 44. Background corrected color histogram for Abell 350 for galaxies within  $0.5 r_{200}$  of the cluster center.

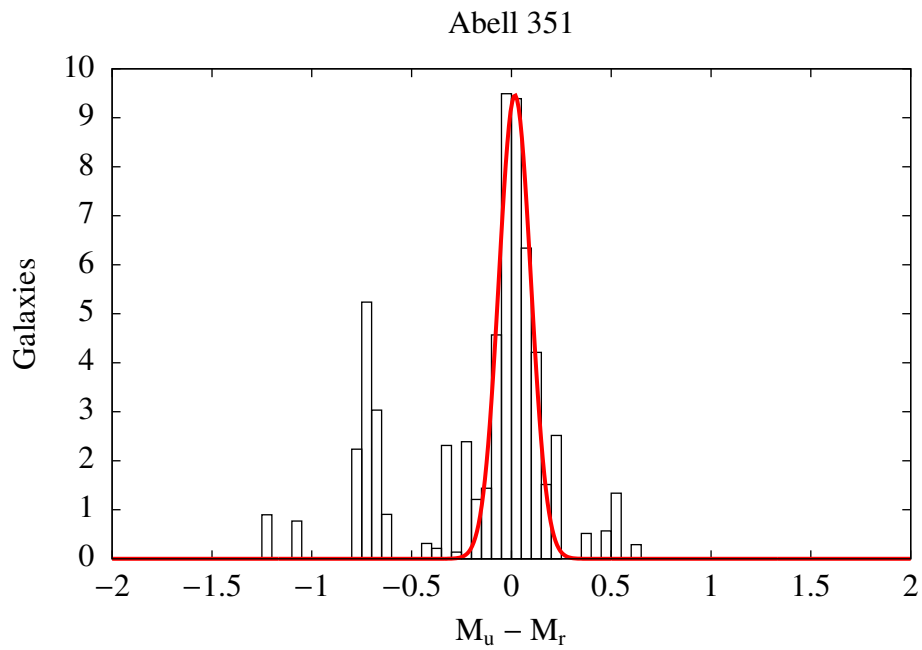


Figure 45. Background corrected color histogram for Abell 351 for galaxies within  $0.5 r_{200}$  of the cluster center. The small group at a rectified color of  $-0.75$  is a lower redshift system.

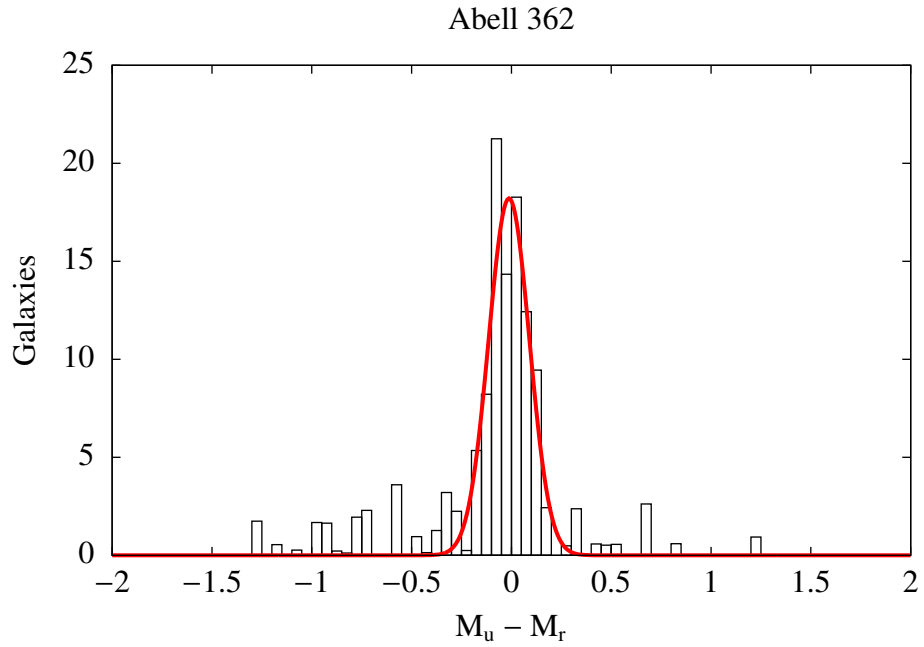


Figure 46. Background corrected color histogram for Abell 362 for galaxies within  $0.5 r_{200}$  of the cluster center.

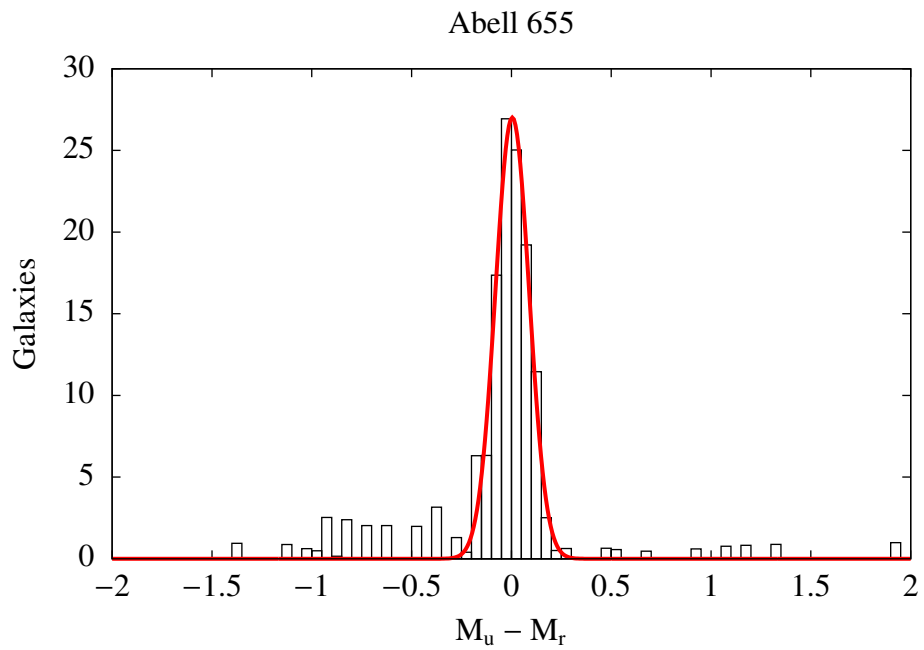


Figure 47. Background corrected color histogram for Abell 655 for galaxies within  $0.5 r_{200}$  of the cluster center.

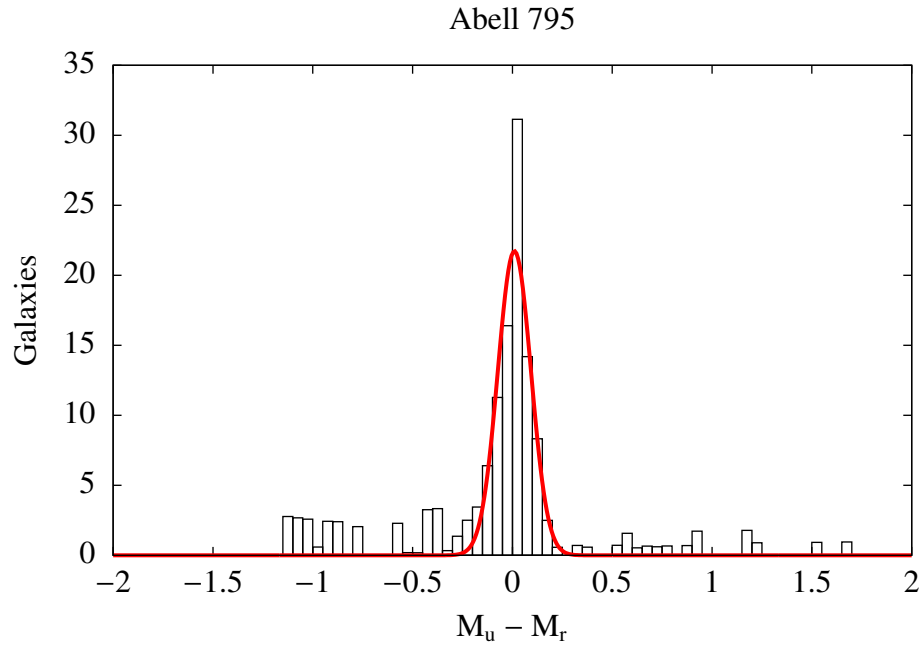


Figure 48. Background corrected color histogram for Abell 795 for galaxies within  $0.5 r_{200}$  of the cluster center.

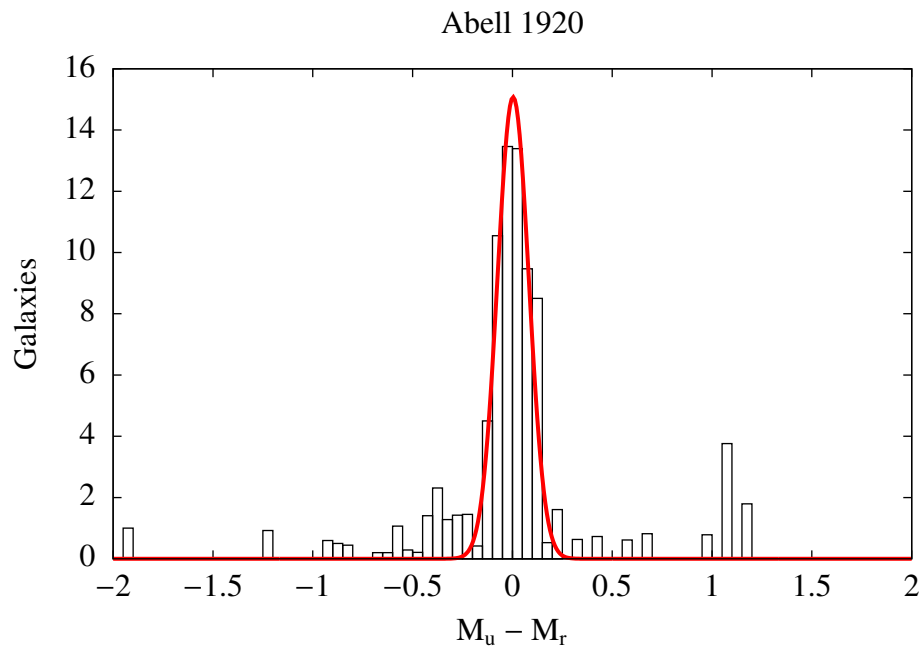


Figure 49. Background corrected color histogram for Abell 1920 for galaxies within  $0.5 r_{200}$  of the cluster center.

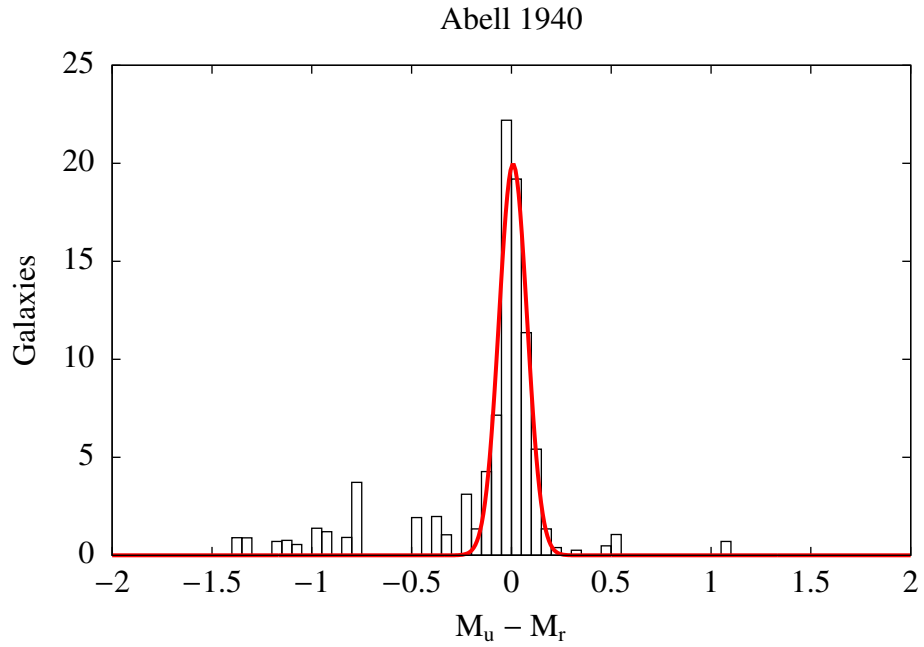


Figure 50. Background corrected color histogram for Abell 1940 for galaxies within  $0.5 r_{200}$  of the cluster center.

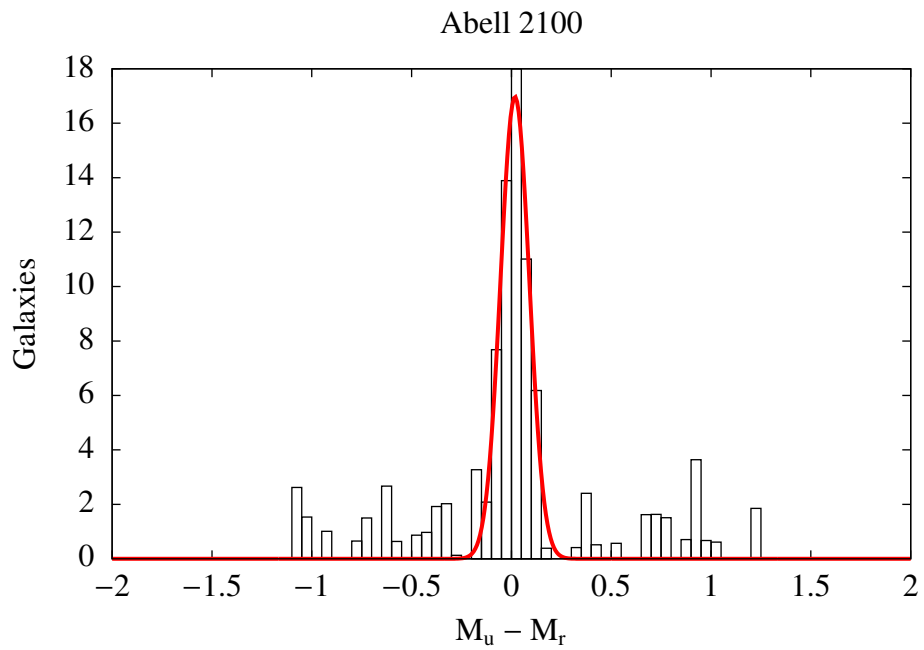


Figure 51. Background corrected color histogram for Abell 2100 for galaxies within  $0.5 r_{200}$  of the cluster center.

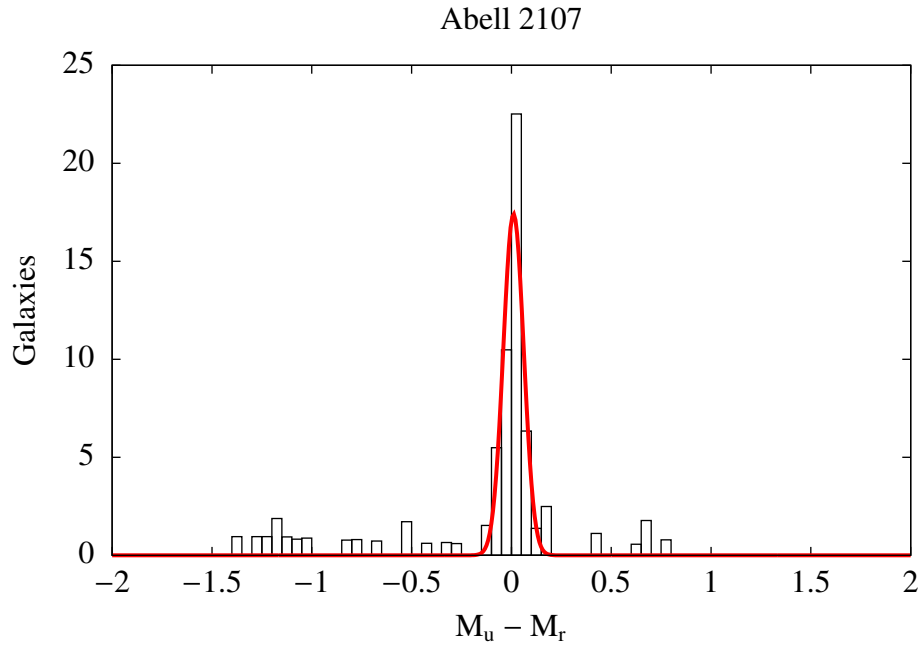


Figure 52. Background corrected color histogram for Abell 2107 for galaxies within  $0.5 r_{200}$  of the cluster center.

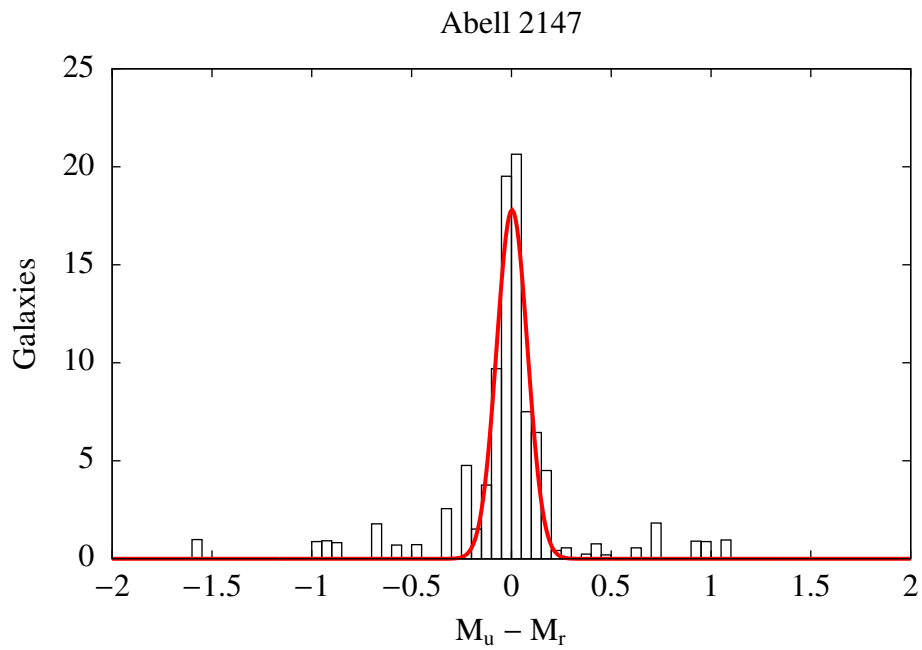


Figure 53. Background corrected color histogram for Abell 2147 for galaxies within  $0.5 r_{200}$  of the cluster center.

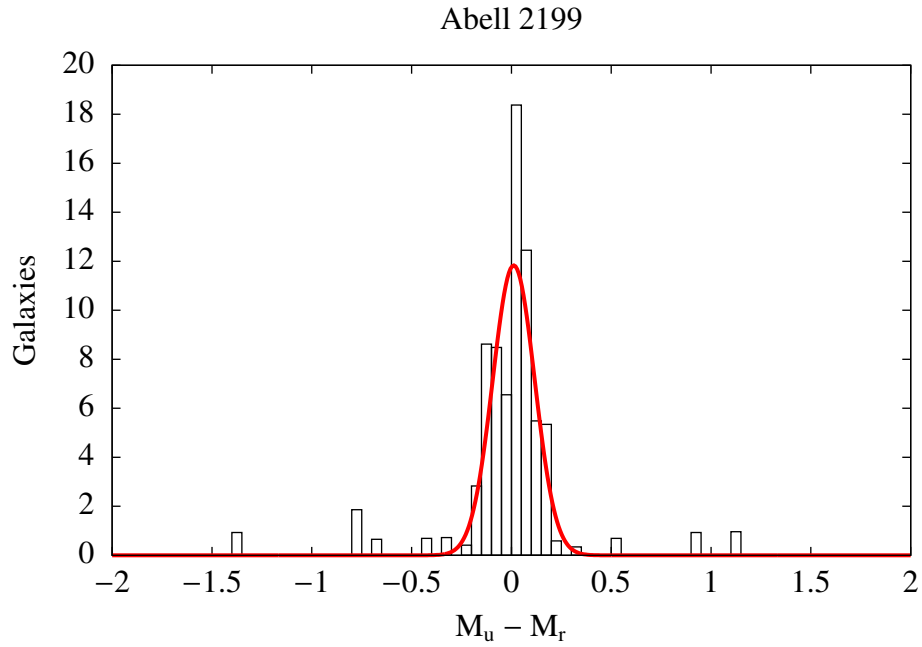


Figure 54. Background corrected color histogram for Abell 2199 for galaxies within  $0.5 r_{200}$  of the cluster center.

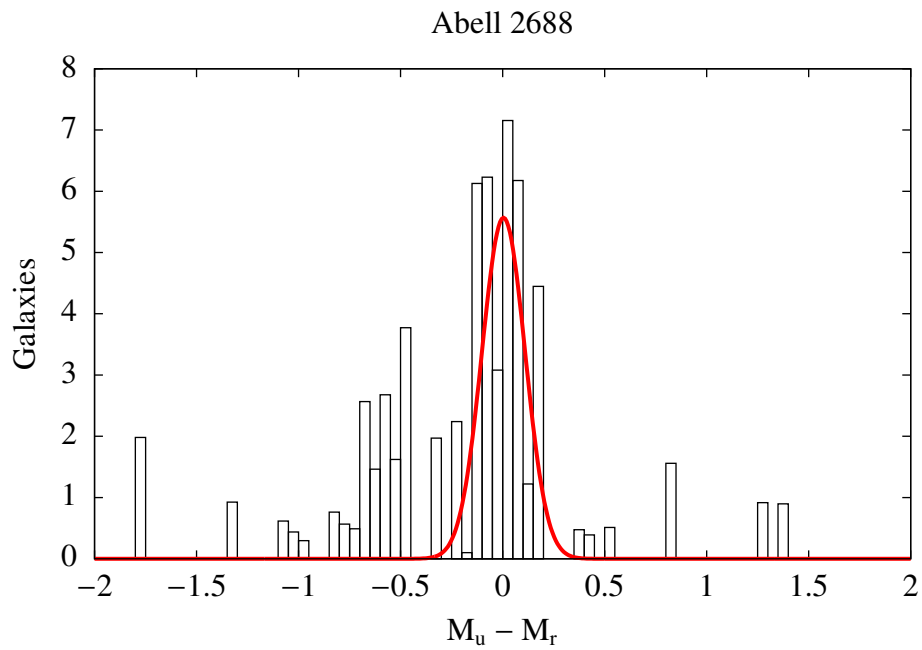


Figure 55. Background corrected color histogram for Abell 2688 for galaxies within  $0.5 r_{200}$  of the cluster center. The small group at a rectified color of  $-0.6$  is a lower redshift system.

calculated using the lambda richness measurement (Rykoff et al., 2012). This method estimates the number of cluster galaxies by calculating the probability that each galaxy is a member of the cluster.

The following procedure is adapted from Rozo et al. (2009). If  $\mathbf{x}$  is a vector of the measurements of a galaxy (i.e. magnitude, color, etc.), then the probability that the galaxy is a member of the cluster is given by

$$p(\mathbf{x}) = \frac{\lambda u(\mathbf{x}|\lambda)}{\lambda u(\mathbf{x}|\lambda) + b(\mathbf{x})}, \quad (3.5)$$

where  $\lambda$  is the number of cluster galaxies,  $u$  is the galaxy density profile normalized to 1, and  $b$  is the background density. The background density is determined by binning a background catalog of galaxies in magnitude and color. Each bin is multiplied by

$$\frac{1}{(A)(cbin)(mbin)}, \quad (3.6)$$

where  $A$  is the total angular area of the background in square degrees,  $cbin$  is the color bin size, and  $mbin$  is the magnitude bin size. This converts the background density into units of counts/square degree/mag/mag. For each cluster, the background density is converted to counts/square Mpc/mag/mag based on the cluster's redshift.

The density function in eq. 3.5 depends on  $R$ , the distance from the center of the cluster,  $m$ , the apparent magnitude, and  $c$ , the color. It is defined as

$$u(\mathbf{x}) = \{2\pi R \Sigma(R/R_s)\} \phi(m) G(c), \quad (3.7)$$

where  $\Sigma(R)$  is the radial density profile,  $\phi(m)$  is a Schechter function, and  $G(c)$  is a Gaussian function centered on the red-sequence. The radial density profile is the surface density of a Navarro-Frenk-White profile, using a length scale of  $R_s$  (Navarro et al., 1995; Bartelmann, 1996). For  $R/R_s > 1$  the profile is

$$\Sigma(R) = \frac{\Sigma_0}{(R/R_s)^2 - 1} \left( 1 - \frac{2}{\sqrt{(R/R_s)^2 - 1}} \tan^{-1} \left( \frac{\sqrt{(R/R_s) - 1}}{\sqrt{(R/R_s) + 1}} \right) \right), \quad (3.8)$$

where  $R_s$  is set to  $15 h^{-1}$  (Rykoff et al., 2012). If  $R/R_s < 1$ , some terms become imaginary,

$$\Sigma(R) = \frac{\Sigma_0}{(R/R_s)^2 - 1} \left( 1 - \frac{2}{i \sqrt{(1 - (R/R_s))^2}} \tan^{-1} \left( \frac{i \sqrt{1 - (R/R_s)}}{\sqrt{(R/R_s) + 1}} \right) \right). \quad (3.9)$$

Using the identity that  $\tan^{-1}(ix) = i \tanh^{-1}(x)$ ,

$$\Sigma(R) = \frac{\Sigma_0}{(R/R_s)^2 - 1} \left( 1 - \frac{2}{i \sqrt{1 - (R/R_s)^2}} i \tanh^{-1} \left( \frac{\sqrt{1 - (R/R_s)}}{\sqrt{(R/R_s) + 1}} \right) \right), \quad (3.10)$$

$$\Sigma(R) = \frac{\Sigma_0}{(R/R_s)^2 - 1} \left( 1 - \frac{2}{\sqrt{1 - (R/R_s)^2}} \tanh^{-1} \left( \frac{\sqrt{1 - (R/R_s)}}{\sqrt{(R/R_s) + 1}} \right) \right). \quad (3.11)$$

Since this function diverges as  $R \rightarrow 0$ ,  $\Sigma(R)$  is defined to be a constant value for  $R/R_s < 10 h^{-1}$  kpc. The inner value of  $\Sigma(R)$  is chosen so that  $\Sigma(R)$  is continuous. The normalization constant,  $\Sigma_0$ , is defined so that

$$\int_0^{R_c} 2\pi R \Sigma(R) = 1, \quad (3.12)$$

where  $R_c$  defines the maximum radius of the cluster.

The Schechter function in Eq. 3.7,  $\phi(m)$ , is given by



$$\phi(m) = \phi_0 10^{-0.4(m-m^*)(\alpha+1)} \exp(-10^{-0.4(m-m^*)}), \quad (3.13)$$

where  $\alpha$  is set to 0.8 in order to be consistent with Rozo et al. (2009). The characteristic magnitude,  $M^*$ , was measured by Barkhouse et al. (2007). After converting to the appropriate band,  $M^* = -21.47$ . This value is transformed to the apparent magnitude at the cluster's redshift using a k-correction assuming the galaxy is in the red-sequence. A magnitude cutoff of  $m^* + 1.75$  is employed so that all fainter galaxies are not included in the measurement. Finally, the normalization factor,  $\phi_0$ , is chosen so that

$$\int_{-\infty}^{m^*+1.75} \phi(m) = 1. \quad (3.14)$$

The color filter term,  $G(c)$ , is a Gaussian function with the measured standard deviation given in Table 6. Due to the slope of the red-sequence, the mean of the Gaussian is adjusted so that it is always centered on the red-sequence. Explicitly, the function is

$$G(c) = \frac{1}{\sqrt{2\pi}\sigma} \exp\left(-\frac{(c - r(m))^2}{2\sigma^2}\right), \quad (3.15)$$

where  $r(m)$  is the linear function fit to the red-sequence.

The total number of galaxies in a cluster is

$$\lambda = \Sigma p(\mathbf{x}|\lambda) = \Sigma_{R < R_c} \frac{\lambda u(\mathbf{x}|\lambda)}{\lambda u(\mathbf{x}|\lambda) + b(\mathbf{x})}. \quad (3.16)$$

The maximum radius,  $R_c$ , is given by

$$R_c = R_0 \left( \frac{\lambda}{100} \right)^\beta. \quad (3.17)$$

If  $\beta > 0$ , the cluster size used to estimate the richness scales with  $\lambda$ . However, since the CFHT image has missing data between chips and defects, a fixed radius is used so that the richness can be compensated for missing area. Therefore,  $\beta$  is set to zero. Following Rykoff et al. (2012) for a fixed radius,  $R_c$  is set to  $0.9 h^{-1}$  Mpc. Finally,  $\lambda$  is calculated by solving

$$\lambda - \Sigma p(\mathbf{x}|\lambda) = \lambda - \Sigma_{R < R_c} \frac{\lambda u(\mathbf{x}|\lambda)}{\lambda u(\mathbf{x}|\lambda) + b(\mathbf{x})} = 0 \quad (3.18)$$

with a root finder. The error of the measurement is calculated as  $\sqrt{\lambda}$ , as the dominant source of error is from the scatter in the number of expected galaxies for a cluster (Rozo et al., 2011). The resulting  $\lambda$  is scaled by the fraction of missing data in the  $0.9 h^{-1}$  Mpc region. The scaled  $\lambda$  measurements are shown in Table 6.

There are six galaxy clusters which have X-ray flux measurements available in the literature (Ebeling et al., 1998). Since X-ray luminosity is used to estimate cluster mass (Balland & Blanchard, 1997), it can be used to check if the  $\lambda$  measurements are reasonable. A comparison of the two is shown in Fig. 56. The seemingly tight correlation between the two is no surprise as the parameters were tuned by Rykoff et al. (2012) to reduce scatter between  $\lambda$  and X-ray luminosity. For each cluster, the X-ray luminosity is calculated from its flux measurement by

$$L_x = AF_x, \quad (3.19)$$

where  $A$  is the surface area of a sphere whose radius is the luminosity distance to the cluster, and  $F_x$  is the X-ray flux.

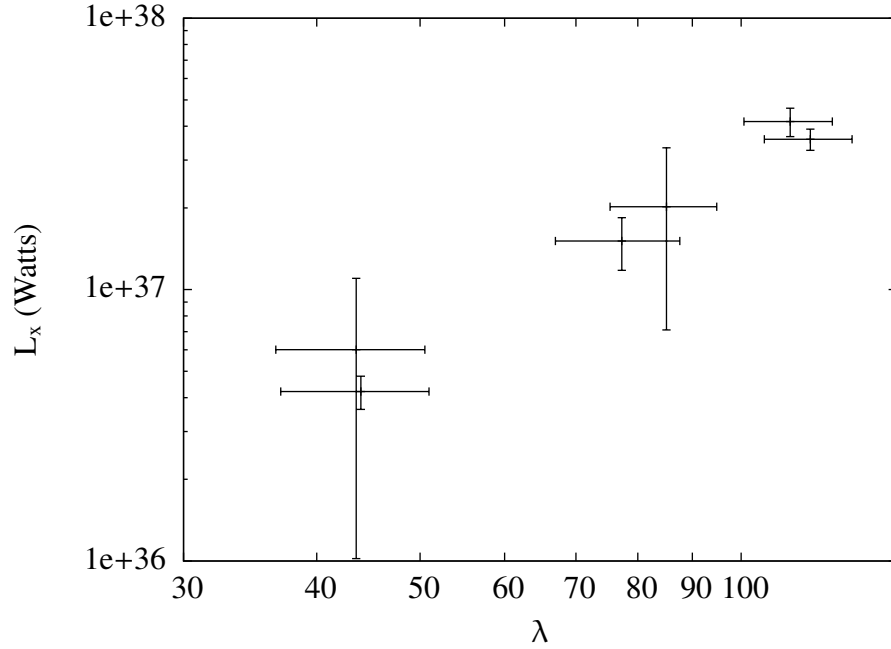


Figure 56. The  $\lambda$  richness versus X-ray luminosity for Abell 76, 655, 795, 2107, 2199, and 2147.

### 3.6 Dynamical Radius

To fairly compare clusters of various richness, each cluster needs to be scaled according to its mass. The scaling radius chosen,  $r_{200}$ , is defined as the radius of a sphere within which the average density is 200 times the critical density of the universe. The critical density is given by

$$\rho_c = \frac{3H^2}{8\pi G}. \quad (3.20)$$

This value is often used as an estimate for the size of a cluster because the maximum density of a cluster after it reaches equilibrium, for the spherical collapse model (Kravtsov & Borgani, 2012), is  $\approx 178$  times the mean density of the universe. For nine clusters from my sample, velocity dispersion measurements,  $\sigma_v$ , are available from the literature (Struble & Rood, 1999; Oegerle & Hill, 2001; Popesso et al., 2007; Tovmassian & Andernach, 2012; Rines et al., 2013). A velocity dispersion measurement is available for Abell 98, but no distinction was made between the northern and southern components, therefore it was not used. The  $r_{200}$  values are calculated from the velocity dispersion following Demarco et al. (2010),

$$r_{200} = \frac{\sqrt{3}\sigma_v}{10H(z)}, \quad (3.21)$$

where

$$H(z) = H_0 \sqrt{\Omega_m(1+z)^3 + \Omega_\Lambda}. \quad (3.22)$$

In order to estimate  $r_{200}$  for the rest of the sample, a linear line is fit to  $\log(\lambda)$  versus  $\log(r_{200})$  using the method of bivariate correlated errors and intrinsic scatter (BCES; Akritas & Bershady, 1996). The error measurements given for  $\sigma_v$  are usually asymmetric and therefore an average of the two errors was used for fitting. Unfortunately, some velocity dispersion measurements from the literature do not report uncertainties. For these values, an error of 15% was assumed, which is a typical relative uncertainty for velocity dispersion measurements. The result of the fit, shown in Fig. 57, is

$$\log(r_{200}) = (0.39 \pm 0.10) \log(\lambda) - (0.51 \pm 0.19). \quad (3.23)$$

The velocity dispersions, labeled  $\sigma_v$ , and the  $r_{200}$  values are given in Table 6.

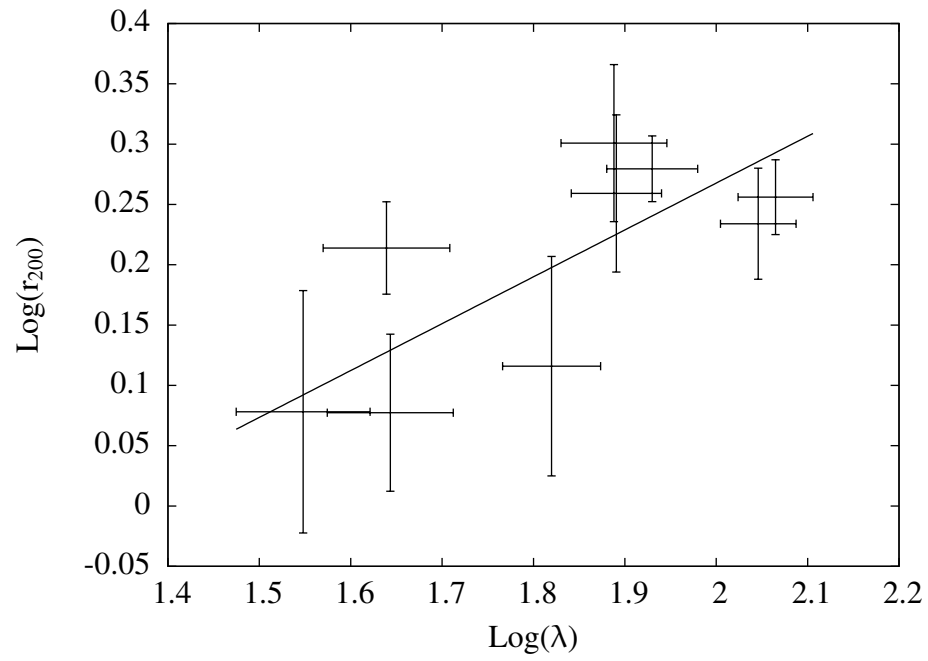


Figure 57. A linear line was fit to  $\log(\lambda)$  versus  $\log(r_{200})$  to estimate  $r_{200}$  for the rest of the sample.

## CHAPTER 4

### RESULTS

In this chapter, luminosity functions (LFs), dwarf-to-giant ratio's (DGRs), and galaxy colors are explored. All measurements are made within four cluster-centric radial bins:  $0.0 \leq r/r_{200} < 0.2$ ,  $0.2 \leq r/r_{200} < 0.4$ ,  $0.4 \leq r/r_{200} < 0.6$ , and  $0.6 \leq r/r_{200} < 1.0$ .

Additionally, LFs are also constructed in select radial bins to facilitate comparisons with previous studies.

The reddest objects expected in a galaxy cluster are those in the red-sequence. For the analyses in this chapter, all galaxies  $3\sigma$  (Sec. 3.4) redder than the red-sequence are excluded. This cut is conducted using apparent magnitudes before converting to absolute magnitudes. The same selections are used on the background control fields.

For the analysis that extends to  $r = 1.0 r_{200}$ , 13 clusters are used. The two clusters that are excluded, Abell 2147 and Abell 2199, are rich low redshift clusters. The field-of-view of Megacam does not cover their outer regions.

#### 4.1 Combined Red-Sequence

The LF for the  $u$ -band is shifted relative to the  $r$ -band as a typical cluster galaxy is red. To determine a reasonable value for the shift, a combined red-sequence for all the clusters was measured using absolute magnitudes (Fig. 58). The red-sequence was fit via a linear regression, and the uncertainty was determined using the bootstrap method with 1000 samples. The resulting fit is

$$(M_u - M_r) = (-0.099 \pm 0.002)M_r + (0.332 \pm 0.036). \quad (4.1)$$

Dwarf galaxies are defined to have  $M_r \geq -19.5$ , which is  $\approx M^* + 2$ . On the red-sequence, the  $u$ -band definition of a dwarf galaxy is  $M_u \geq -17.2$ , as determined from Eq. 4.1 using a  $r$ -band magnitude of  $-19.5$ . When comparing LFs,  $r$ -band measurements are shifted by 2.26 magnitudes.

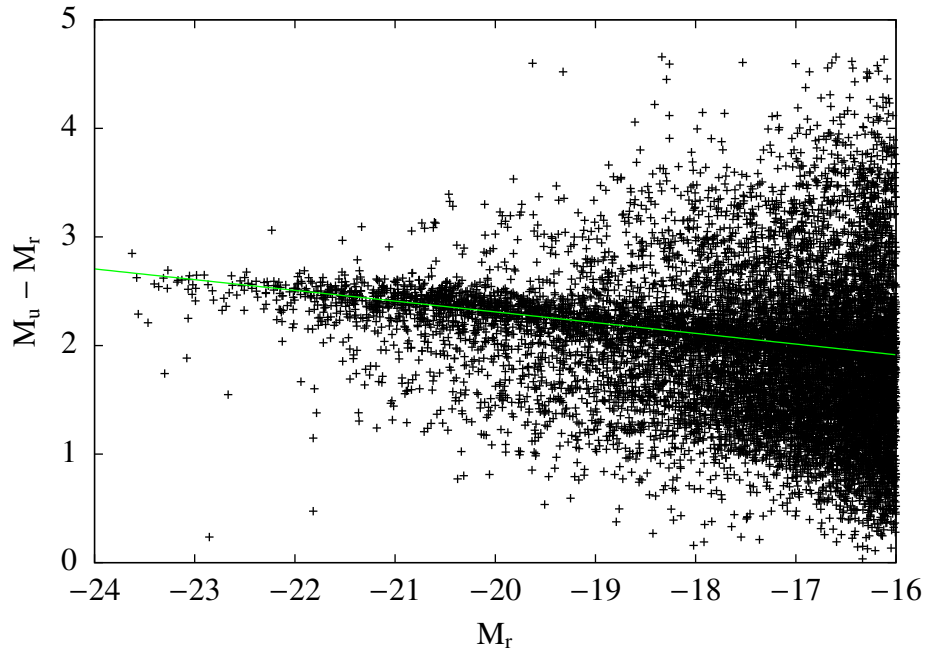


Figure 58. Color magnitude diagram measured using cluster galaxies within  $0.5 r/r_{200}$ .

## 4.2 Luminosity Functions

Since direct measurements of mass are unavailable for large surveys,  $r$ -band or infrared luminosity is used instead. There are numerous uses of LFs, as the mass distribution is often predicted in theories (Press & Schechter, 1974). Here, LFs are used to explore the galaxy population.

### 4.2.1 Measurement Uncertainties

A simulation was ran to assess the affect of the color error on galaxy position in the color-magnitude diagram. A sample of 100 galaxies brighter than  $m_r = 26$  was randomly selected within  $0.5 r/r_{200}$  of the center of A1940. Each galaxy's color and magnitude was offset by a random amount taken from a Gaussian distribution with a standard deviation equal to the uncertainty of the measurement. The result, shown in Fig. 59, shows that galaxies are just likely to scatter blueward as they are redward.

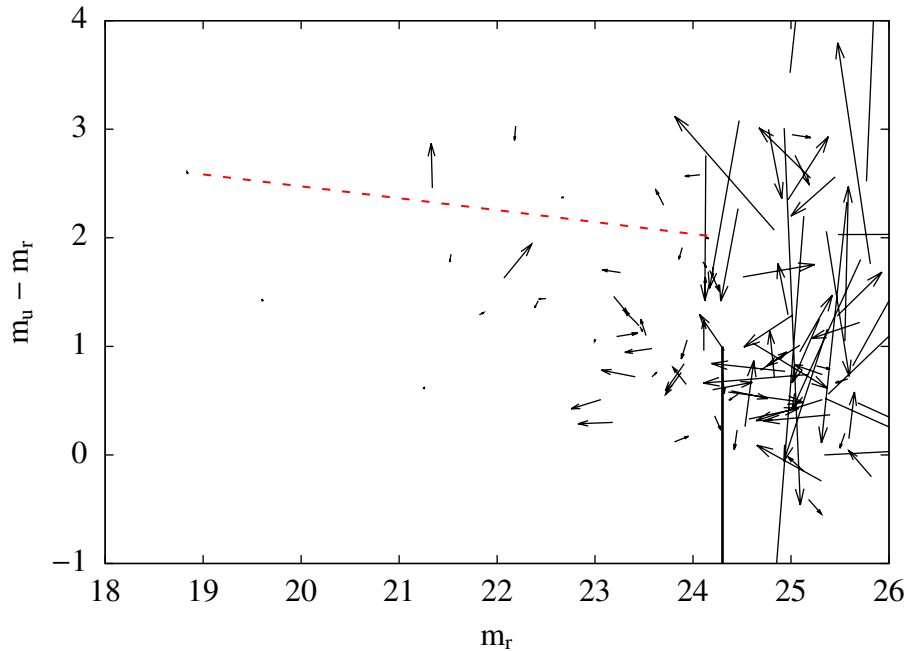


Figure 59. The tails of the arrows show the starting point of a sample of 100 galaxies within  $0.5 r/r_{200}$  of Abell 1940. The arrowhead indicates the new position after a simulated scatter in color and magnitude were applied. The thicker line in the lower right indicates the magnitude limit ( $r = 24.24$ ). The dashed red line shows the position of the red-sequence.

The procedure to statistically remove background galaxies using control fields is similar to that described in Sec. 3.4, with one exception. For lower redshift clusters  $z < 0.11$ , a background LF is constructed from all the control fields. Each control field



contributes to each magnitude bin brighter than its completeness limit. The LF is scaled by  $\left(\frac{\text{cluster area}}{\text{background area}}\right)$ , where the background area is calculated per magnitude bin, summing up the areas of all the control fields which contributed to the magnitude bin. The background corrected LF is then constructed by subtracting the scaled background LF from the cluster LF.

The uncertainty on magnitude bin  $i$  in the background corrected LF is given by

$$\sqrt{N_{ci} + 1.69 N_{bi}}, \quad (4.2)$$

where  $N_{ci}$  is the number of background subtracted cluster galaxies, and  $N_{bi}$  is the number of expected background galaxies in the cluster. The factor of 1.69 is to account for 30% field-to-field variations in the background (Barkhouse et al., 2007).

#### ***4.2.2 Combined Luminosity Function***

A combined LF is created by combining individually measured LFs. Not all of the luminosity functions reach the desired depth, and thus they are combined following the procedure outlined by Schechter (1976). The combined LF is computed, starting with a list of cluster LFs sorted by depth in descending order, as follows:

1. If the current LF is complete at the current magnitude bin, add the bin value to the combined LFs bin.
2. Else
  - (a) Integrate the combined LF up to, but not including, this bin.
  - (b) Integrate the current LF up to, but not including, this bin.

- (c) Set the bin value to the combined LF bin multiplied by the integral of the current LF divided by the integral of the combined LF.
- (d) Add the resulting bin to the combined LF.

This process is also used to estimate the number of background galaxies in the survey area used in estimating the uncertainty.

### 4.2.3 *Fitting the Luminosity Function*

The luminosity of different galaxy types have varying distributions (Thompson & Gregory, 1980). As such, a single Schechter function is not adequate to fit both the giant and dwarf populations, as can be seen in Sec. 4.2.4. As such, the measured LFs are fit using a double Schechter function.

The Schechter function (Schechter, 1976) is given by

$$N(M)dM = kN_1^* e^{k(\alpha_1+1)(M^*-M) - \exp[k(M_1^*-M)]} dM, \quad (4.3)$$

where  $k = 0.4 \ln 10$ . The measured galaxy count in a magnitude bin is the integral of the number density over the bin. A correction to the Schechter function is applied to account for this offset. As described by Schechter (1976), the correction is

$$N_i^e(M_i) = N(M_i)\Delta M + N''(M_i)\Delta M^3/24, \quad (4.4)$$

where  $\Delta M$  is the bin size.

A single Schechter function is fit to the bright galaxies using the Levenberg–Marquardt algorithm (Marquardt, 1963), holding  $\alpha_1$  fixed at  $-1$ . This fit is

made for  $-23 < M_r < -19$  in the  $r$ -band, and  $-21 < M_u < -17$  in the  $u$ -band, with the exception of the  $0.0 \leq r/r_{200} < 0.2$  region, which was fit within  $-20 < M_u < -16$ . The formation of the BCG is different from standard galaxy formation (Dressler, 1984), and can cause issues when fitting the LF. The scale factor  $N_1^*$  is constrained such that  $\int N(M)dM$  is equal to the number of galaxies within the magnitude range being fit (López-Cruz, 1997).

The resulting fit for  $M_1^*$  is used in fitting a double Schechter function, given by

$$N(M)dM = k \left( N_1^* e^{k(\alpha_1+1)(M_1^*-M) - \exp[k(M_1^*-M)]} + 2N_1^* e^{k(\alpha_2+1)(M_2^*-M) - \exp[k(M_2^*-M)]} \right) dM. \quad (4.5)$$

There are degeneracies when fitting a double Schechter function so  $M_1^*$  and  $\alpha_1$  are held fixed. Due to the relatively bright cutoff of the  $u$ -band LF used in fitting the parameters, the value of  $N_2^*$  is held fixed as the faint-slope  $\alpha$  is the primary parameter of interest.

Barkhouse et al. (2007) found that the geometric mean of  $N_2^*/N_1^*$  to be 2.12, and so the value of  $N_2^*$  is set to  $2N_1^*$ . The integral of the resulting fit is still required to match the total number of galaxies in the interval being measured.

#### ***4.2.4 r-band Composite Luminosity Functions***

The cluster stack is divided into several annuli based on  $r_{200}$  in order to compare the inner and outer region of the cluster environment. Figs. 60-63 show  $r$ -band LFs in four radial bins:  $0.0 \leq r/r_{200} < 0.2$ ,  $0.2 \leq r/r_{200} < 0.4$ ,  $0.4 \leq r/r_{200} < 0.6$ , and  $0.6 \leq r/r_{200} < 1.0$ . The parameters of the fits to the LFs are shown in Table 7. The value of  $M_2^*$  gets brighter with increasing radius. This could indicate that the dwarf population is being disrupted in the inner region of the cluster. The Schechter functions from Barkhouse et al. (2007) are also

shown with the LFs. Those functions were converted to my adopted cosmology, and a correction was applied to convert from Cousins  $R_c$  into Sloan  $r$  (Fukugita et al., 1995). The fits from Barkhouse et al. (2007) were normalized to the CFHT data by fitting the scale factor to the bright end of the LF. The bright end of the LFs show a very small number of bright galaxies, and thus they have large scatter due to small number statistics.

Table 7. Parameters derived from fitting Schechter functions in the  $r$ -band.

Radial Bin	$M_1^*$	$M_2^*$	$\alpha$
$0.0 \leq r/r_{200} < 0.2$	$-21.46 \pm 0.11$	$-16.52 \pm 0.22$	$-0.87 \pm 0.19$
$0.2 \leq r/r_{200} < 0.4$	$-21.44 \pm 0.10$	$-17.19 \pm 0.16$	$-1.24 \pm 0.08$
$0.4 \leq r/r_{200} < 0.6$	$-21.54 \pm 0.12$	$-17.67 \pm 0.19$	$-1.30 \pm 0.08$
$0.6 \leq r/r_{200} < 1.0$	$-21.44 \pm 0.12$	$-17.65 \pm 0.16$	$-1.58 \pm 0.06$

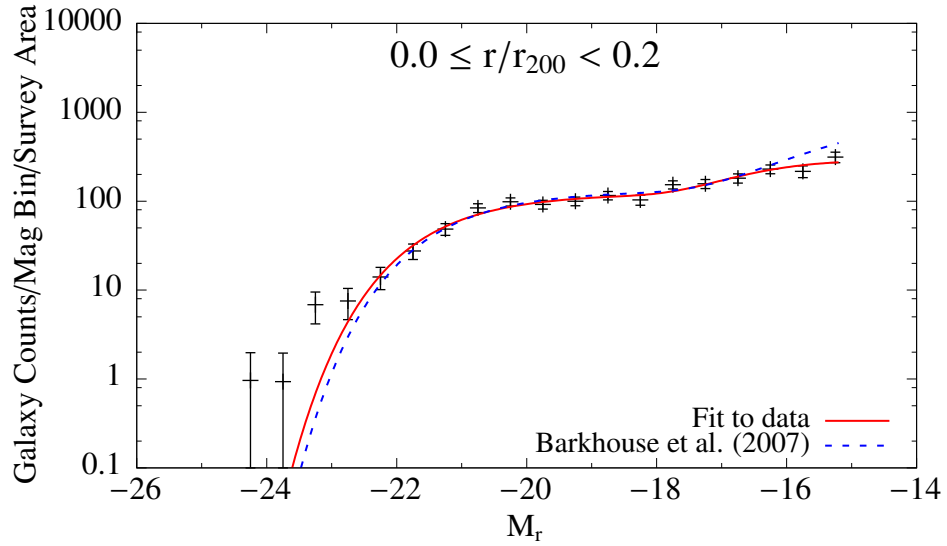


Figure 60. The  $r$ -band LF for the  $0.0 \leq r/r_{200} < 0.2$  region. The red solid line is the fit to the data, and the blue dashed line is the fit measured by Barkhouse et al. (2007).

Like previous studies, the slope of the faint-end of the LFs increase with increasing cluster-centric radii. Quantitatively, however, the LFs reported by Barkhouse et al. (2007) are steeper than this study in all radial bins. This could be due to differences in the two samples; the clusters used in Barkhouse et al. (2007) have a median redshift of

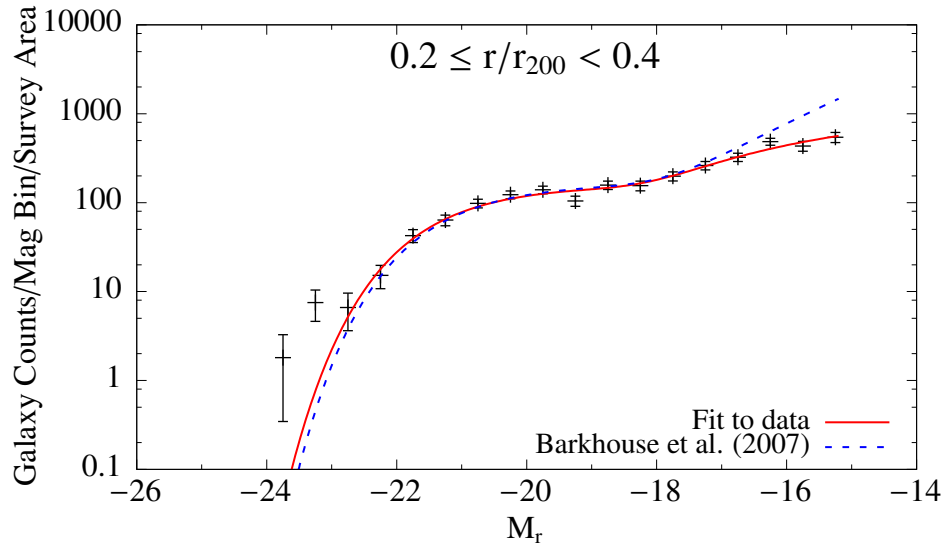


Figure 61. The  $r$ -band LF for the  $0.2 \leq r/r_{200} < 0.4$  region. The red solid line is the fit to the data, and the blue dashed line is the fit measured by Barkhouse et al. (2007).

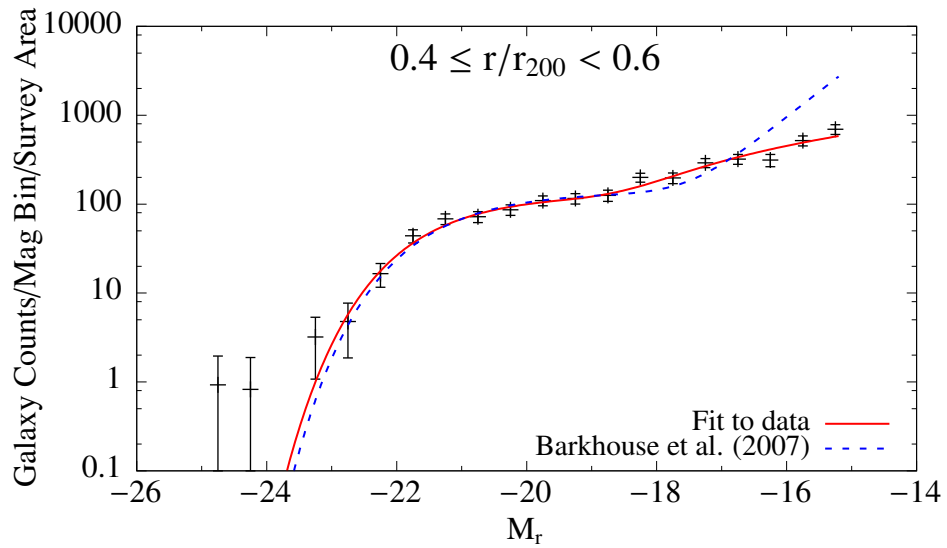


Figure 62. The  $r$ -band LF for the  $0.4 \leq r/r_{200} < 0.6$  region. The red solid line is the fit to the data, and the blue dashed line is the fit measured by Barkhouse et al. (2007).

0.06, while the clusters from this project have a median redshift of 0.13. Evolutionary effects may cause an increase in the number of dwarf galaxies. The majority galaxies in the faint-end are background galaxies, thus the faint-end is more susceptible to non-uniform backgrounds. This issue is explored in Sec. 4.2.6.

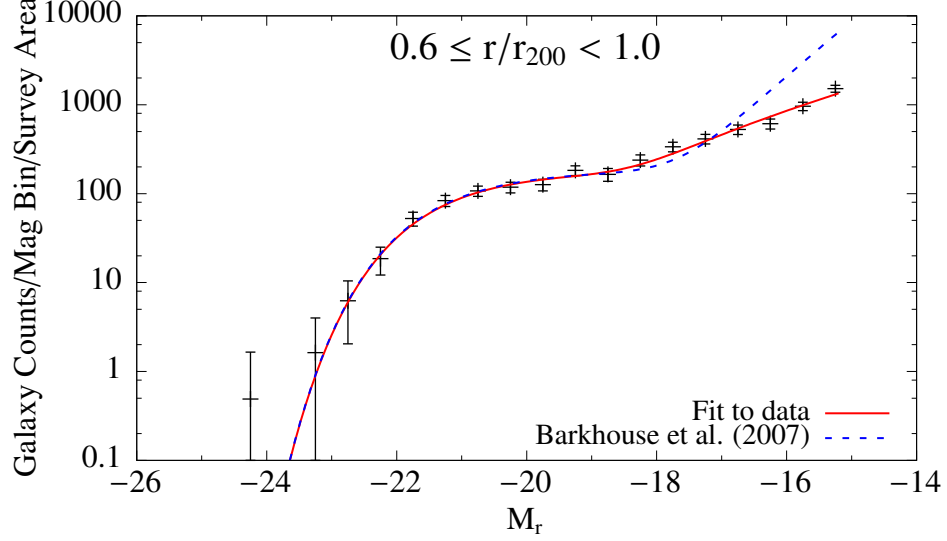


Figure 63. The  $r$ -band LF for the  $0.6 \leq r/r_{200} < 1.0$  region. The red solid line is the fit to the data, and the blue dashed line is the fit measured by Barkhouse et al. (2007).

The inner  $0.14 r/r_{200}$  region of the CFHT clusters is compared with the LF from the Coma cluster (Beijersbergen et al. 2002; Fig. 64). To fairly compare the Coma cluster with the CFHT data, the velocity dispersion from Struble & Rood (1999) was used to estimate  $r_{200}$  for the Coma cluster via Eq. 3.21. The fit to the Coma LF was adjusted to my adopted cosmology, and was normalized to match the bright-end of the CFHT LF.

For the full region of the sample,  $0 \leq r/r_{200} < 1$ , comparisons are made with both Beijersbergen et al. (2002) and Popesso et al. (2006). The double LF used by Popesso et al. (2006) differs from this work. Instead of setting the faint-end LF to twice the bright-end, they use

$$\phi(L) = \phi^* \left[ \left( \frac{L}{L_b^*} \right)^{\alpha_b} \exp\left(\frac{-L}{L_b^*}\right) + \left( \frac{L_b^*}{L_f^*} \right) \left( \frac{L}{L_f^*} \right)^{\alpha_f} \exp\left(\frac{-L}{L_f^*}\right) \right]. \quad (4.6)$$

Instead of weighting the faint-end Schechter function as twice that of the first Schechter

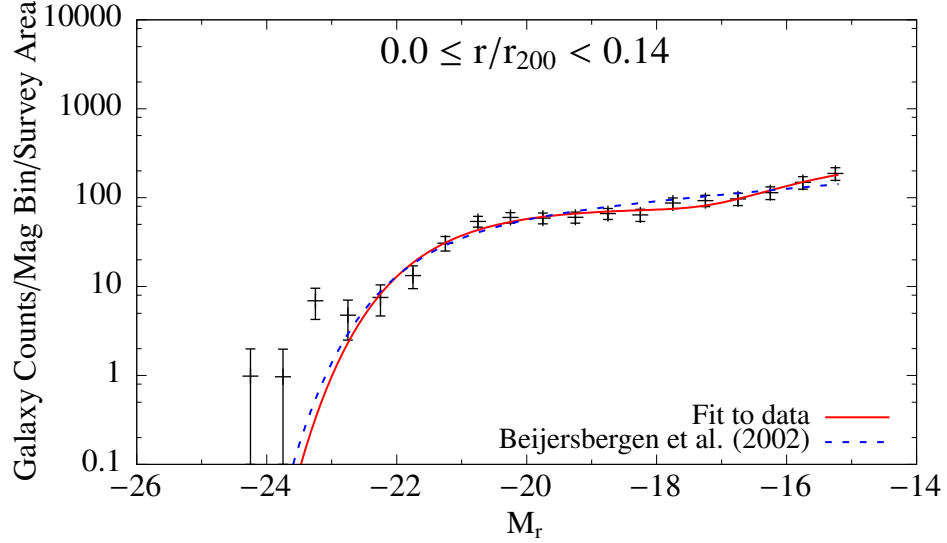


Figure 64. The  $r$ -band LF for the  $0.0 \leq r/r_{200} < 0.14$  region. The red solid line is the fit to the data, and the green dashed line is the fit measured by Beijersbergen et al. (2002).

function, it is weighted by  $L_b^*/L_f^*$ . Using  $M = -2.5 \log(L)$ , the normalization becomes

$$\exp(k(M_f^* - M_b^*)). \quad (4.7)$$

The fits from Beijersbergen et al. (2002) and Popesso et al. (2006) are compared to the CFHT data in Fig. 65. The comparison with Beijersbergen et al. clearly shows that a single Schechter function is an inadequate match to the data. The faint-end slope from Popesso et al. LF fit rises much sooner and steeper than the CFHT data. Their resulting slopes could be too steep due to underestimating the number of background galaxies.

#### 4.2.5 $u$ -band Composite Luminosity Functions

There are not many published  $u$ -band LFs to compare with my LFs. The only data at a similar depth is from Beijersbergen et al. (2002). Those comparisons are shown in Figs. 66 and 67. The  $u$ -band data for Coma LF was observed using an RGO filter. I am unaware

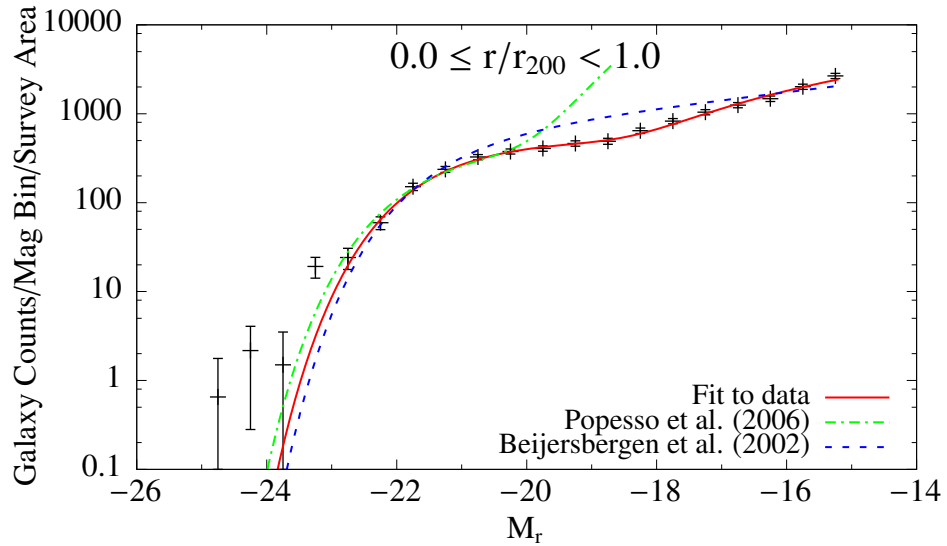


Figure 65. The  $r$ -band LF for the  $0.0 \leq r/r_{200} < 1.0$  region. The red solid line is the fit to the data, and the green dashed line is the fit measured by Popesso et al. (2006), and the blue dot-dashed line is from Beijersbergen et al. (2002).

of any known measurements to convert RGO  $U$ -band magnitudes into Sloan  $u$  magnitudes. To compare the two LFs,  $M^*$  from Beijersbergen et al. (2002) was adjusted to match the CFHT LFs. This would cause issues if comparisons were being made to the bright end, however, we are only interested in the faint-end, so this should not cause any significant problems. The CFHT  $u$ -band LF for the  $0.0 \leq r/r_{200} < 1.0$  region shows reasonable agreement with Beijersbergen et al. (2002), though a single Schechter function does not fully describe the data.

Hammer et al. (2012) constructed deep luminosity functions in the near ultraviolet (NUV) and far-ultraviolet (FUV) from the Galaxy Evolution Explorer (*GALAX*; an ultraviolet space telescope). The wavelengths sampled by the NUV filter is near the CFHT  $u$ -band filter (Fig. 68), and so a comparison is reasonable. The *GALAX* data is taken from an aperture with a radius of 0.6 deg, centered 0.9 deg away from the center of the cluster. This is near a known subcluster of Coma. The CFHT data within an annuli of



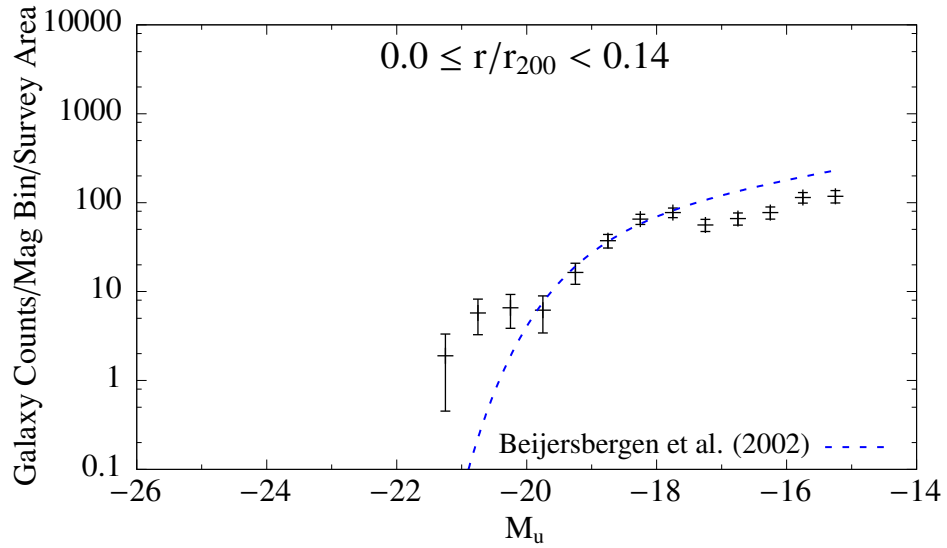


Figure 66. The  $u$ -band LF for the  $0.0 \leq r/r_{200} < 0.14$  region. The blue dashed line is the fit measured by Beijersbergen et al. (2002).

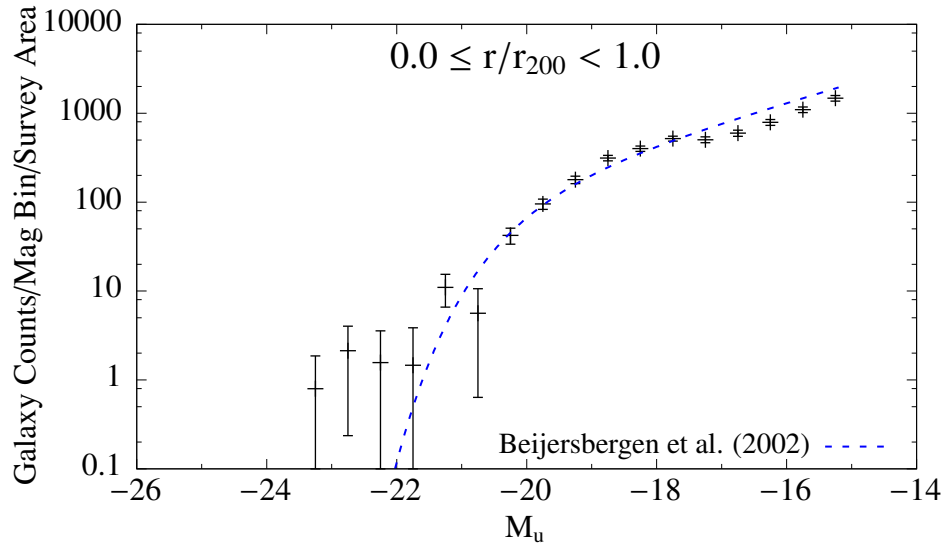


Figure 67. The  $u$ -band LF for the  $0.0 \leq r/r_{200} < 1.0$  region. The blue dashed line is the fit measured by Beijersbergen et al. (2002).

$0.25 \leq r/r_{200} < 1.0$  is compared with the Coma LF in Fig.69. The Coma LF also had  $M^*$  adjusted to match the CFHT data. Like the RGO  $U$ -band data, the *GALAX* NUV LF matches the CFHT data reasonably well.

The LFs for the four radial bins are shown in Figs. 70-73. The results of the LF

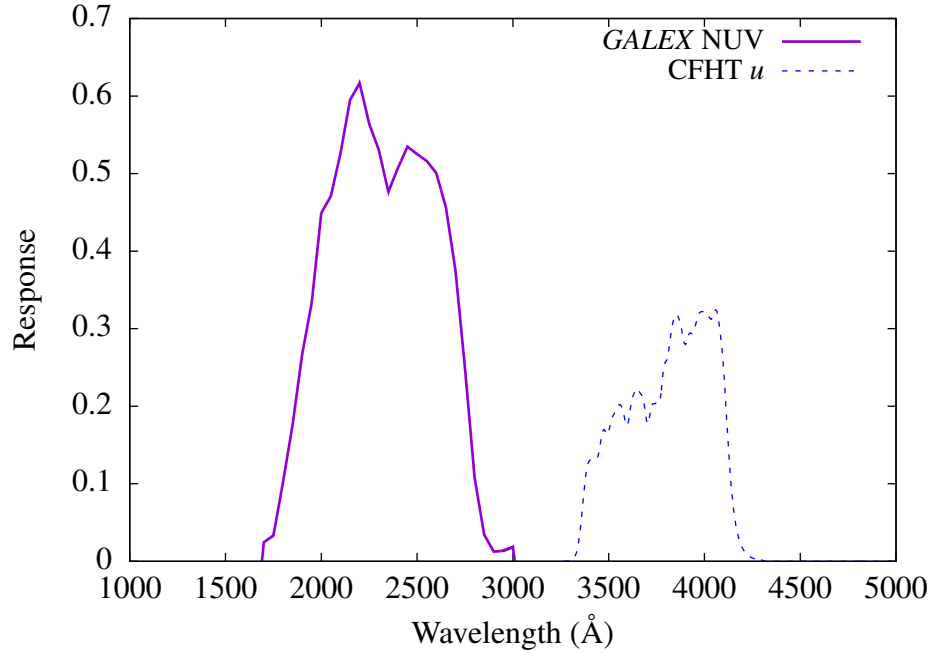


Figure 68. The response of the *GALAX* NUV filter (left) and the CFHT *u* filter (right).

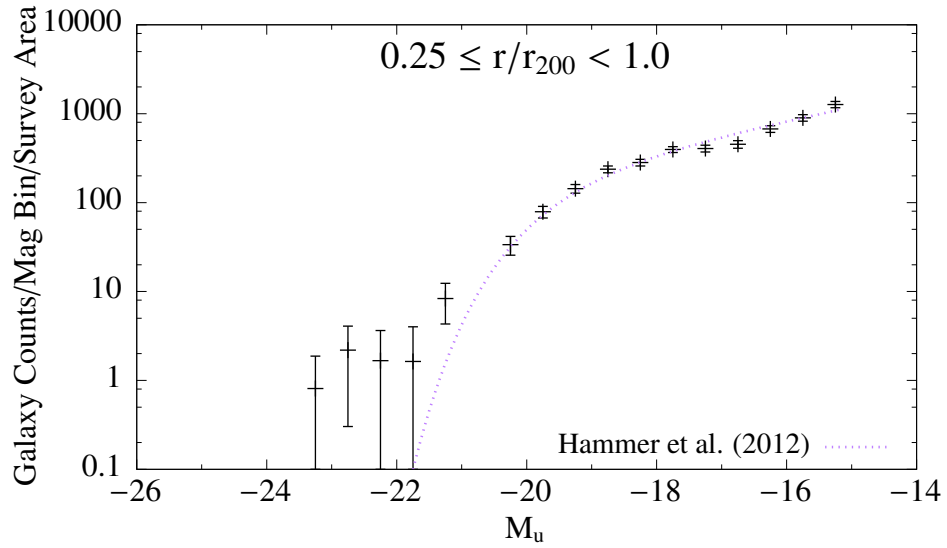


Figure 69. The *u*-band LF for the  $0.25 \leq r/r_{200} < 1.0$  region. The purple dotted line is the fit measured by Hammer et al. (2012).

fitting are shown in Table 8. The results from the fits of the second Schechter function are not well constrained, and a deeper LF is required to make an adequate measurement of the parameters. The decrease in  $M_1^*$  and  $M_2^*$  with increasing cluster-centric radius could be

caused by star formation increasing the  $u$ -band luminosity of galaxies in the outer regions.

The  $r$ -band double Schechter function fits are compared to the  $u$ -band using a 2.26 magnitude shift, as explained in Sec. 4.1.

Table 8. Parameters derived from fitting Schechter functions in the  $u$ -band.

Radial Bin	$M_1^*$	$M_2^*$	$\alpha$
$0.0 \leq r/r_{200} < 0.2$	$-18.92 \pm 0.11$	$-14.80 \pm 1.43$	$-0.95 \pm 4.12$
$0.2 \leq r/r_{200} < 0.4$	$-18.94 \pm 0.10$	$-15.13 \pm 0.24$	$-1.89 \pm 1.80$
$0.4 \leq r/r_{200} < 0.6$	$-19.10 \pm 0.11$	$-15.57 \pm 0.17$	$-1.92 \pm 0.73$
$0.6 \leq r/r_{200} < 1.0$	$-19.13 \pm 0.12$	$-16.12 \pm 0.18$	$-1.71 \pm 0.27$

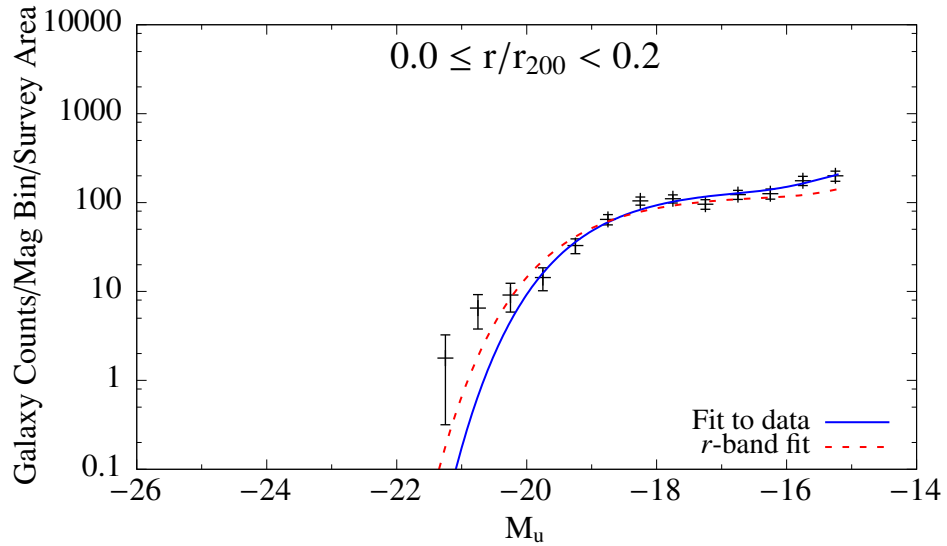


Figure 70. The  $u$ -band LF for the  $0.0 \leq r/r_{200} < 0.2$  region. The blue solid line is the fit to the data. The red dashed line is the fit to the  $r$ -band data shifted to the right by 2.26 magnitudes.

The inner regions shows a marginal increase in the faint-end slope of the  $u$ -band LF relative to the  $r$ -band. The outermost region shows the largest increase in the  $u$ -band faint-end slope. This is similar to the results from Beijersbergen et al. (2002), but with higher precision. One explanation for this effect is enhanced star formation in the outer region of the cluster sample. Faint dwarf galaxies become brighter in the  $u$ -band, but are

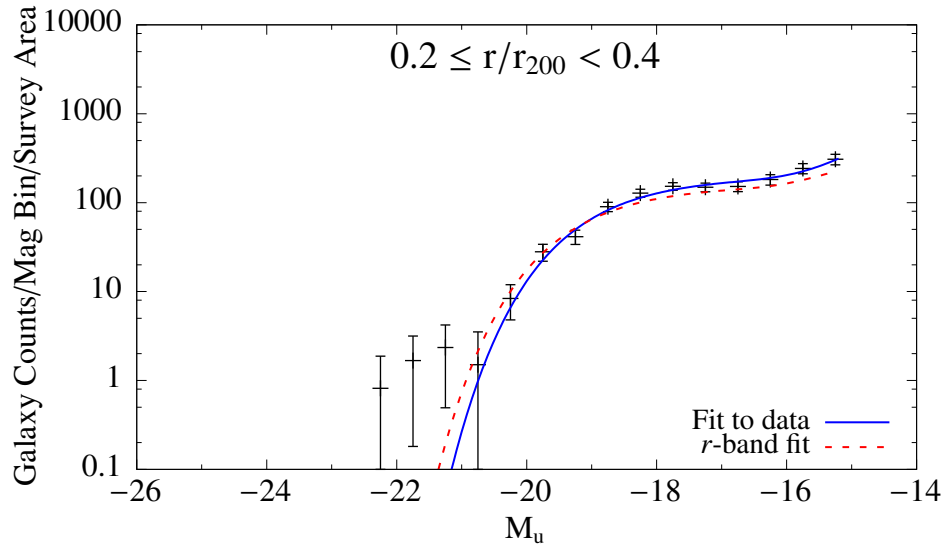


Figure 71. The  $u$ -band LF for the  $0.2 \leq r/r_{200} < 0.4$  region. The blue solid line is the fit to the data. The red dashed line is the fit to the  $r$ -band data shifted to the right by 2.26 magnitudes.

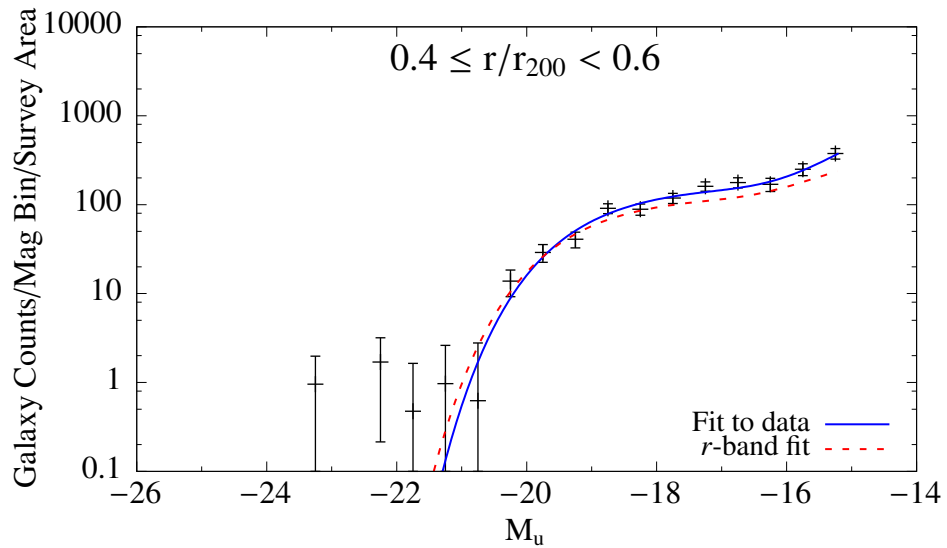


Figure 72. The  $u$ -band LF for the  $0.4 \leq r/r_{200} < 0.6$  region. The blue solid line is the fit to the data. The red dashed line is the fit to the  $r$ -band data shifted to the right by 2.26 magnitudes.

relatively unaffected in the  $r$ -band, causing an increase in the faint-end slope of the  $u$ -band LF.

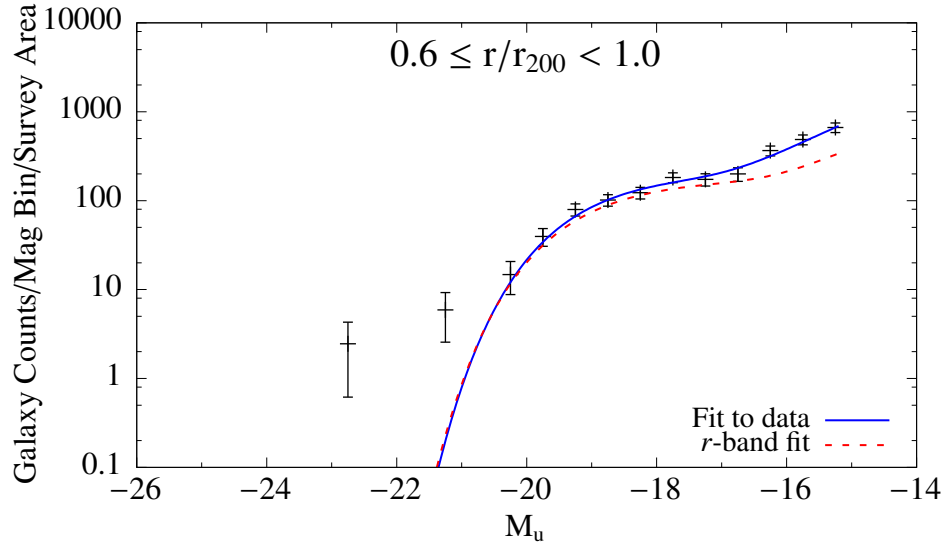


Figure 73. The  $u$ -band LF for the  $0.6 \leq r/r_{200} < 1.0$  region. The blue solid line is the fit to the data. The red dashed line is the fit to the  $r$ -band data shifted to the right by 2.26 magnitudes.

#### 4.2.6 Possible Biases

One explanation for the discrepancy between the CFHT LFs and Barkhouse et al. (2007) is the difference in background subtraction between the two studies. Barkhouse et al. (2007) use control fields away from individual clusters, while I use the region surrounding each cluster. If the region is selected too close to the cluster, the background could be systematically too large. To estimate this effect, catalogs taken from the CFHT Legacy Survey Deep Fields were used to estimate the background (Figs. 74 and 75). This method, however, resulted in even flatter slopes. The Deep Field catalogs were generated using `Source Extractor`. Systematic differences in the detection and classification of galaxies could affect the resulting slope. As can be seen in the figures, only the faint-end is heavily affected due to the large number of faint background galaxies. For the  $0.0 \leq r/r_{200} < 1.0$  region, the number of background galaxies surpasses the number of cluster galaxies at  $\approx -18.75$  in the  $r$ -band, and  $\approx -17.25$  in the  $u$ -band. Systematic effects are minimized

when utilizing the same methodology for detecting cluster and background galaxies, and so the original backgrounds are used for the remaining analysis.

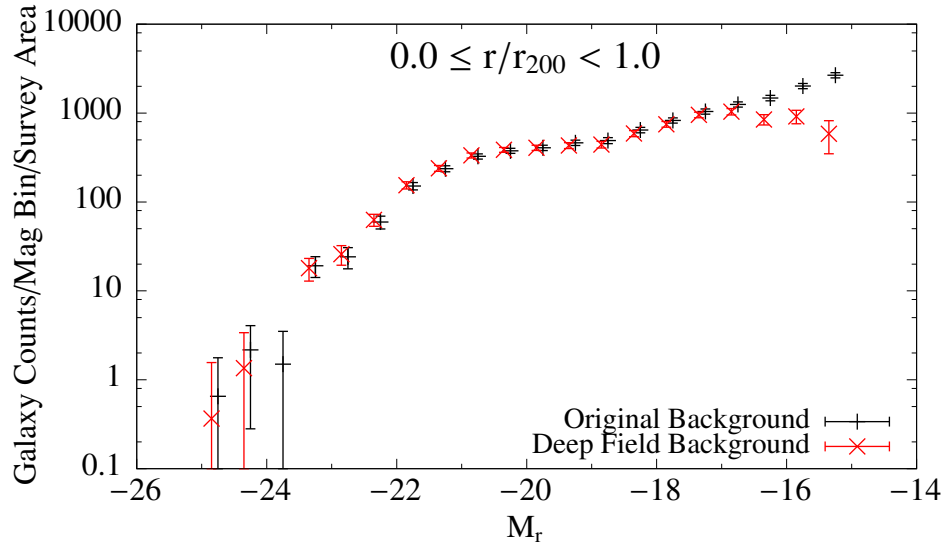


Figure 74. The  $r$ -band LF for the  $0.0 \leq r/r_{200} < 1.0$  region using original background (black dashes) and using background fields from the CFHTLS Deep Fields (red X's). The Deep Field LF was offset by 0.1 magnitudes for visualization purposes.

The differences between the two methodologies is not as extreme in the  $u$ -band compared to the  $r$ -band. The number of background galaxies per magnitude bin in the  $u$ -band is approximately equal to the number in the  $M_r - 1.5$  magnitude bin. Therefore the differences in background subtraction is noticeable about 1.5 magnitudes brighter in the  $r$ -band than in the  $u$ -band. Additionally, the direct comparisons of the faint-end  $u$ -band LFs are in the  $-19.5 < M_r < -17$  range, and so the last bins of the  $r$ -band LF are not directly comparable to the  $u$ -band CFHT data.

Another possible issue is the Eddington bias (Eddington, 1913). This effect is due to the uncertainty in the magnitude measurements. The bias is easily understood when considering two adjacent bins in a histogram. If one of the bins contains more galaxies,

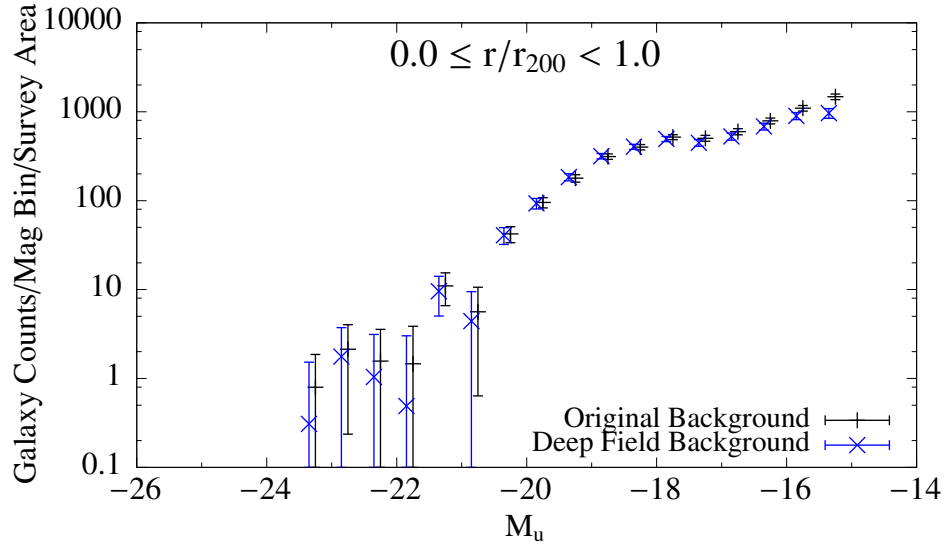


Figure 75. The  $u$ -band luminosity function for the  $0.0 \leq r/r_{200} < 1.0$  region using original background (black dashes) and using background fields from the CFHTLS Deep Fields (blue X's). The Deep Field LF was offset by 0.1 magnitudes for visualization purposes.

the number of galaxies that will scatter out of the larger bin will be greater than the number that scatter into the larger bin. This has the effect of smoothing the overall distribution. This bias was explored by simulating a galaxy population. First, the  $u$ -band LF in the  $0.0 \leq r/r_{200} < 0.5$  was fit using the procedure from Sec. 4.2.3. Additionally, the uncertainty in the  $u$ -band magnitude was binned as a function of magnitude, and the median uncertainties in each bin were fit using a cubic function (Fig. 76). The procedure followed was similar to that of Sec. 3.2. The faint-end slope of the second LF was increased by setting  $\alpha = -3$  in order to exacerbate the bias in the faintest bin. The resulting double Schechter function was used to generate 10,000 galaxies from the magnitude range  $-26 \leq M_u < -14.5$ . An error was calculated for each simulated galaxy by drawing a random number from a normal distribution with a mean of zero and a standard deviation determined by the cubic fit to the measured uncertainty in  $M_u$ . The

cubic fit to the uncertainty goes negative at the bright-end as bright galaxies have an error that is below the precision of PPP. In this case, the simulated galaxy was assumed to have no associated uncertainty in magnitude. An LF was made from the simulated galaxies with and without simulated scatter. As can be seen in Fig. 77, the relative change in counts due to the Eddington bias is small.

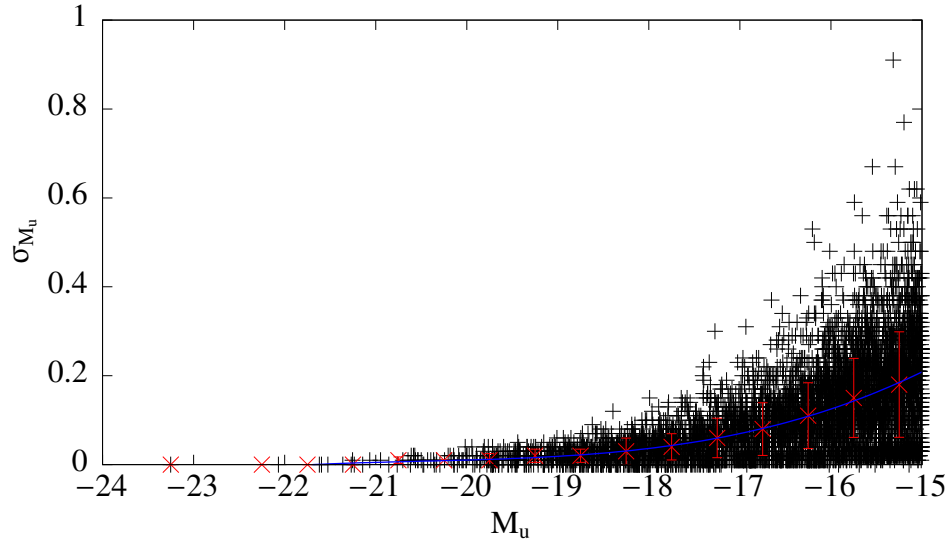


Figure 76. The uncertainty in magnitude for galaxies within  $0.5 r/r_{200}$ . The data was binned, and the median value for each bin is plotted using red markers. The uncertainty shown is the MAD value for the bin. A cubic fit to the points is shown with a blue line.

The last possible bias explored is due to projection effects. Assuming the cluster is spherically symmetric, the outer region of the cluster will be projected in front and behind the inner region of the cluster (Beijersbergen et al., 2002; Barkhouse et al., 2007). As shown in Fig. 78, galaxies projected in front and behind the center of the cluster, regions B1 and B2, are counted in the LF of the inner region. To determine the true inner region LF, the projected galaxies must be subtracted from the projected LF. This can be accomplished using the LF measured from the projected outskirts of the cluster, region C.



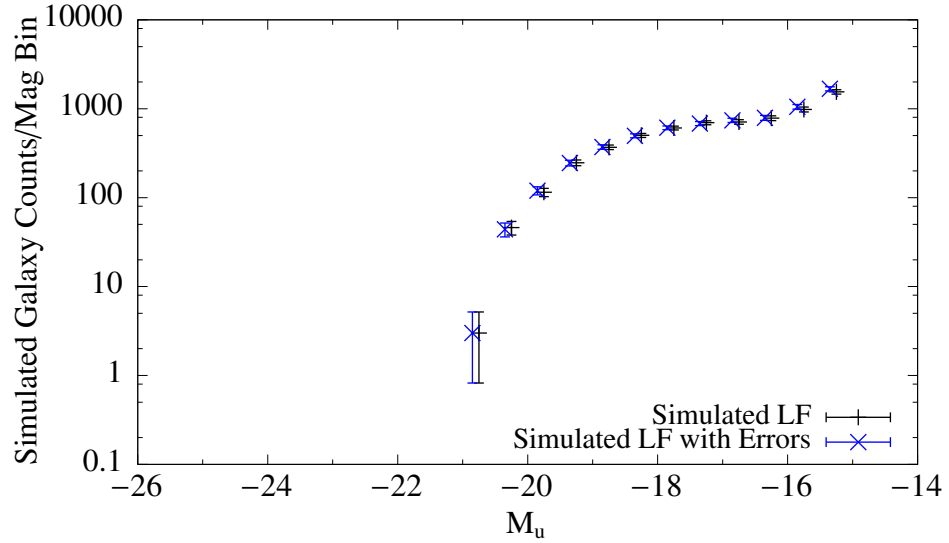


Figure 77. The  $u$ -band LF from the simulated galaxy cluster is shown as black dashed markers, and the LF after the simulated uncertainty was applied is shown as red X's. The simulated LF with errors was offset by 0.1 magnitudes for visualization purposes.

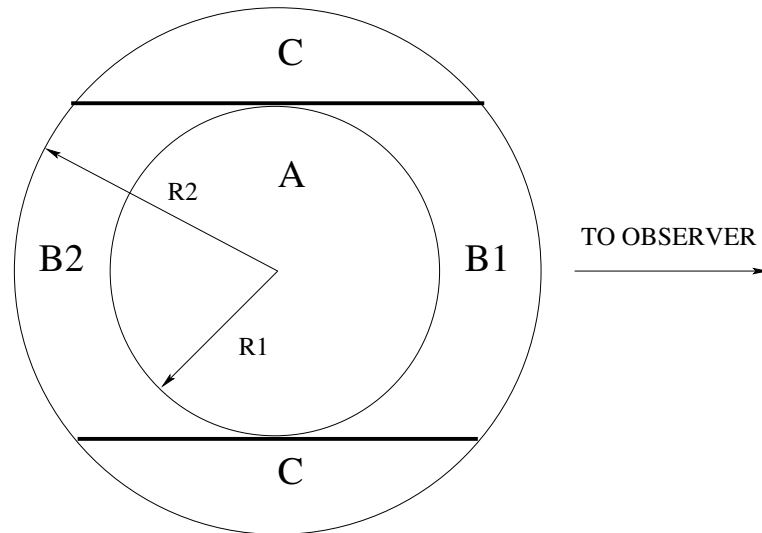


Figure 78. Galaxies in the volume B1 and B2 are projected onto volume A. Reproduced from Barkhouse et al. (2007).

The outer LF first needs to be normalized by the total volume of B1 and B2. The normalization factor is given by

$$\frac{V(B1) + V(B2)}{V(C)}, \quad (4.8)$$

where  $V(X)$  is the volume of region  $X$ . Calculating  $V(B1) + V(B2)$  directly is difficult, and so  $V(B1) + V(B2) + V(A)$  is computed first. This allows for easy computation of  $V(C)$  given that  $V(A) + V(B1) + V(B2) + V(C) = \frac{4}{3}\pi R_2^3$  and  $V(A) = \frac{4}{3}\pi R_1^3$ , where  $R_1$  and  $R_2$  are the radii of the inner and outer regions, respectively. The volume of  $A + B1 + B2$  can be described by a cylinder of radius  $R_1$  with two caps (Fig. 79). The problem of determining

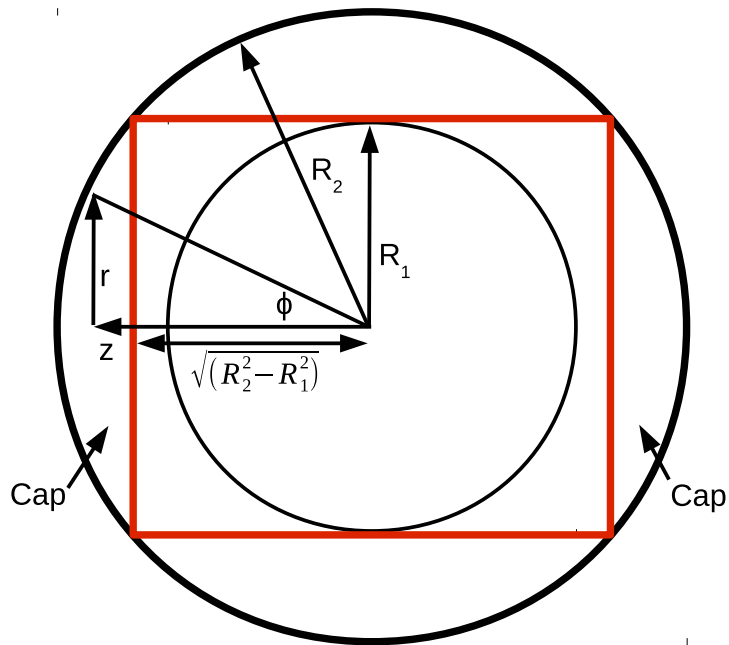


Figure 79. Schematic cross section of the Napkin Ring Problem. The red rectangle represents a cylinder of radius  $R_1$ . The  $z$  coordinate is along the sight of the observer. The caps begin at a distance of  $\sqrt{R_2^2 - R_1^2}$  along the  $z$  axis. The angle between the  $z$  axis and the edge of the outer sphere is  $\phi$ .

the volume of region  $C$  is known as the “Napkin Ring Problem,” as region  $C$  looks like a napkin ring. The volume of a cap can be calculated by

$$V(\text{cap}) = \pi \int_{\sqrt{R_2^2 - R_1^2}}^{R_2} r^2 dz. \quad (4.9)$$

Using the change of variables

$$\begin{aligned}
 r &= R_2 \sin \phi, \\
 z &= R_2 \cos \phi, \\
 dz &= -R_2 \sin(\phi) d\phi,
 \end{aligned}
 \tag{4.10}$$

Eq. 4.9 becomes

$$V(\text{cap}) = \pi \int_{\phi_i}^0 R_2^3 \sin^3(\phi) d\phi,
 \tag{4.11}$$

where  $\phi_i = \frac{\sqrt{R_2^2 - R_1^2}}{R_2}$ . Performing the integration yields

$$V(\text{cap}) = \frac{2}{3} \pi R_2^3 - \frac{\pi}{3} (R_1^2 + 2 R_2^2) \sqrt{R_2^2 - R_1^2}.
 \tag{4.12}$$

The volume of the regions A, B1, and B2 can now be computed using

$$V(A) + V(B1) + V(B2) = 2V(\text{cap}) + \pi R_1^2 \left( 2 \sqrt{R_2^2 - R_1^2} \right).
 \tag{4.13}$$

A normalization factor is calculated by summing the volumes of B1 and B2 of all the clusters, and dividing by the sum of volume C. The resulting deprojected LFs are shown in Figs. 80 and 81. In both cases, the resulting LFs are noticeably shallower than the original. In order to compare the two deprojected LFs, each LF was fit with a single Schechter function, as neither LF shows an upturn in the faint-end slope. The two fits are shown in Fig 82. These two functions are consistent with each other, which indicates no star formation in the central region of the cluster.

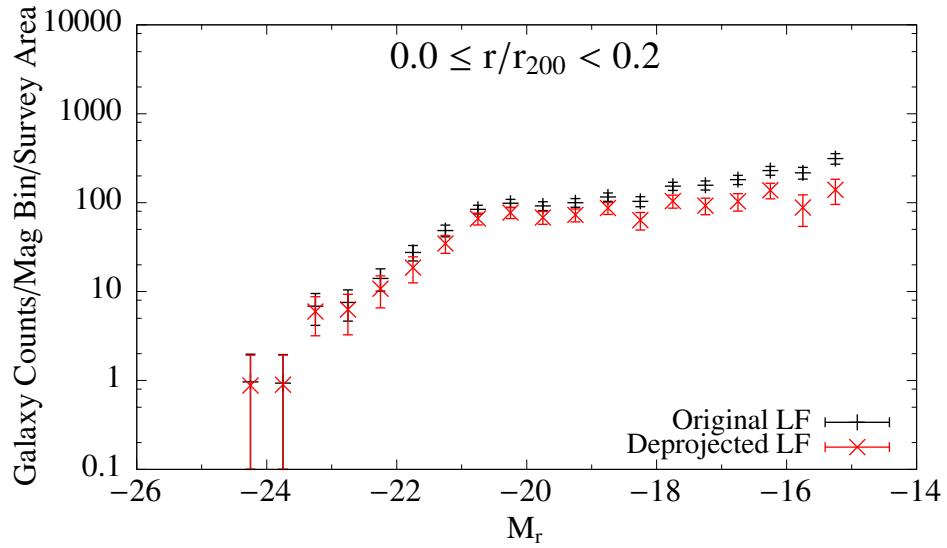


Figure 80. The original and deprojected  $r$ -band LFs for the  $0.0 \leq r/r_{200} < 0.2$  region. The black dashed markers are the original, projected LF, and the deprojected LF is shown as red X's.

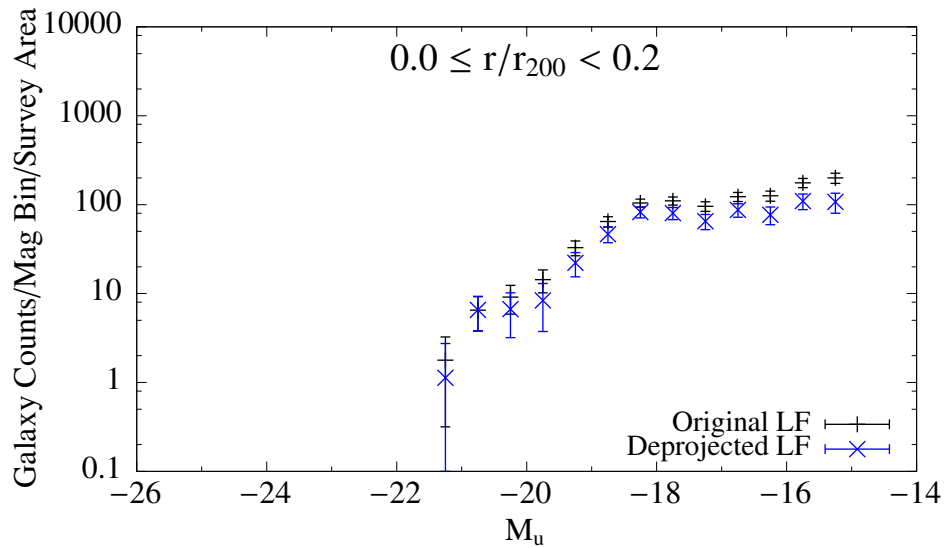


Figure 81. The original and deprojected  $u$ -band LFs for the  $0.0 \leq r/r_{200} < 0.2$  region. The black dashed markers are the original, projected LF, and the deprojected LF is shown as blue X's.

### 4.3 Dwarf-to-Giant Ratio

The DGR is another way to look for evidence of star formation in a non-parametric way.

For the  $r$ -band, giant galaxies are defined to have  $M_r < -19.5$ , and dwarfs have

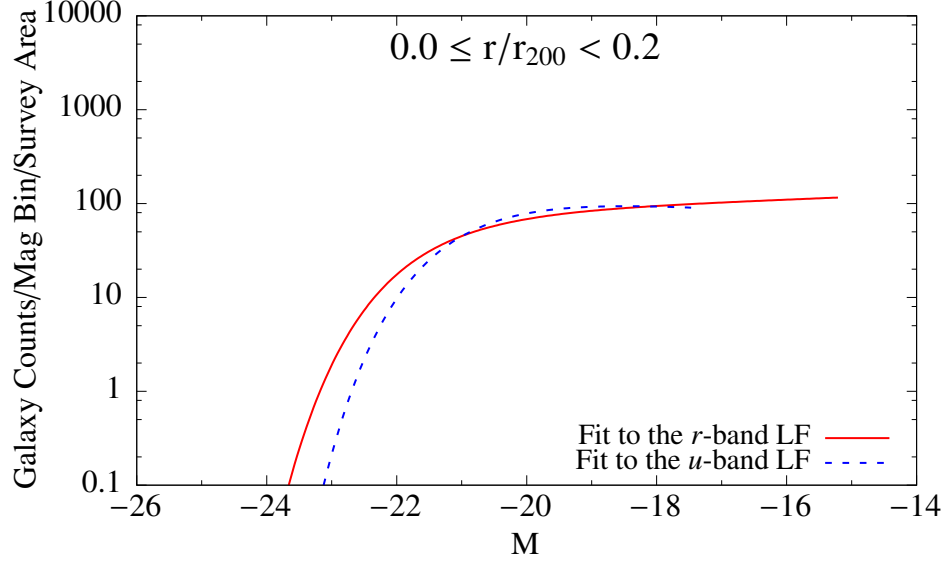


Figure 82. The Schechter fits to the deprojected LFs in the  $0.0 \leq r/r_{200} < 0.2$  region. The solid red line is the fit to the  $r$ -band and the dashed blue line shows the fit to the  $u$ -band. The  $u$ -band is shifted by 2.26 magnitudes to the left to facilitate the comparison.

$-19.5 \leq M_r < -17.5$ . Using the results from Sec. 4.1, giants in the  $u$ -band have  $M_u < -17.24$  and dwarfs have  $-17.24 \leq M_u < -15.24$ . Since Abell 2688 is not deep enough in the  $u$ -band, it has been excluded from these measurements. The Abell 2688 control field, however, was still used in the estimation of the background count for low redshift clusters. To be consistent with previous measurements, the uncertainty in  $N$  (the galaxy count) is given by  $\sqrt{N}$ . When subtracting the background counts from the cluster counts, the errors are added in quadrature

$$\sigma = \sqrt{N_{uc} + N_{bi}}, \quad (4.14)$$

where  $N_{uc}$  is the number of uncorrected cluster counts, and  $N_b$  is the number of expected background counts. The uncertainty in the DGR is then

$$\sigma_{DGR} = DGR \sqrt{\left(\frac{\sigma_G}{N_G}\right)^2 + \left(\frac{\sigma_D}{N_D}\right)^2}, \quad (4.15)$$

where  $N_G$  and  $N_D$  denote the number of giant and dwarf galaxies, respectively.

The DGR as a function of  $r/r_{200}$  is shown in Fig 83. As expected from the LFs, the  $u$ -band DGR is slightly larger than the  $r$ -band in the inner region, and they both increase with increasing cluster-centric radius. In the outer region, the difference between the  $u$ - and  $r$ -band DGR is the greatest, consistent with a population of star forming galaxies.

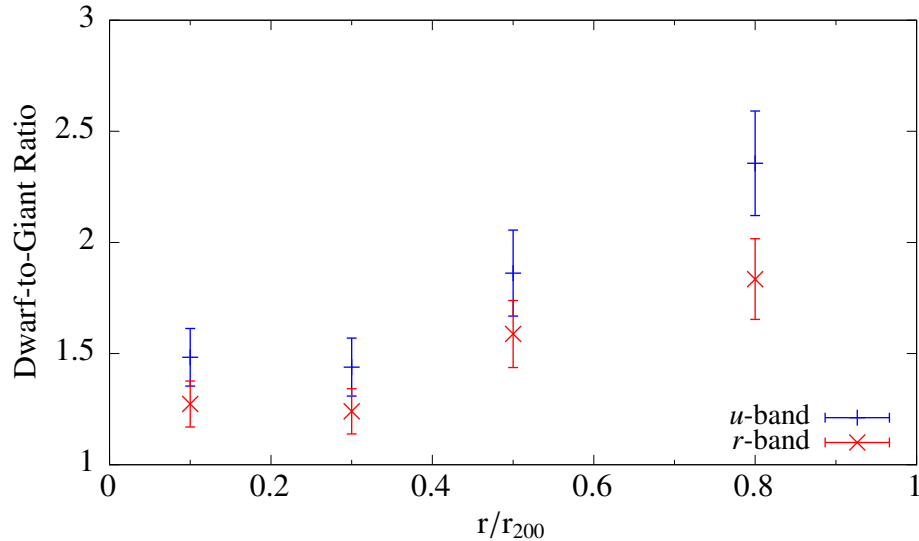


Figure 83. The  $r$ -band (red dashes) and  $u$ -band (blue X's) dwarf-to-giant ratios in four radial bins.

One factor that may reduce the DGR in the  $u$ -band relative to the  $r$ -band is star formation in brighter dwarf galaxies. A galaxy classified as a dwarf in the  $r$ -band could be classified as a giant in the  $u$ -band. This effect is investigated in Fig. 84. The inner region of the cluster sample shows a similar number of giants detected in both bands, while the

outer region shows 25% more giants detected in the  $u$ -band. When comparing dwarfs, the  $u$ -band has 60% more dwarfs than the  $r$ -band (Fig. 85).

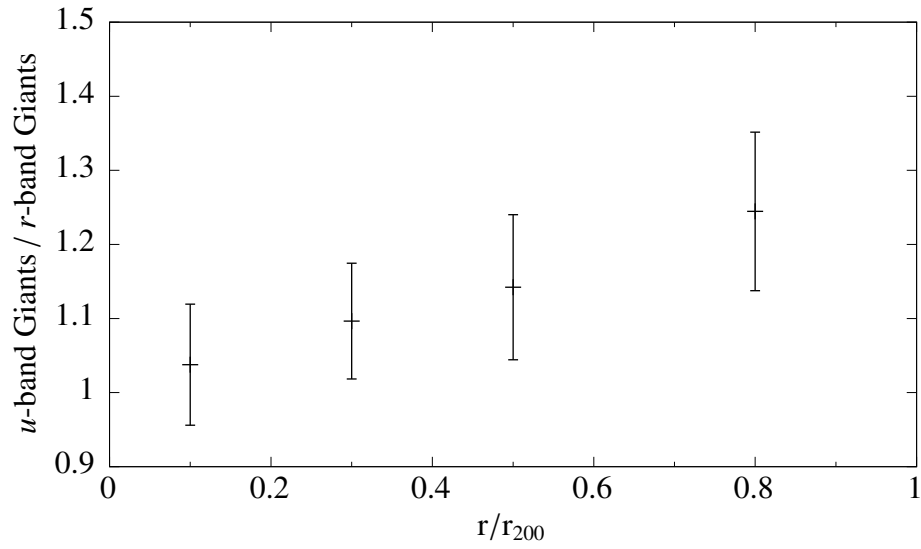


Figure 84. The ratio of  $u$ -band giants to  $r$ -band giants.

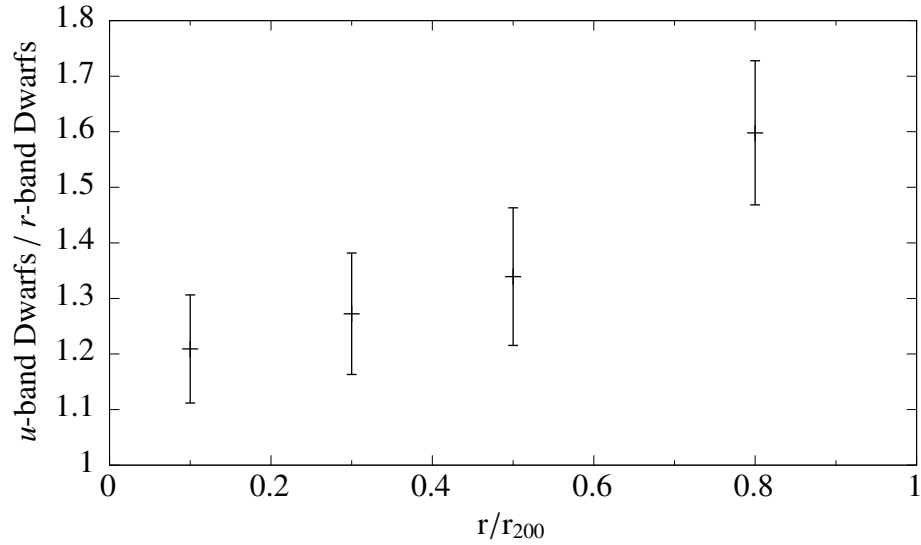


Figure 85. The ratio of  $u$ -band dwarfs to  $r$ -band dwarfs.

#### 4.4 Galaxy Color

Galaxy color can be used to discriminate between starforming and non-starforming galaxies (Kennicutt, 1998). In order to study the galaxy population, histograms of  $u - r$  color are constructed for the four radial bins used previously. The errors in each bin of the histogram are computed using  $\sqrt{N_{ui} + N_{bi}}$ , where  $N_{ui}$  and  $N_{bi}$  are the uncorrected cluster counts and the expected number of background counts in bin  $i$ , respectively. Dwarf galaxies are selected to be within  $-19.5 \leq M_r < -17$ . The results are shown in Figs. 86-89.

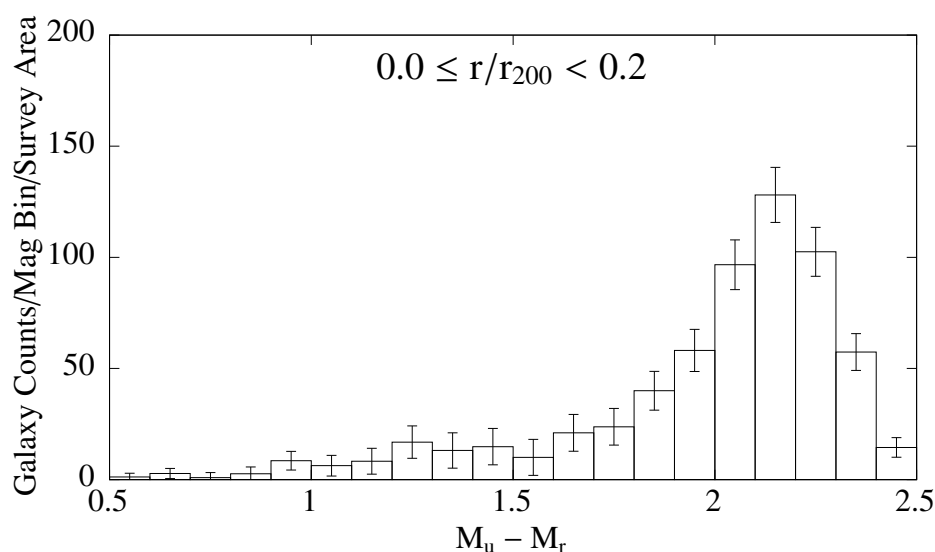


Figure 86. Histogram of dwarf galaxy color within  $-19.5 \leq M_r < -17$  for the  $0 \leq r/r_{200} < 0.2$  region.

Comparing the four figures, the relative size of the blue galaxy population grows relative to the red population with increasing cluster-centric radii. This coincides with the relative increase of the  $u$ -band DGR with respect to the  $r$ -band DGR. The color of giant galaxies  $-26 \leq M_r < -19.5$  for the  $0.6 \leq r/r_{200} < 1.0$  region does not show a large population of blue galaxies (Fig. 90).



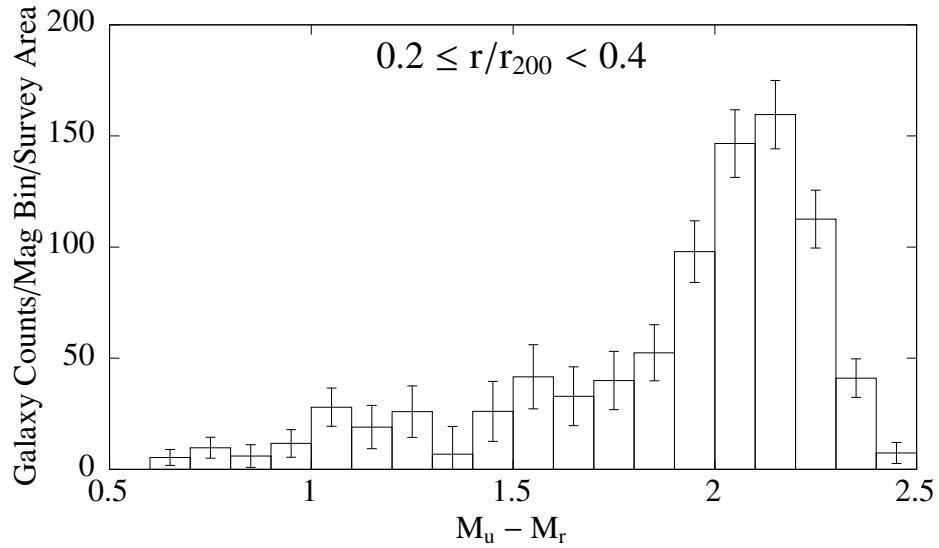


Figure 87. Histogram of dwarf galaxy color within  $-19.5 \leq M_r < -17$  for the  $0.2 \leq r/r_{200} < 0.4$  region.

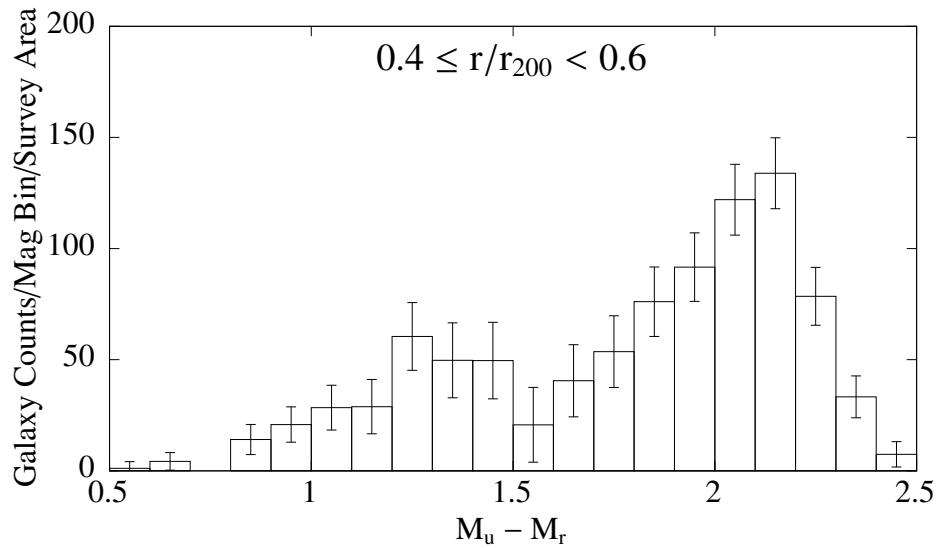


Figure 88. Histogram of dwarf galaxy color within  $-19.5 \leq M_r < -17$  for the  $0.4 \leq r/r_{200} < 0.6$  region.

The color distribution is bimodal with a population of red and blue galaxies that can be separated using a color cut. Examination of the color histograms suggest separating the two populations using a color of  $u - r = 1.6$ . The bins are summed on either side of the color cut to measure the number of blue and red galaxies, and the fraction of

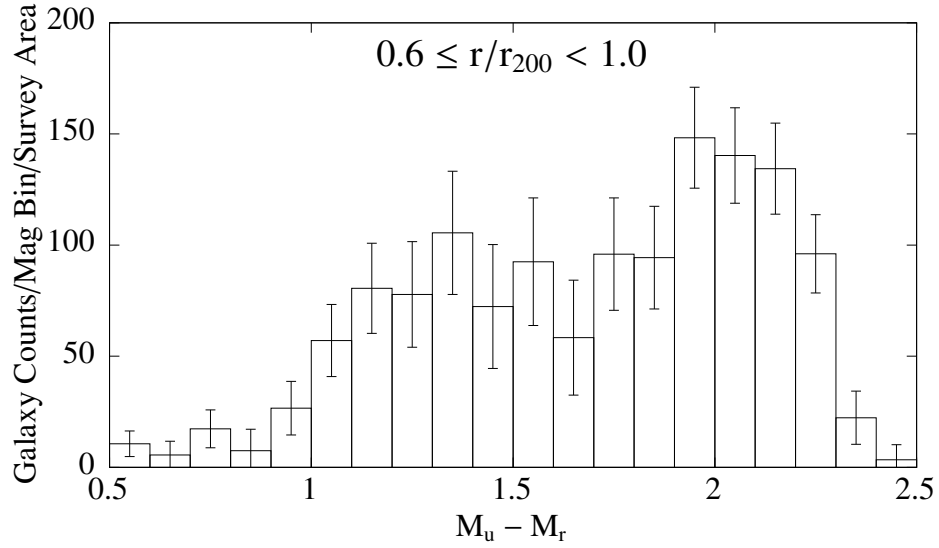


Figure 89. Histogram of dwarf color within  $-19.5 \leq M_r < -17$  for the  $0.6 \leq r/r_{200} < 1.0$  region.

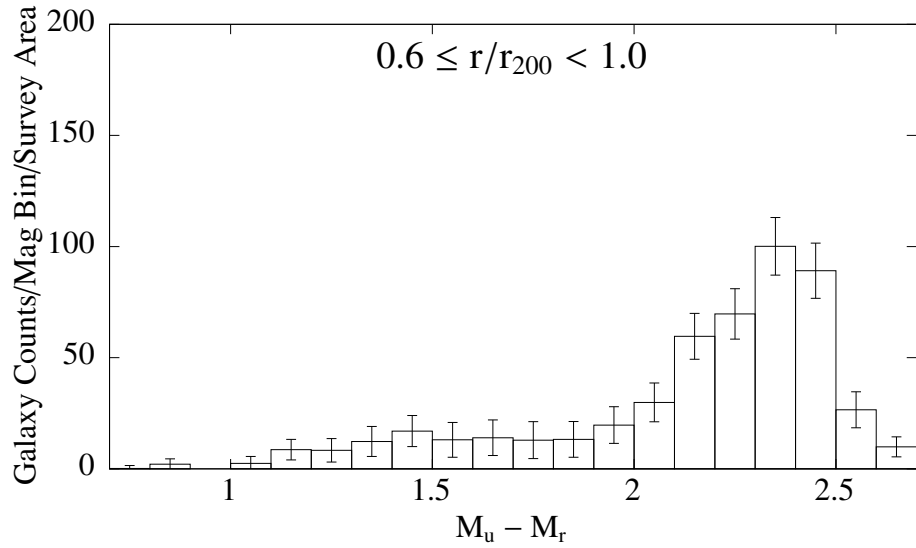


Figure 90. Histogram of giant galaxy color within  $-26 \leq M_r < -19.5$  for the  $0.6 \leq r/r_{200} < 1.0$  region.

blue galaxies is calculated for each radial bin. Explicitly, the blue fraction is given by

$$f_b = \frac{N_b}{N_b + N_r}, \quad (4.16)$$

where  $f_b$  is the blue fraction,  $N_b$  is the number of blue galaxies, and  $N_r$  is the number of red galaxies. The uncertainty in  $N_b$  is determined by

$$\sigma_{N_b} = \sqrt{\sum \sigma_i^2}, \quad (4.17)$$

where the sum is over all of the bins blueward of the color cut. The uncertainty on the number of red galaxies is calculated in a similar fashion using galaxies redward of  $u - r = 1.6$ . The estimate of the uncertainty on  $f_b$  is given by

$$\sigma_{b_f} = \sqrt{\left(\frac{\partial b_f}{\partial N_b}\right)^2 \sigma_{N_b}^2 + \left(\frac{\partial b_f}{\partial N_r}\right)^2 \sigma_{N_r}^2}. \quad (4.18)$$

The partial derivatives are found from

$$\begin{aligned} \left(\frac{\partial b_f}{\partial N_b}\right) &= \frac{1}{N_b + N_r} - \frac{N_b}{(N_b + N_r)^2}, \\ \left(\frac{\partial b_f}{\partial N_r}\right) &= -\frac{N_b}{(N_b + N_r)^2}. \end{aligned} \quad (4.19)$$

The resulting dwarf galaxy blue fractions for the four radial bins are shown in Fig. 91.

This shows an increasing blue fraction with increasing cluster-centric radius. The increase of the outermost blue fraction  $b_{fo}$  relative to the innermost blue fraction  $b_{fi}$  is significant at the  $6.6\sigma$  level:

$$\frac{b_{fo} - b_{fi}}{\sqrt{\sigma_{b_{fo}}^2 + \sigma_{b_{fi}}^2}} = 6.6. \quad (4.20)$$

Due to the slope of the red-sequence, the split between the blue and red fraction is redder by  $\approx 0.2$  magnitudes. Using a cutoff of 1.8, the blue fraction of giants is shown with the dwarfs in Fig. 91. The increase in the blue fraction of giants is more modest than the

dwarfs.

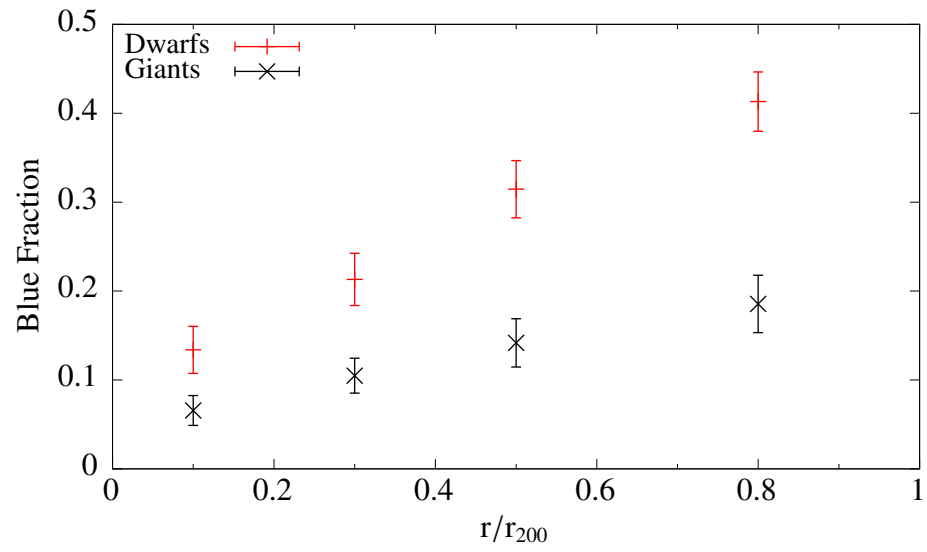


Figure 91. Blue fraction versus cluster-centric radii for dwarfs (red dashed markers) and giants (black X symbols).

## CHAPTER 5

### CLASH CLUSTERS

One way to study galaxy evolution is by comparing galaxies at different stages of their lives. To that end, catalogs of high redshift clusters produced by CLASH (Postman et al., 2012) are compared with the CFHT data.

#### 5.1 Data

The CLASH sample consists of 25 clusters imaged in several filters ranging from ultraviolet to infrared. From the CLASH sample, clusters are chosen that have  $r_{200}$  data available from Merten et al. (2014) and have a redshift range of  $0.185 < z < 0.7$ . The 17 clusters that meet these requirements are shown in Table 9.

For this analysis, all images were observed with HST using the Advanced Camera for Surveys (ACS). Due to the increasing redward shift in wavelength with distance, longer wavelength filters are used for more distant clusters. For clusters with  $0.185 < z \leq 0.4$ , the F435W and F775W filters are used, and for  $0.4 < z < 0.7$  the F475W and F814W filters are used. The response of these filters, along with comparable SDSS filters, are shown in Figs. 92 and 93. The field of view of the ACS is  $202''$  across, which is about  $1/20th$  of Megacam. This limits the data to the inner region ( $r/r_{200} < 0.2$ ) of the clusters.

The CLASH team provides object catalogs for all images. These catalogs were generated using Source Extractor (Sec. 2.2.1). Objects were detected on an image made

Table 9. CLASH target clusters.

Cluster	RA (deg)	DEC (deg)	z	$r_{200}$ (Mpc)	$r_{200}$ (arcseconds)	Red Mag Limit <sup>a</sup>	Blue Mag Limit <sup>a</sup>
A383	42.0141	-3.5292	0.187	2.07 ± 0.53	558 ± 144	-14.07	-13.57
A209	22.9690	-13.6112	0.206	2.17 ± 0.68	532 ± 166	-14.25	-14.02
A2261	260.6133	32.1326	0.224	2.48 ± 1.15	561 ± 261	-14.94	-14.34
RXJ2129	322.4165	0.0892	0.234	1.84 ± 0.67	401 ± 147	-14.79	-14.26
A611	120.2367	36.0566	0.288	1.99 ± 0.60	357 ± 108	-15.71	-14.90
MS2137	325.0632	-23.6611	0.313	2.13 ± 0.47	353 ± 78	-15.83	-15.20
RXJ2248	342.1832	-44.5309	0.348	2.19 ± 0.70	330 ± 105	-16.31	-15.74
MACSJ1115	168.9663	1.4986	0.352	2.04 ± 0.72	303 ± 107	-16.22	-15.69
MACSJ1931	292.9568	-26.5757	0.352	1.87 ± 0.62	279 ± 92	-16.67	-15.89
MACSJ1720	260.0698	35.6073	0.391	1.90 ± 0.72	258 ± 98	-16.33	-15.82
MACSJ0429	67.4000	-2.8852	0.399	1.93 ± 0.85	257 ± 113	-16.59	-15.95
MACSJ1206	181.5506	-8.8009	0.44	1.90 ± 0.76	232 ± 93	-16.29	-16.14
MACSJ0329	52.4232	-2.1962	0.45	1.79 ± 0.87	214 ± 104	-16.10	-16.00
RXJ1347	206.8775	-11.7526	0.451	2.12 ± 0.93	253 ± 111	-16.20	-15.40
MACSJ1311	197.7575	-3.1777	0.494	1.51 ± 0.39	166 ± 43	-16.44	-16.28
MACSJ1423	215.9495	24.0785	0.545	1.61 ± 0.58	163 ± 58	-16.53	-16.85
MACSJ0744	116.2200	39.4574	0.686	1.64 ± 0.46	137 ± 39	-17.50	-17.28

<sup>a</sup> Measured using absolute magnitudes.

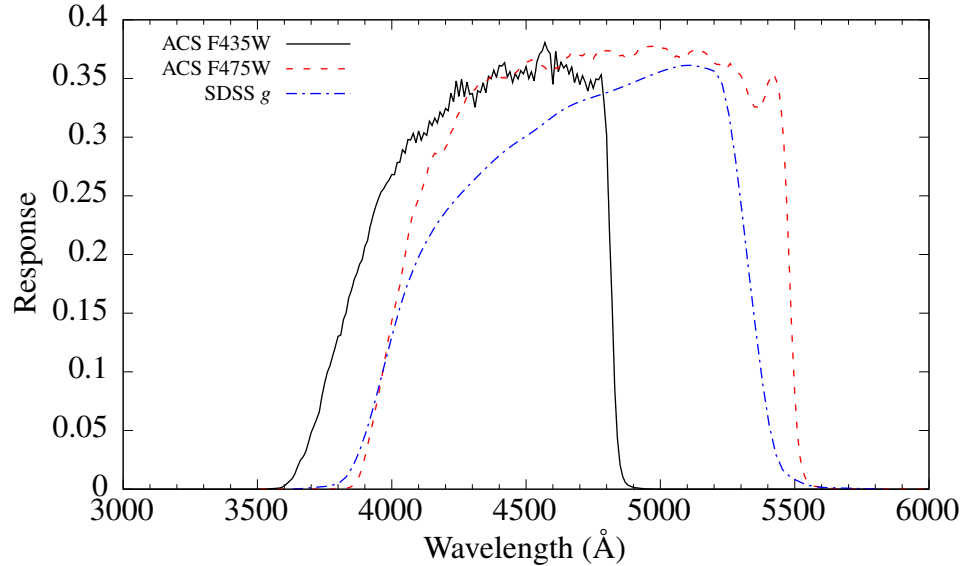


Figure 92. Response of F435W (black solid line), F475W (red dashed line) and SDSS *g*-band (blue dot dashed line) filters.

from the weighted sum of images observed with ACS and the Wide Field Camera 3<sup>3</sup>.

Object flux was measured from pixels that were detected above background (isophotal magnitudes), and an aperture correction was applied to the resulting magnitudes (Holwerda, 2005; Bertin, 2010b). Additionally, the catalogs were corrected for galactic extinction using dust emission maps from Schlegel et al. (1998). Photometric redshift estimates are also provided using the Bayesian Photometric Redshifts algorithm (Benítez, 2000; Benítez et al., 2004; Coe et al., 2006). This method estimates the redshifts of each galaxy based on galaxy colors.

## 5.2 Calibrations

Object classification was completed using the stellarity parameter from Source Extractor. An object is considered a galaxy if its stellarity  $< 0.8$ . The limiting magnitude was determined using the same process outlined in Chapter 3, either 0.8 magnitude before the

<sup>3</sup>More information about the CLASH catalogs can be found at <https://archive.stsci.edu/prepds/clash/>

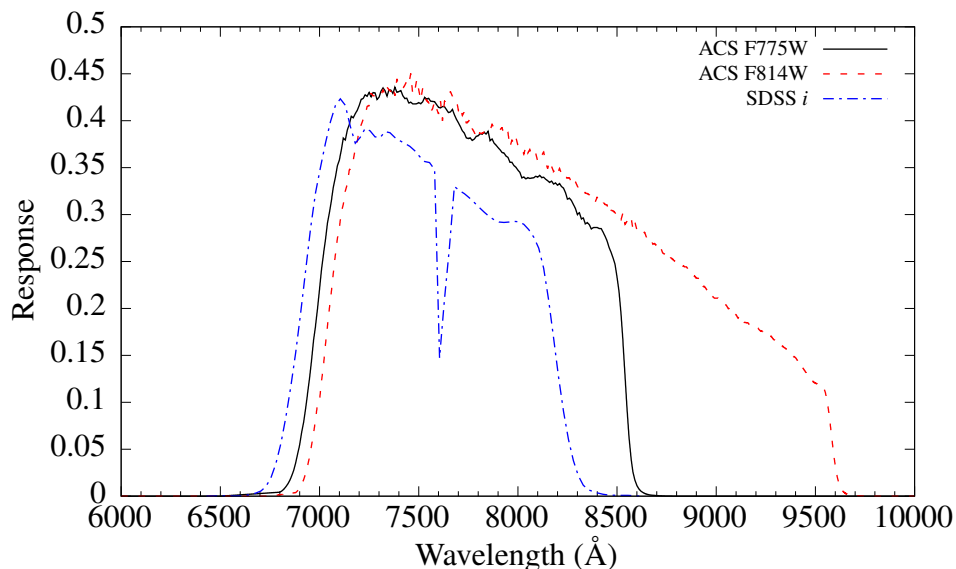


Figure 93. Response of F775W (black solid line), F814W (red dashed line) and SDSS *i*-band (blue dot dashed line) filters.

turnover or the magnitude where the color error exceeds 0.2, whichever is brighter.

Instead of subtracting the number of background galaxies from the number of cluster galaxies to compile a statistical galaxy cluster sample, cluster galaxies are selected via photometric redshifts. A cut of  $z_c \pm 0.1$  was used to select cluster galaxies, where  $z_c$  is the redshift of the cluster (Fig. 94).

Absolute magnitudes were computed assuming the redshift listed in Table 9. The SDSS catalog contains k-corrections determined from photometric redshifts (Csabai et al., 2007) and a best fit spectral type from Dobos et al. (2012). Galaxies from SDSS in several of the CLASH fields were used to provide an estimate for the k-correction of a passive red galaxy and a star forming blue galaxy for the redshift range of the sample (Fig. 95). The resulting k-corrections were interpolated using a cubic spline. A (*blue* – *red*) cut of 1.5 was used to determine whether a galaxy was passive or star forming. This color cut was determined from a color histogram of galaxies within  $z \pm 0.1$  of each cluster (Fig. 96).



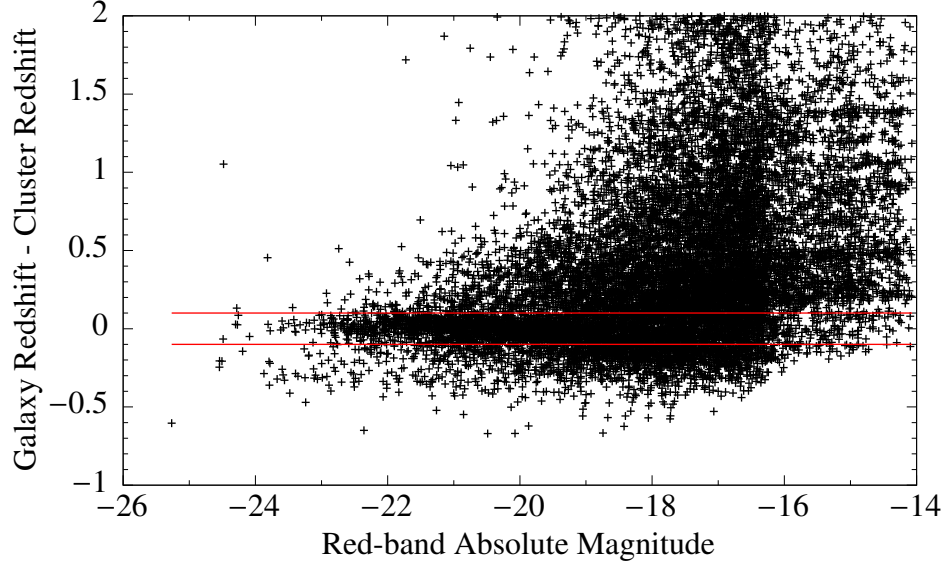


Figure 94. Absolute magnitude is plotted versus  $z_{\text{galaxy}} - z_{\text{cluster}}$  for all clusters. The cut of  $z_{\text{cluster}} \pm 0.1$  is shown as red lines.

Galaxies in the  $0.185 < z \leq 0.4$  range were k-corrected to a redshift of 0.313 and the  $0.4 < z < 0.7$  galaxies were k-corrected to a redshift of 0.473, the median redshift of the two samples.

### 5.3 Results

The CLASH clusters provide a higher redshift comparison with the CFHT sample for the inner cluster region. LFs are constructed following the procedure outlined in Sec. 4.2.2, except a cut in redshift was made to isolate cluster galaxies instead of statistically subtracting background galaxies. The uncertainty is determined from  $\sqrt{N}$ , where  $N$  is the expected number of cluster counts.

The red and blue LFs measured from all CLASH clusters are shown in Figs. 97 and 98. Neither LFs show an upturn at the faint-end, so both were fit using a single Schechter function, similar to the CFHT inner region LFs. The results of the fit are in Table 10.

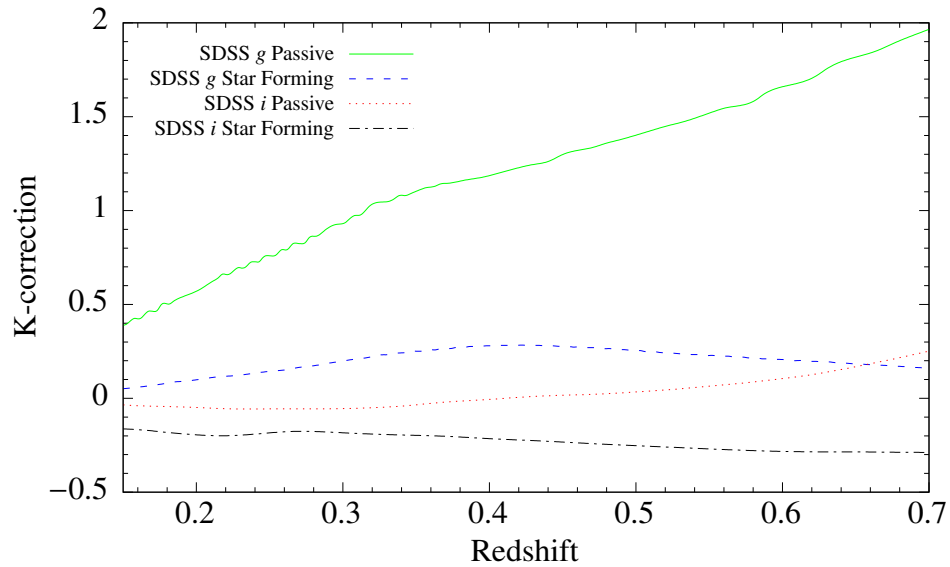


Figure 95. Estimated k-corrections for passive galaxies in the *g*-band (green solid line), star forming galaxies in the *g*-band (blue dashed line), passive galaxies in the *i*-band (red dotted line), and star forming galaxies in the *i*-band (black dot dashed line). The passive galaxies have a large k-correction in the *g*-band due to a sharp drop in luminosity for wavelengths shorter than 4000 Å, which is known as the 4000 angstrom break.

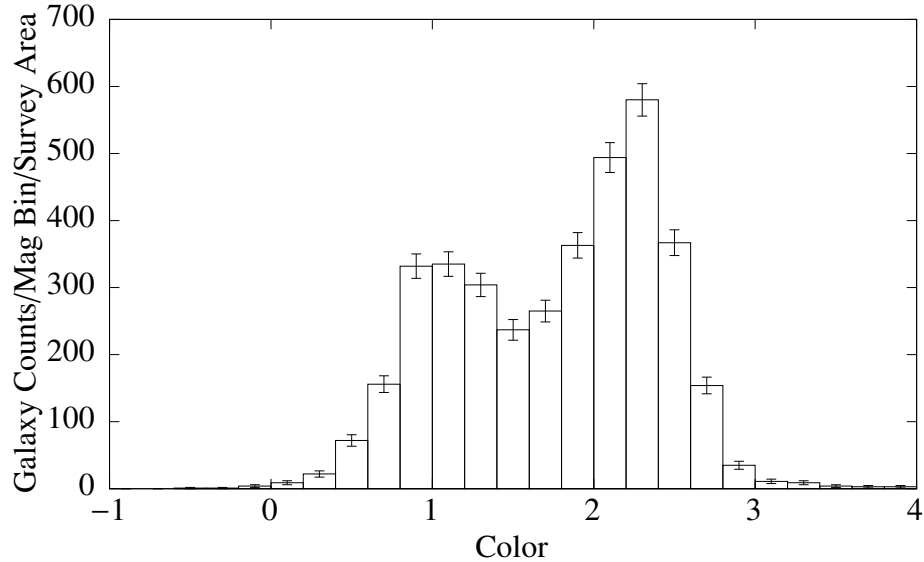


Figure 96. Histogram of the color of all CLASH galaxies within  $z \pm 0.1$  of a target cluster. A color cut of 1.5 is used to distinguish passive and star forming galaxies for applying k-corrections.

Table 10. Parameters derived from fitting a single Schechter function to the red and blue LF.

Band	$M^*$	$\alpha$
Red	$-21.91 \pm 0.11$	$-0.89 \pm 0.02$
Blue	$-19.63 \pm 0.15$	$-0.95 \pm 0.04$

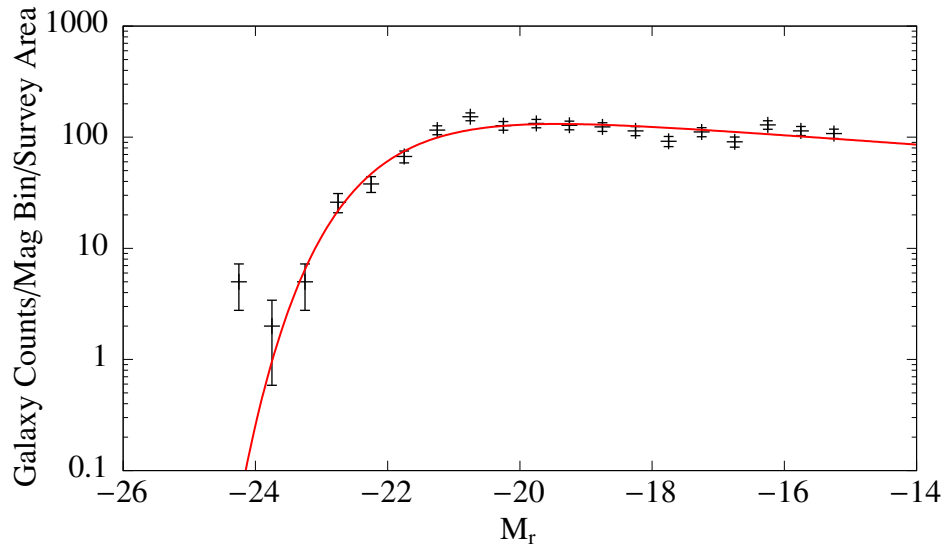


Figure 97. CLASH LF for the red-band fit with a single Schechter function.

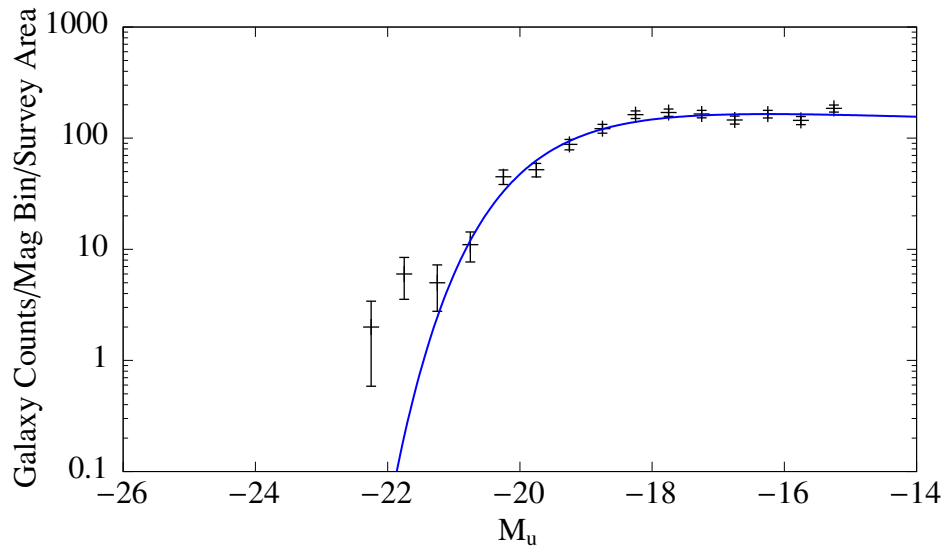


Figure 98. CLASH LF for the blue-band fit with a single Schechter function.

The LF of the higher redshift clusters,  $0.4 < z < 0.7$ , shows a downturn in the number of faint-end counts. Since the errors in the photometric redshift increases with redshift, cluster galaxies at higher redshift may scatter outside of the cut. As shown in Fig. 99, increasing the redshift cut for the higher redshift clusters to  $z_{\text{cluster}} \pm 0.2$  causes an increase in the number of faint galaxies. However, the combined LF from both the high and low redshift clusters using the larger redshift cut for the high redshift sample only shows minor changes in the LF (Fig 100). As such, a cut of  $z_{\text{cluster}} \pm 0.1$  for the entire sample is used for the rest of the analysis.

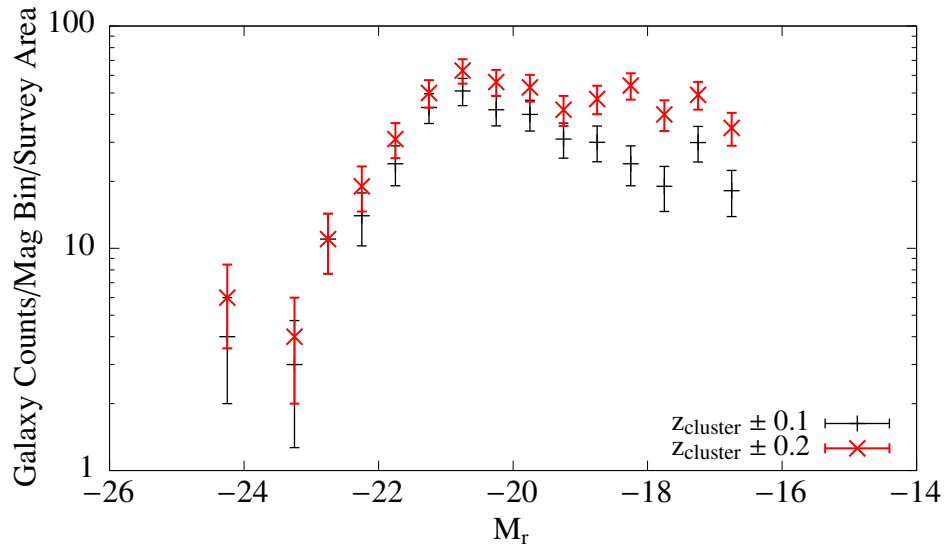


Figure 99. CLASH LF for clusters  $0.4 < z < 0.7$  using a cut of  $z_{\text{cluster}} \pm 0.1$  (black dashed markers) and a cut of  $z_{\text{cluster}} \pm 0.2$  (red x markers).

The separating magnitude between giants and dwarfs is chosen to be  $M^* + 2$  for both the red- and blue-bands. Only seven clusters are deep enough in the blue-band when

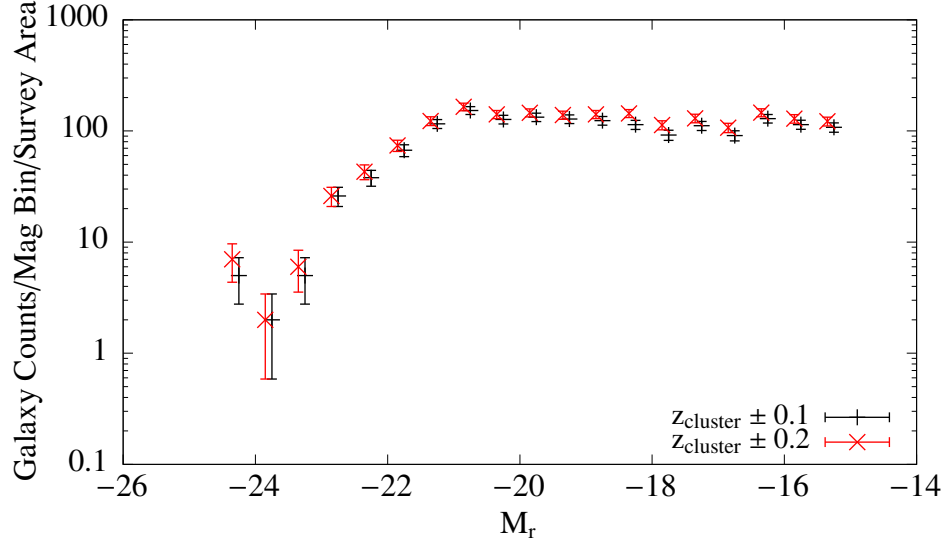


Figure 100. CLASH LF using a cut of  $z_{\text{cluster}} \pm 0.1$  (black dashed markers) for all clusters and using a cut of  $z_{\text{cluster}} \pm 0.2$  for clusters within  $0.4 < z < 0.7$  (red x markers). The latter LF has been offset by 0.1 magnitude.

using a faint-end limit of  $M^* + 4$ . For these seven clusters, the DGRs are given by

$$DGR_{red} = 1.08 \pm 0.10, \quad (5.1)$$

$$DGR_{blue} = 1.22 \pm 0.10.$$

These DGRs are somewhat smaller than the inner region of the CFHT data, though relative changes between the blue and red DGRs is similar. The ratio of galaxies detected in the red band to galaxies detected in the blue band for giants and dwarfs is

$$\frac{N_{BG}}{N_{RG}} = 1.03 \pm 0.09, \quad (5.2)$$

$$\frac{N_{BD}}{N_{RD}} = 1.17 \pm 0.10,$$

where  $N_{BG}$  is the number of blue galaxies,  $N_{RG}$  is the number of red galaxies,  $N_{BD}$  is the number of blue dwarfs, and  $N_{RD}$  is the number of red dwarfs.

The colors of dwarf galaxies in the inner region is bimodal, as can be seen in Fig. 101. These were measured within  $M^* + 2 \leq M_r < M^* + 4.5$  or  $-19.91 \leq M_r < -17.41$ . One cluster, MACSJ0744, was left out due to its bright limiting magnitude. The blue fraction was calculated using a color cut of 1.5, and was computed directly from the color histogram. The resulting blue fraction is

$$f_b = 0.30 \pm 0.02. \quad (5.3)$$

Although the DGR is less in the CLASH sample than in the inner region of the CFHT clusters, the blue fraction is about twice that of the CFHT data. The relative number of dwarf galaxies is heavily influenced from selection effects, and so direct comparisons of DGRs are unreliable. The color fraction, however, shows that the inner region is bluer at higher redshifts. This is known as the Butcher-Oemler effect (Butcher & Oemler, 1978), where higher redshift clusters have a larger fraction of blue galaxies. The reduction in the blue fraction could indicate that star formation has decreased over time from truncation via ram pressure stripping.

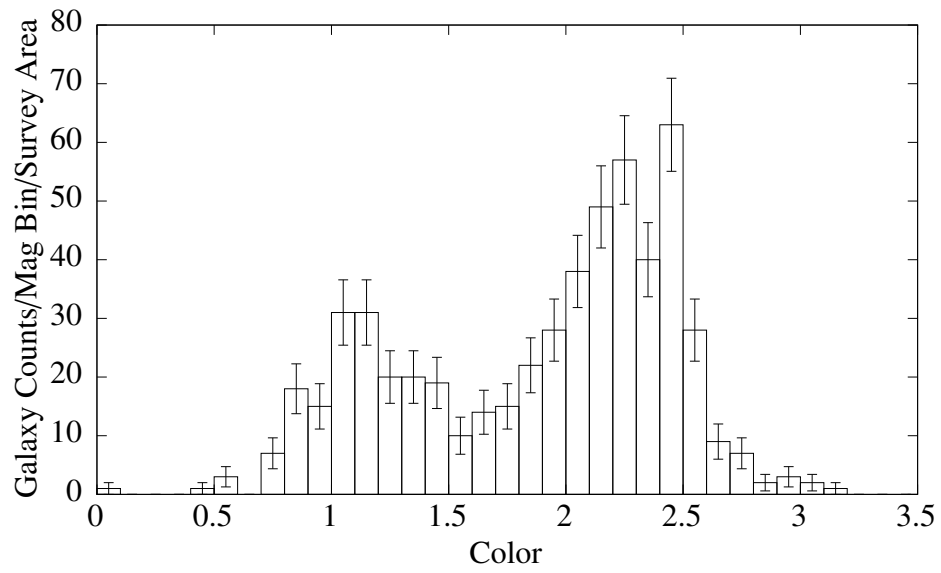


Figure 101. Histogram of galaxy color within a magnitude range of  $-19.91 \leq M_r < -17.41$ .

## CHAPTER 6

### DISCUSSION

The colors and star formation properties of giant galaxies has been subject to numerous studies over the past several decades. Galaxy density has been found to correlate with several properties such as morphology (Dressler, 1980), star formation (Quadri et al., 2012), and color (Balogh et al., 2004). Understanding these relationships for the dwarf population is especially important in untangling environmental effects on galaxy evolution.

#### 6.1 Field and Cluster Luminosity Functions

The LF measured for field galaxies differs from the LF derived from the outskirts of the cluster environment. Blanton et al. (2001) measured field LFs from the SDSS commissioning data. The field LFs were fit using a single Schechter function as they do not have an upturn at the faint-end. The resulting fits are shown with the outermost CFHT LF in the  $r$ -band (Fig. 102) and in the  $u$ -band (Fig. 103). The field LFs have been normalized to match the bright-end of the CFHT LFs.

The field LF is shallower at the faint-end relative to the outer region of the CFHT clusters. This implies that the survival rate of dwarf galaxies is highest in the outskirts of clusters compared to the field and the inner cluster region. This is expected for the inner region of clusters as dwarf galaxies are likely to be destroyed by tidal disruptions in denser environments (Martel et al., 2012). Consistent with these results, Thompson &



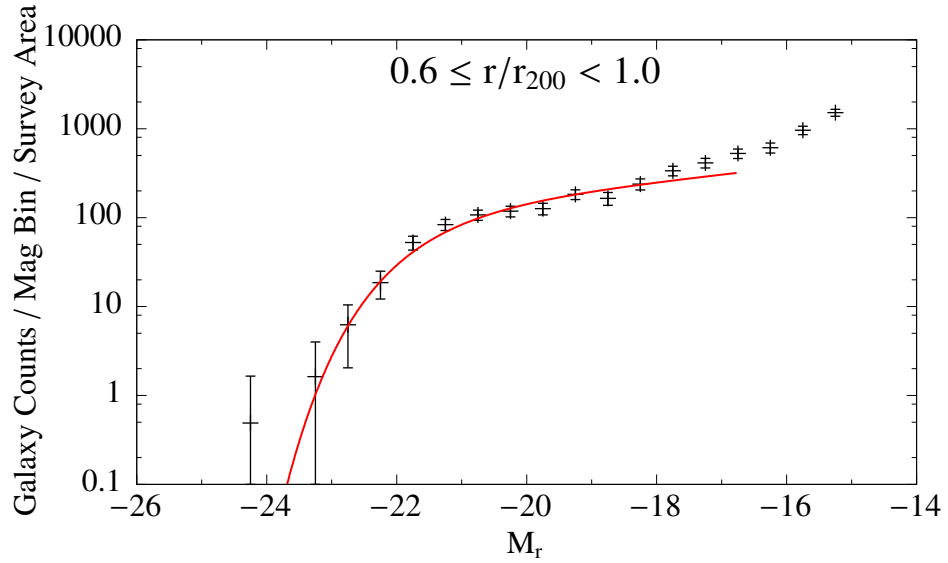


Figure 102. The  $r$ -band LF for the  $0.6 \leq r/r_{200} < 1.0$  region of the CFHT clusters (black markers) shown with the field LF from Blanton et al. (2001; solid red line). The field LF has been converted to my adopted cosmology and scaled to match the bright-end of the CFHT LF.

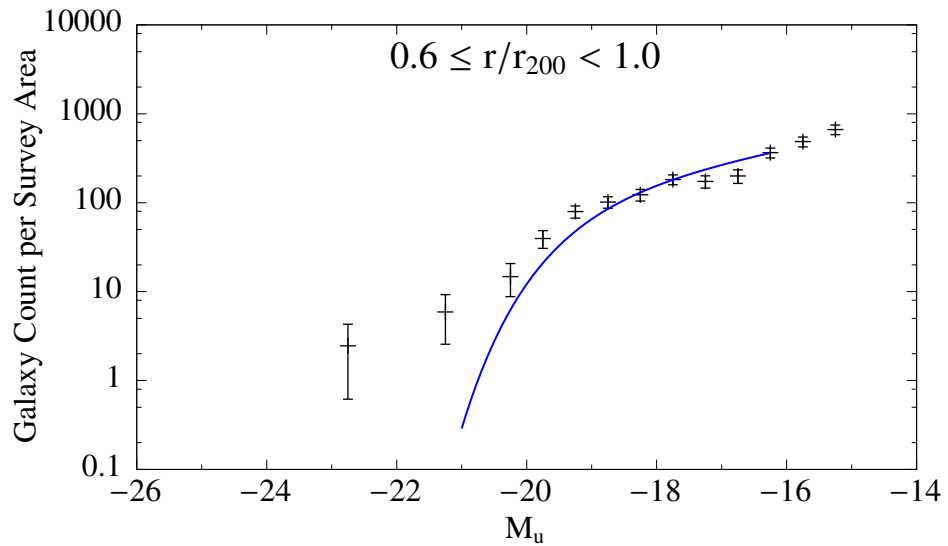


Figure 103. The  $u$ -band LF for the  $0.6 \leq r/r_{200} < 1.0$  region of the CFHT clusters (black markers) shown with the field LF from Blanton et al. (2001; solid blue line). The field LF has been converted to my adopted cosmology and scaled to match the bright-end of the CFHT LF.

Gregory (1993) found that less centrally concentrated dwarf galaxies (dSph) are absent in the center of the Coma cluster.

An important comparison is the faint-end slope of the field  $r$ -band LF relative to the field  $u$ -band LF. The Schechter function for the  $u$ -band has a steeper slope ( $\alpha = -1.35$ ) compared to the  $r$ -band ( $\alpha = -1.20$ ; Fig. 104). The change in slope at the faint-end of the  $u$ - and  $r$ -band LFs measured from the outer region of the CFHT clusters is not as large as the change between the field  $u$ - and  $r$ -band LFs. This is consistent with quenching of star formation as dwarf galaxies fall into the cluster environment.

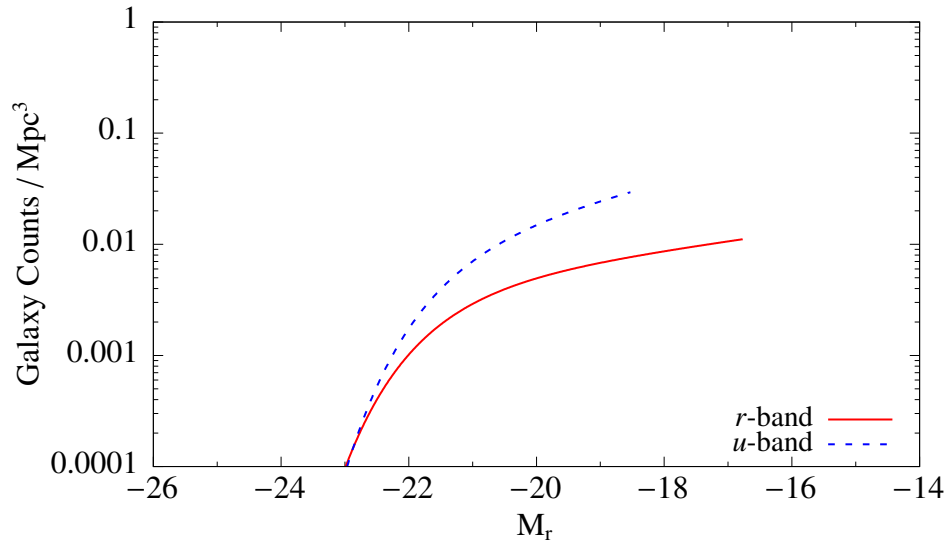


Figure 104.  $r$ -band (red solid line) and  $u$ -band (blue dashed line) LFs for field galaxies from Blanton et al. (2001). The  $u$ -band LF has been shifted by 2.26 magnitudes to the left. The LFs are plotted with the original measured normalization constants converted to my adopted cosmology. The normalization constants have units of  $\text{Mpc}^{-3}$ .

Due to the small field of view of the ACS camera, only the inner region of the CLASH clusters was observed. The CLASH blue-band LF shows a slightly higher slope than that of the CLASH red-band LF. As can be seen in Fig. 101, the dwarf population

contains a non-negligible blue population of dwarf galaxies. Without observations of the outer region of the CLASH sample, deprojected LFs cannot be measured. Thus it is not possible to tell if the blue population is really in the central region of the cluster or it is just a projection effect.

## 6.2 Comparisons of Dwarf-to-Giant Ratios

For the inner region, the DGR for the CLASH sample is lower than the DGR of the CFHT clusters. This is expected from the comparison of the CLASH and CFHT LFs. The LFs for the inner region of the CFHT clusters have a steeper faint-end slope than the CLASH data, implying a larger number of dwarf galaxies in the CFHT clusters.

The methods used to detect objects from CFHT and CLASH was different (PPP versus `Source Extractor`). When comparing LFs generated with different background fields in Sec. 4.2.6, the use of background fields measured using `Source Extractor` had a large effect on the faint-end slope compared to fields measured using PPP. Therefore, direct comparisons between DGRs are uncertain, as the number of dwarf galaxies can be greatly affected by the object detection and classification method employed. The CFHT data was measured using PPP as it offers more control over the input catalog compared to `Source Extractor`. The chosen background fields for the CFHT data were measured using PPP to minimize systematic differences between the CFHT cluster and CFHT background fields.

The  $r$ -band DGR versus cluster-centric radius for the CFHT clusters increases for  $r \gtrsim 0.4 r_{200}$ . The DGR selected from a sample of 57 low redshift Abell clusters (Barkhouse et al., 2009) shows a steady increase from the inner to the outer region.

The differences in the DGR may indicate systematic differences between

estimations of  $r_{200}$  between Barkhouse et al. (2009) and my sample. The richness method used to estimate  $r_{200}$  was different ( $\lambda$  vs  $B_{gc}$ ) as was the sample of clusters used to generate the relationship between richness and  $r_{200}$ . Both cases, however, indicate a suppression of dwarf galaxies in the inner region of low redshift clusters. Even if there are systematic differences between the two samples, comparisons within the CFHT data is valid as  $r_{200}$  is calculated in the same way for all of the CFHT clusters.

### **6.3 Colors of Galaxies versus Density**

A previous study carried out by Balogh et al. (2004) looked at the color of galaxies as a function of local density and magnitude. They found that the blue population is smaller in number for brighter galaxies at low densities compared with fainter galaxies (Fig. 105).

Galaxy colors measured from the CFHT data show an increase in the number of blue galaxies with increasing cluster-centric radius for dwarf galaxies, while the change in the number of blue giants is much smaller. The dwarf galaxy colors for the outermost region of the CFHT clusters show a bimodal distribution of roughly equal numbers (Fig. 89). Comparison with the bottom row of Fig. 105 indicates that the outer region of the cluster is still a relatively dense region, assuming the trends from Balogh et al. (2004) continue to fainter luminosities.

### **6.4 Butcher-Oemler Effect**

The CLASH data shows an increase in the blue fraction for the dwarf population of the high redshift sample compared to the low redshift clusters. The standard view for cluster evolution is that star forming galaxies fall into the cluster environment from the field or groups and are quenched by some physical mechanism. The correlation between blue

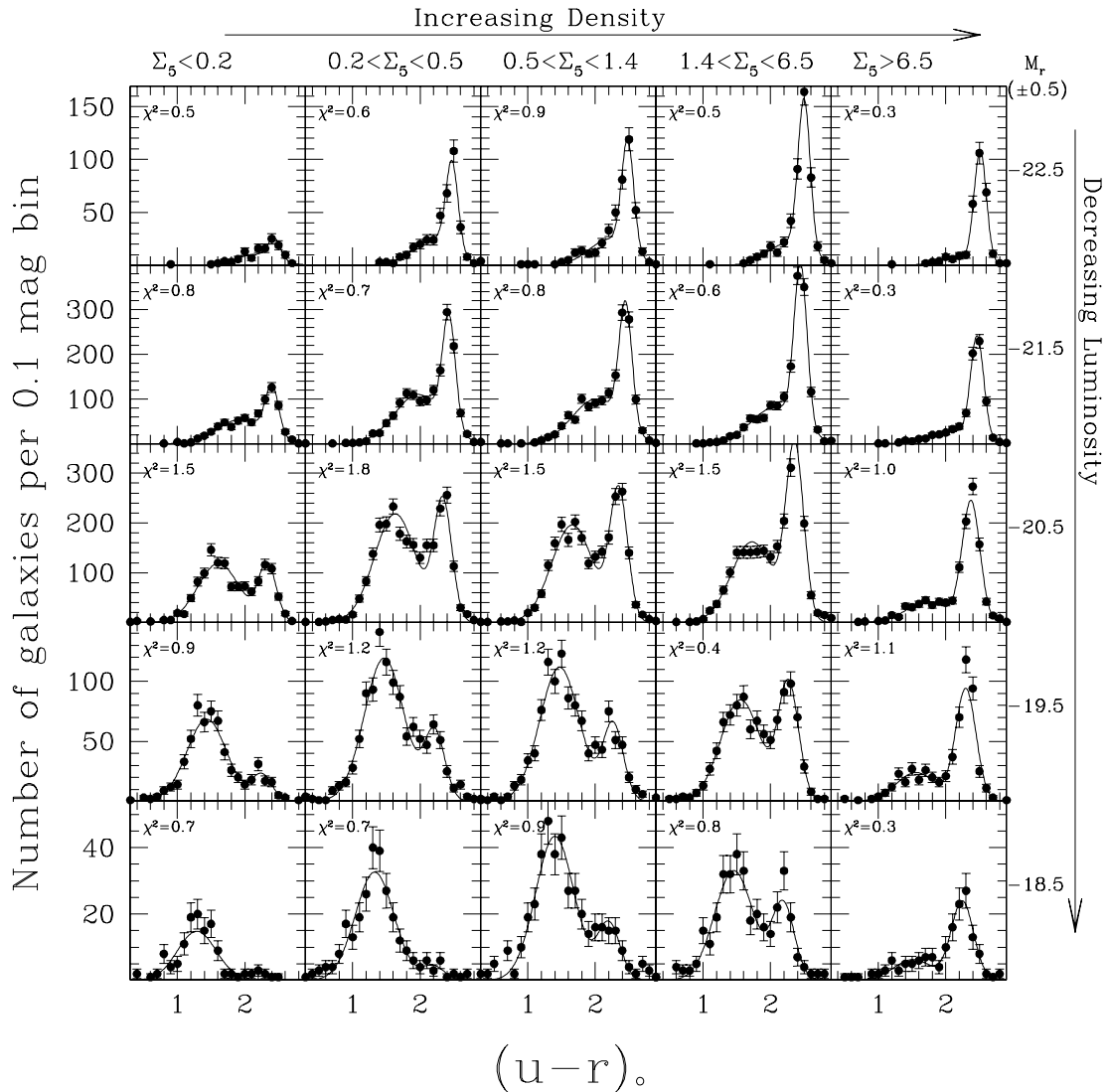


Figure 105. Galaxy color as a function of magnitude and local density. The bright galaxies show a small blue population across all densities, while the blue population dominates the fainter galaxy population in low densities. Reproduced from Balogh et al. (2004).

fraction and redshift can be explained as an increase in the number of infalling galaxies, as predicted by cosmological simulations. The efficiency by which the physical mechanisms quench star formation remains constant, as the decrease in blue fraction is simply due to less blue galaxies being accreted with time.

Ellingson et al. (2001) measured the blue fraction for bright cluster galaxies for redshifts ranging from  $0.2 < z < 0.5$  (Fig. 106). They found an increase in the blue fraction with redshift when measuring all galaxies within  $1.0 r/r_{200}$ . They did not find such a relation for cluster galaxies within  $0.5 r/r_{200}$ .

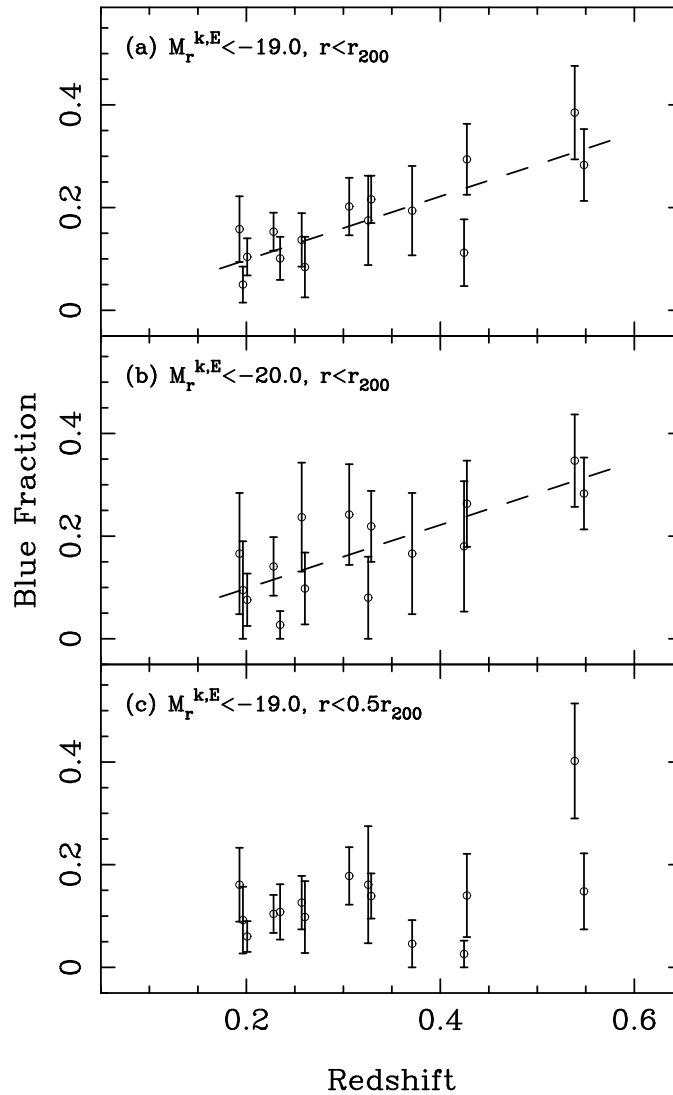


Figure 106. Blue fraction versus redshift from the CNOC1 sample of clusters. The Butcher-Oemler effect is present when measuring galaxies within  $1.0 r/r_{200}$ , but not within  $0.5 r/r_{200}$ . Reproduced from Ellingson et al. (2001). Note that Ellingson et al. use the Gunn  $r$  filter and magnitudes are calculated assuming a cosmology of  $H_0 = 100 \text{ km/s/Mpc}$  and  $q_0 = 0.1$ .

The blue fraction measured from the CLASH data is divided into two separate

redshift bins,  $0.185 < z < 0.4$  and  $0.4 < z < 0.7$ , and compared with the inner region of the CFHT clusters. The results are similar to Ellingson et al. for the giants; no change in the blue fraction with redshift is seen (Fig. 107). The dwarfs, however, show a clear trend towards increasing blue fraction with increasing redshift.

The blue fractions for giants from the CFHT data ranges from  $f_b = 0.07 \pm 0.02$  in the innermost region to  $f_b = 0.19 \pm 0.03$  in the outermost region. This range is comparable to the blue fractions measured from clusters at  $z \approx 0.2$  shown in Fig. 106.

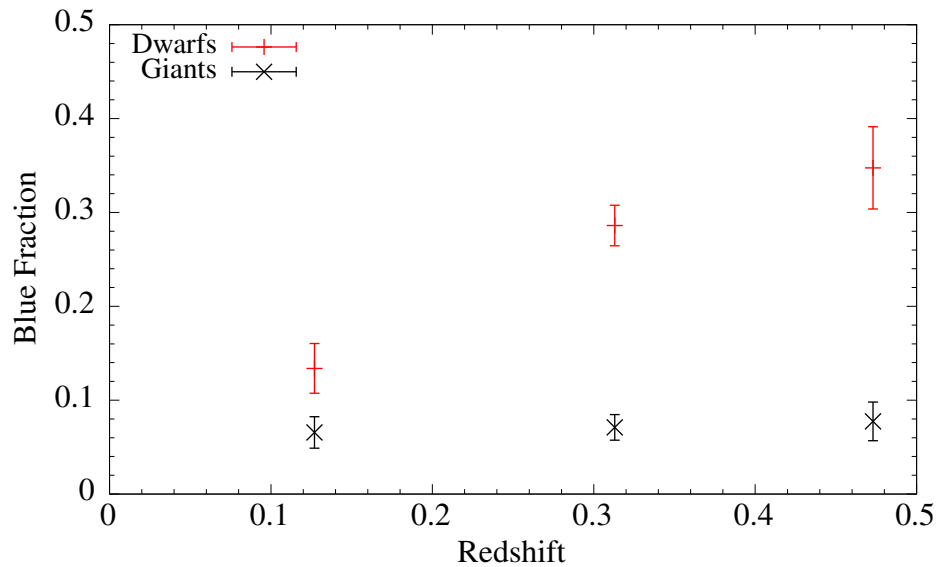


Figure 107. Blue fraction for three redshift bins measured from CFHT and CLASH clusters within  $0.2 r/r_{200}$ . Dwarfs are displayed as red dashed markers and giants are shown as black X symbols.

Comparisons of the CFHT clusters with Barkhouse et al. (2009) show interesting differences. Their blue fraction for the giants changes the most dramatically, reaching the same level as the dwarfs in the outer region (Fig. 108). The blue fraction for dwarfs, however, changes dramatically in the inner region, and levels off in the outer region. The differences with the CFHT data may be due to the filters used. Barkhouse et al. use

$B$ -band for their blue filter. The two filters ( $u$  and  $B$ ) may sample different stellar populations and thus the  $B$ -band may indicate star formation on a different timescale (Larson & Tinsley, 1978).

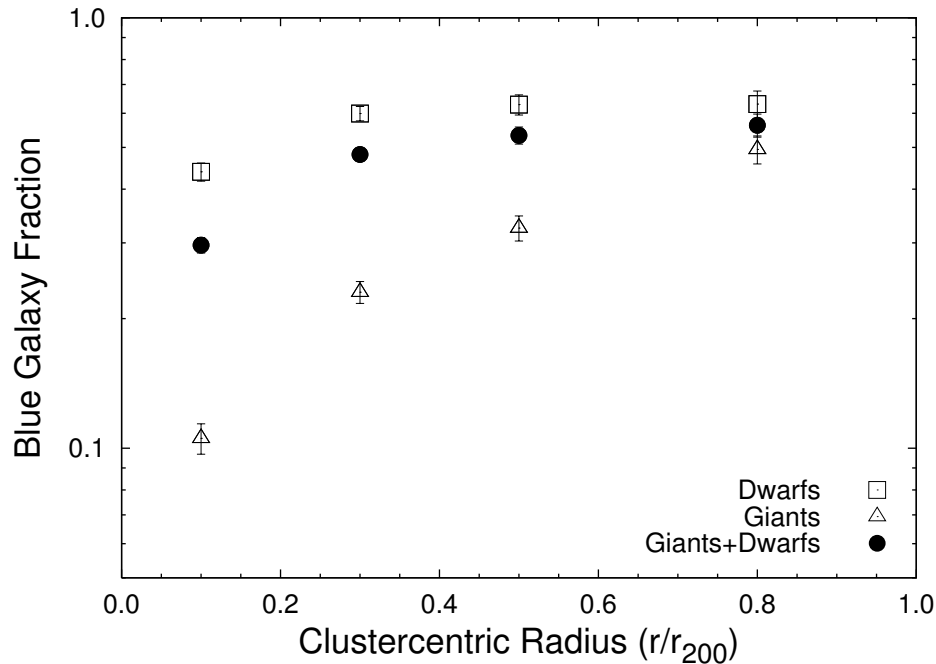


Figure 108. Blue galaxy fraction for dwarfs (squares), giants (triangles), and dwarfs + giants (filled circle) reproduced from Barkhouse et al. (2009). The dwarf blue fraction increases in the inner regions and then levels off in the outer region. The giant blue fraction increases the most dramatically.

### 6.5 Star Formation in Dwarf Cluster Galaxies

An important goal in the study of galaxy evolution is to determine which physical mechanism is responsible for the differences between cluster and field galaxies. One way of probing the effect of the cluster environment is tracing star formation via  $u - r$  color. Physical mechanisms can be differentiated by determining the region in which star formation is quenched. The relative location can only be determined if the quenching of star formation occurs over a short time period. Galaxy starvation is effective on timescales



of  $\approx 10^9$  years, where as ram pressure could remove the gas within a disk in  $10^8$  years (Quilis et al., 2000), though some simulations show it could take much longer (Tonnesen et al., 2007). If truncation happens over  $10^8$  years, it may be possible to determine its location within a cluster, as typical timescales for a galaxy crossing a cluster is on the order of  $10^9$  years. The change in blue fraction and luminosity functions with respect to cluster-centric radii implies quenching timescales  $\lesssim 10^9$  years.

The  $u - r$  color is limited in its ability track star formation on very short timescales. The  $u - r$  color is sensitive to the average star formation rates over the past  $10^8$ - $10^9$  years (Kennicutt, 1998), which makes determining the location of quenching as a function of cluster-centric radius difficult.

The relatively shallow correlation between blue fraction and cluster-centric radii of giants compared to dwarfs is consistent with giant galaxies having been preprocessed prior to falling into the cluster environment. This is plausible as larger galaxies are more likely to fall into a cluster as part of a group than dwarfs (McGee et al., 2009). The difference in color between giant and dwarf galaxies can be explained with a physical process like starvation, which is effective in smaller groups. A higher fraction of giant galaxies are quenched in the group environment prior to falling into a cluster. A higher fraction of dwarfs have their star formation quenched in the cluster environment as they are accreted in isolation.

If there is no preprocessing, than the effects of the cluster environment appear to be more effective in giants, as their blue fractions are lower than dwarfs, especially in the outskirts of clusters. This scenario requires an alternative physical mechanism such as AGN feedback (Dubois et al., 2013) as most of the proposed processes (e.g. ram pressure,

galaxy harassment, and starvation) are more effective on dwarfs.

The accretion of galaxies and groups into clusters was studied by McGee et al. (2009) using simulated galaxy clusters and groups in four redshift bins: 0, 0.5, 1, and 1.5. They find that the fraction of galaxies accreted as part of a group slowly increases with decreasing redshift. At  $z = 0$ , 45% of galaxies that fall into a cluster the size of Coma do so in a large group. At  $z = 1.5$ , it drops to 40%. Roughly 80% of massive galaxies are accreted in a small group or larger collection compared to  $\approx 60\%$  for less massive galaxies.

Projection effects could explain the differences in blue fraction between dwarfs and giants in the inner region of the CLASH data. In agreement with the results from the CFHT and CLASH data, Dahlén et al. (2002) found an increasing blue fraction in the cluster Cl 1601+42 ( $z = 0.54$ ) with magnitude. Shown in Fig. 109 is the blue fraction versus limiting magnitude cut for Cl 1601+42. Since the blue fraction gets larger when including fainter galaxies, the perceived Butcher-Oemler effect in the inner region of the CLASH sample might be caused by blue galaxies in the outer region projected onto the inner region. This effect would be larger in higher redshift clusters, assuming the blue fraction increases with redshift.

As will be discussed, quenching timescales have been studied using numerous methods with mixed results. Using ultraviolet data from the *GALEX* space telescope, Hammer (2012) found that the majority of dwarf galaxies in the Coma cluster being transformed from star forming to passive galaxies were quenched with timescales  $< 10^9$  years.

Very recently, Peng et al. (2015) compared the metallicity of star forming and

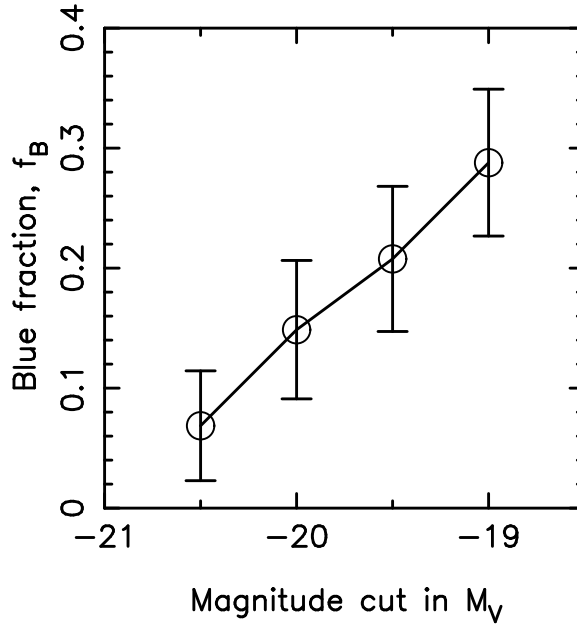


Figure 109. Blue fraction versus limiting magnitude cut for Cl 1604+42. Reproduced from Dahlén et al. (2002).

passive galaxies that have spectra in SDSS. Since the majority of galaxies reside in groups, these results are indicative of the quenching process in the group environment. While accreting gas, the increase in metallicity of the interstellar material is modest as the accreted gas dilutes the interstellar gas. Quick removal of the interstellar material will stop star formation, and the metallicity will be held fixed. Alternatively, just removing the gas feeding the galaxy (i.e. galaxy starvation) will cause the metallicity to increase more rapidly as the interstellar material is not being diluted. Peng et al. found the metallicity of passive galaxies to be consistent with the starvation scenario.

A simulation of a galaxy cluster with  $6.4 \times 10^{14} M_{\odot}$  of dark matter by Tonnesen et al. (2007) shows that most of the gas loss that occurs in large galaxies is from ram pressure stripping. Although ram pressure is strongest in the central region of clusters, it can be effective as far as 2 Mpc from the cluster center. Tonnesen et al. find that gas

stripping occurs over long time periods ( $\geq 10^9$  years). They also find that the accretion of gas would be halted  $\approx 2.4$  Mpc from the cluster center.

## CHAPTER 7

### SUMMARY

The reduction, calibration, and analysis of 15 galaxy clusters obtained from the archives of the Canada-France-Hawaii Telescope observed with Megacam was presented.

Calibrated images were combined using `Source Extractor`, `Scamp`, and `SWarp`. Object detection, magnitude measurements, and object classification was completed using the `Picture Processing Package`. The brightest cluster galaxy, along with neighboring giant galaxies, were modeled and removed using `Ellipse`.

Objects magnitudes were brought onto the AB magnitude system by calibrating to extinction corrected (Schlegel et al., 1998) bright stars (*r*-band) or bright galaxies (*u*-band) from SDSS. Absolute magnitudes were calculated using a *k*-correction based on redshift and color (Chilingarian et al., 2010; Chilingarian & Zolotukhin, 2012).

The red-sequence for each cluster was fit with a straight line, and the dispersion was measured using rotated colors so that the red-sequence had a slope = 0 (i.e. the red-sequence was horizontal). Using the measured red-sequence,  $\lambda$  richness was calculated for each cluster. The dynamical radius  $r_{200}$  was computed for a subset of clusters with known velocity dispersions, and a relationship between  $\lambda$  and  $r_{200}$  was used to estimate  $r_{200}$  for the rest of the sample.

Combined luminosity functions were constructed in four radial bins:

$0.0 \leq r/r_{200} < 0.2$ ,  $0.2 \leq r/r_{200} < 0.4$ ,  $0.4 \leq r/r_{200} < 0.6$ , and  $0.6 \leq r/r_{200} < 1.0$ . The

$r$ -band LF has an upturn in the faint-end and so it is not well described by a single Schechter function, and therefore a double Schechter function was fit. The slope of the faint-end upturn increased with increasing radius, similar to other studies. The relative size of the slope, however, is lower than Barkhouse et al. (2007) and Popesso et al. (2006). The  $u$ -band LF is shaped similar to the  $r$ -band, and the outer region  $u$ -band LF has an increased slope relative to the  $r$ -band.

The faint-end slope of the deprojected LFs for the  $0.0 \leq r/r_{200} < 0.2$  region is lower than the projected LFs. The deprojected  $u$ -band LF has a similar faint-end slope to the  $r$ -band LF, which indicates no star formation activity in the inner region of the cluster sample.

LFs measured from the Coma cluster (Beijersbergen et al., 2002; Hammer et al., 2012) were similar to the CFHT LFs. The large scatter in the LFs by Beijersbergen et al. make it impossible to determine if there is an upturn at the faint-end of their LF.

The DGR in both the  $r$ - and  $u$ -band start to increase at  $0.4 r/r_{200}$ . The  $u$ -band DGR is larger than the  $r$ -band, and the difference increases with increasing cluster-centric radius. The DGR from Barkhouse et al. (2009), on the other hand, increases steadily.

The differences in the slope of the faint-end  $u$ -band LF relative to the  $r$ -band LF in the outer region of the cluster sample is not as large as the differences between the field  $u$ - and field  $r$ -band LFs. This indicates a truncation of star formation as galaxies fall into the cluster environment. The ability to determine the physical mechanism responsible for quenching star formation is complicated by the relatively poor precision of the  $u - r$  colors to differentiate between current and recent star formation (Kennicutt, 1998).

The distribution of galaxy colors in the CFHT clusters is bimodal with a

population of red and blue galaxies. The blue fraction for dwarf galaxies steadily increases with cluster-centric radius. The giant blue fraction increases much slower than the dwarf galaxy blue fraction. The blue fraction from Barkhouse et al. (2009) is the opposite, with a dramatic change in the giant blue fraction. The dwarf blue fraction from Barkhouse et al. only increases in the inner region, as it levels off in the outer region. The differences may be caused by the filters used to calculate the blue fraction. Barkhouse et al. use a  $B$ -band filter which may track a different stellar population than the  $u$ -band and thus be less sensitive to recent star formation.

Additionally, catalogs of 17 clusters produced by the “Cluster Lensing and Supernova survey with Hubble” (Postman et al., 2012) were analyzed. The clusters were observed with the ACS using HST. The clusters range from  $0.185 < z < 0.7$ . Appropriate filters were chosen shortward and longward of the  $4000\text{\AA}$  break in order to provide a fair comparison.

The small field of view of the ACS camera means that only the inner region of the clusters were observed. The LFs in the inner region are flat, with no obvious upturn at the faint-end. The slope of the blue-band is slightly greater than the red-band. The slopes for the CFHT data are a little larger than the CLASH data, though deprojected LFs are required to confirm that it is a real effect.

Comparisons of the inner region of the CFHT and CLASH clusters show that the blue fraction of the dwarf population increases with redshift, while the blue fraction of the giants changes very little. For the giants, this is consistent with Ellingson et al. (2001). To my knowledge, this is the first measurement of the Butcher-Oemler effect for dwarf galaxies. Deprojected blue fractions are required to determine if the increase in the blue

fraction in the inner region is real or if it is a projection effect.



## CHAPTER 8

### FUTURE WORK

The biggest limitation of the results is due to the low precision of the  $u - r$  color in determining recent star formation. Models created using GALEV (Kotulla et al., 2009) show that at present times  $u - r$  color is unable to tell if a galaxy experiences a burst of star formation prior to truncation (Fig. 110). Measurements of  $H\alpha$  equivalent widths can

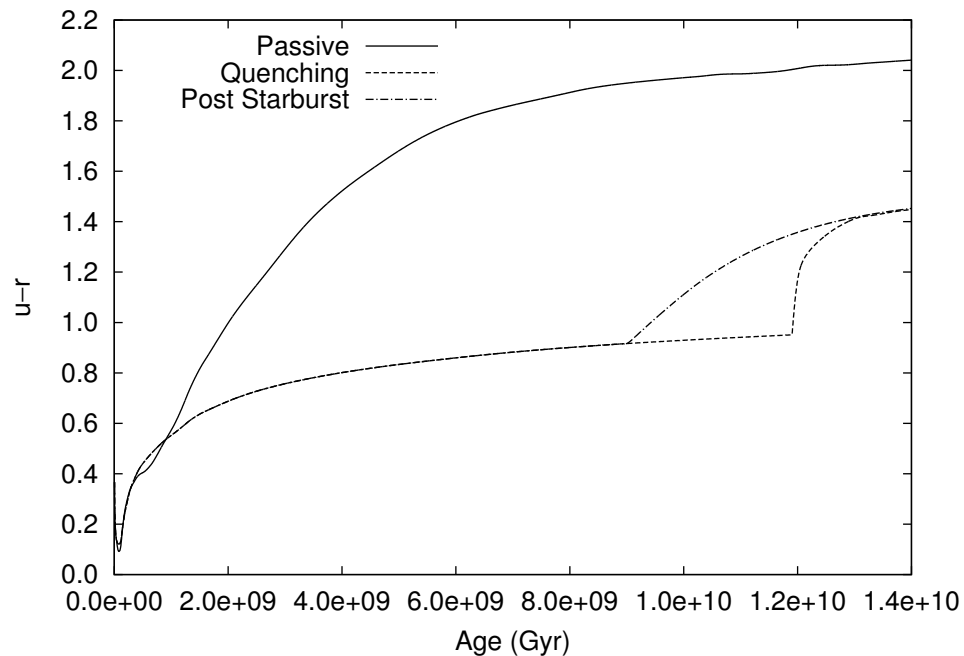


Figure 110. The passive (solid), quenching (dashed), and post starburst (dot-dashed) lines trace the change in  $u - r$  of a simulated galaxy with time. At present times (far right) galaxies that experienced a burst of star formation before quenching are indistinguishable from galaxies that were quenched without experiencing a burst of star formation.

be used to differentiate between different star formation histories. The GALEV models

predict that  $u - r$  versus the equivalent width of  $H\alpha$  can determine whether a burst of star formation occurred before the quenching of star formation (Fig. 111).

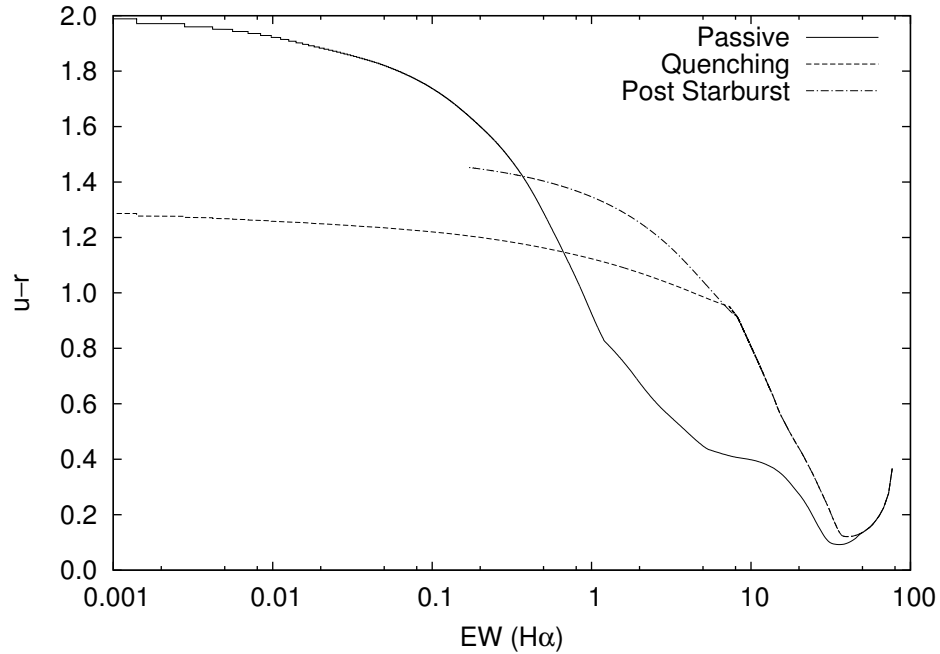


Figure 111. The passive (solid), quenching (dashed), and post starburst (dot-dashed) lines trace the change in the equivalent of  $H\alpha$  and  $u - r$ . The lines start at the right at  $\approx 1$  billion years after the big bang, and move left with increasing time. The addition of  $H\alpha$  allows the differentiation between quenching with and without a prior burst of star formation.

We have been granted several nights at the 4-meter telescope at the Kitt Peak National Observatory to measure  $H\alpha$  emission of galaxy clusters using narrowband filters (Bechtold et al., 1997). These results will allow us to probe star formation on shorter timescales in order to determine the dominate physical mechanism acting in clusters.

Spectra from SDSS can be combined with  $u - r$  color measurements of galaxies in low redshift clusters to measure star formation activity. Specific star formation rates derived by Brinchmann et al. (2004) are compared with the colors of galaxies in Abell 2199 in Fig. 112. The vertical line denotes the separation between passive and star

forming galaxies using specific star formation rates, while the horizontal line splits the two populations using  $u - r$ . Comparing the spectra with the low redshift cluster sample can help constrain the timescales of star formation probed by the  $u - r$  colors.

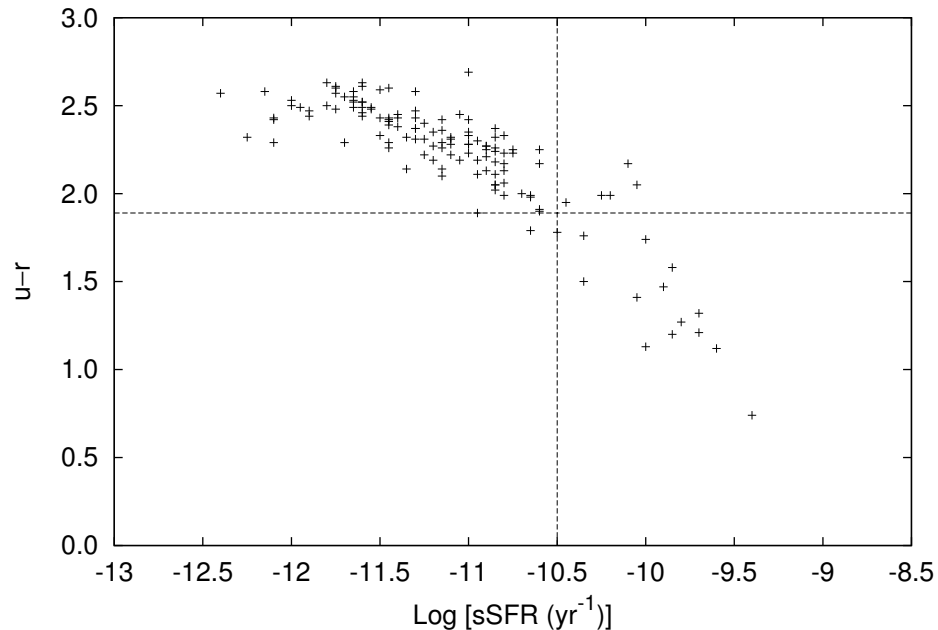


Figure 112. Specific star formation rates from Brinchmann et al. (2004) versus  $u - r$ . A vertical cut in specific star formation separates star forming and passive galaxies. The horizontal dividing line shows a value of  $u - r$  that could differentiate between the two populations.

Morphology is another way to track evolutionary changes in galaxies. For instance, the morphology–density relationship (Dressler, 1980) found in low redshift clusters is not as universal at higher redshifts. At a redshift of  $\approx 0.5$  the relation holds for massive concentrated galaxy clusters, but not for less concentrated irregular clusters (Dressler et al., 1997).

In this thesis, dwarf galaxies have been selected based upon their absolute magnitude. However, they are generally classified via morphology. Work to develop an automated morphology program is currently underway based on the asymmetry and

central concentration of galaxies (Abraham et al., 1996). Comparisons of star formation rates with morphology can help uncover the relationship between dwarf irregulars and dwarf ellipticals.

The CLASH cluster sample suffered from limited coverage as only the lower redshift clusters were deep enough to probe dwarf galaxies. The Frontier Fields are very deep observations of six galaxy clusters using HST within a redshift range  $0.30 < z < 0.55$ . Additionally, a nearby “parallel field” for each cluster is observed that probes the cluster infall region. This data offers an unprecedented opportunity to compare the dwarf galaxy population between low and high redshift clusters, including studying the Butcher-Omeler effect in dwarf galaxies. Furthermore, the high resolution of HST allows for precise morphological studies even at moderate redshifts.

## BIBLIOGRAPHY

- Abell, G. O., Corwin, Jr., H. G., & Olowin, R. P. 1989, *ApJS*, 70, 1
- Abraham, R. G., Tanvir, N. R., Santiago, B. X., et al. 1996, *MNRAS*, 279, L47
- Abraham, R. G., & van den Bergh, S. 2001, *Science*, 293, 1273
- Akritas, M. G., & Bershad, M. A. 1996, *ApJ*, 470, 706
- Balland, C., & Blanchard, A. 1997, *ApJ*, 487, 33
- Balogh, M. L., Baldry, I. K., Nichol, R., et al. 2004, *ApJL*, 615, L101
- Barkhouse, W. A., Yee, H. K. C., & López-Cruz, O. 2007, *ApJ*, 671, 1471
- . 2009, *ApJ*, 703, 2024
- Bartelmann, M. 1996, *A&A*, 313, 697
- Bechtold, J., Yee, H. K. C., Elston, R., & Ellingson, E. 1997, *ApJL*, 477, L29
- Beijersbergen, M., Hoekstra, H., van Dokkum, P. G., & van der Hulst, T. 2002, *MNRAS*, 329, 385
- Benítez, N. 2000, *ApJ*, 536, 571
- Benítez, N., Ford, H., Bouwens, R., et al. 2004, *ApJS*, 150, 1
- Bentley, & Louis, J. 1975, *Commun. ACM*, 18, 509
- Bertin, E. 2006, in *ASP Conference Series*, Vol. 351, *Astronomical Data Analysis Software and Systems XV*, ed. C. Gabriel, C. Arviset, D. Ponz, & S. Enrique, 112
- Bertin, E. 2010a, *SCAMP v1.9 User's manual*
- . 2010b, *SExtractor v2.13 User's manual*, IAP
- . 2010c, *SWarp v2.21 User's guide*, IAP
- Bertin, E., & Arnouts, S. 1996, *A&As*, 117, 393
- Bertin, E., Mellier, Y., Radovich, M., et al. 2002, in *ASP Conference Series*, Vol. 281, *Astronomical Data Analysis Software and Systems XI*, ed. D. A. Bohlender, D. Durand, & T. H. Handley, 228

- Binggeli, B., Sandage, A., & Tammann, G. A. 1988, *ARA&A*, 26, 509
- Blanton, M. R., & Roweis, S. 2007, *AJ*, 133, 734
- Blanton, M. R., Dalcanton, J., Eisenstein, D., et al. 2001, *AJ*, 121, 2358
- Brinchmann, J., Charlot, S., White, S. D. M., et al. 2004, *MNRAS*, 351, 1151
- Bruzual, G., & Charlot, S. 2003, *MNRAS*, 344, 1000
- Butcher, H., & Oemler, Jr., A. 1978, *ApJ*, 219, 18
- Caldwell, N., & Rose, J. A. 1997, *AJ*, 113, 492
- . 1998, *AJ*, 115, 1423
- Canadian Astronomy Data Centre. 2015, MegaPipe image stacking pipeline, <http://www4.cadc-ccda.hia-ihp.nrc-cnrc.gc.ca/en/megapipeline/docs/filt.html>, accessed: 03-27-15
- Carlberg, R. G. 1984, *ApJ*, 286, 403
- Carroll, B. W., & Ostlie, D. A. 2006, *An introduction to modern astrophysics and cosmology*
- Chilingarian, I. V., Melchior, A.-L., & Zolotukhin, I. Y. 2010, *MNRAS*, 405, 1409
- Chilingarian, I. V., & Zolotukhin, I. Y. 2012, *MNRAS*, 419, 1727
- Coe, D., Benítez, N., Sánchez, S. F., et al. 2006, *AJ*, 132, 926
- Cole, S., & Lacey, C. 1996, *MNRAS*, 281, 716
- Csabai, I., Dobos, L., Trencsényi, M., et al. 2007, *Astronomische Nachrichten*, 328, 852
- Dahlén, T., Fransson, C., & Näslund, M. 2002, *MNRAS*, 330, 167
- Demarco, R., Wilson, G., Muzzin, A., et al. 2010, *ApJ*, 711, 1185
- Dobos, L., Csabai, I., Yip, C.-W., et al. 2012, *MNRAS*, 420, 1217
- Dressler, A. 1980, *ApJ*, 236, 351
- . 1984, *ARA&A*, 22, 185
- Dressler, A., & Gunn, J. E. 1983, *ApJ*, 270, 7
- Dressler, A., Smail, I., Poggianti, B. M., et al. 1999, *ApJs*, 122, 51
- Dressler, A., Oemler, Jr., A., Couch, W. J., et al. 1997, *ApJ*, 490, 577
- Dubois, Y., Gavazzi, R., Peirani, S., & Silk, J. 2013, *MNRAS*, 433, 3297

Ebeling, H., Edge, A. C., Bohringer, H., et al. 1998, MNRAS, 301, 881

Eddington, A. S. 1913, MNRAS, 73, 359

Efron, B. 1979, Ann. Statist., 7, 1

Ellingson, E., Lin, H., Yee, H. K. C., & Carlberg, R. G. 2001, ApJ, 547, 609

Ferguson, H. C., & Binggeli, B. 1994, A&ARv, 6, 67

Ferguson, H. C., & Sandage, A. 1989, ApJl, 346, L53

Forman, W., & Jones, C. 1982, ARA&A, 20, 547

Friedman, H., J., Bentley, et al. 1977, ACM Trans. Math. Softw., 3, 209

Fukugita, M., Shimasaku, K., & Ichikawa, T. 1995, PASP, 107, 945

Gunn, J. E., & Gott, III, J. R. 1972, ApJ, 176, 1

Haines, C. P., Barbera, F. L., Mercurio, A., Merluzzi, P., & Busarello, G. 2006, ApJ, 647, L21

Hammer, D. M. 2012, PhD thesis, The Johns Hopkins University

Hammer, D. M., Hornschemeier, A. E., Salim, S., et al. 2012, ApJ, 745, 177

Hester, J. A., Seibert, M., Neill, J. D., et al. 2010, ApJL, 716, L14

Hogg, D. W. 1999, ArXiv Astrophysics e-prints, astro-ph/9905116

Holwerda, B. W. 2005, ArXiv Astrophysics e-prints, astro-ph/0512139

Hubble, E. P. 1925, ApJ, 62, 409

—. 1929, Proceedings of the National Academy of Science, 15, 168

Hubble, E. P., & Humason, M. L. 1931, ApJ, 74, 43

Jedrzejewski, R. I. 1987, MNRAS, 226, 747

Kenney, J. D. P., Geha, M., Jáchym, P., et al. 2014, ApJ, 780, 119

Kennicutt, R. C. 1998, ARA&A, 36, 189

Kodama, T., & Arimoto, N. 1997, A&A, 320, 41

Kormendy, J., & Kennicutt, Jr., R. C. 2004, ARA&A, 42, 603

Kotulla, R., Fritze, U., Weilbacher, P., & Anders, P. 2009, MNRAS, 396, 462

Kowalski, A. F., Hawley, S. L., Hilton, E. J., et al. 2009, AJ, 138, 633

- Kravtsov, A. V., & Borgani, S. 2012, *ARA&A*, 50, 353
- Larson, R. B., & Tinsley, B. M. 1978, *ApJ*, 219, 46
- Larson, R. B., Tinsley, B. M., & Caldwell, C. N. 1980, *ApJ*, 237, 692
- Lawrence, A., Warren, S. J., Almaini, O., et al. 2007, *MNRAS*, 379, 1599
- Lin, D. N. C., & Faber, S. M. 1983, *ApJL*, 266, L21
- Lisker, T., Grebel, E. K., & Binggeli, B. 2006, *AJ*, 132, 497
- López-Cruz, O. 1997, PhD thesis, Department of Astronomy and Astrophysics, University of Toronto
- López-Cruz, O., Barkhouse, W. A., & Yee, H. K. C. 2004, *ApJ*, 614, 679
- Marquardt, D. W. 1963, *SIAM Journal on Applied Mathematics*, 11, 431
- Martel, H., Barai, P., & Brito, W. 2012, *ApJ*, 757, 48
- Martin, C. L., Lotz, J., & Ferguson, H. 2000, *ApJ*, 543, 97
- McGee, S. L., Balogh, M. L., Bower, R. G., Font, A. S., & McCarthy, I. G. 2009, *MNRAS*, 400, 937
- McKee, C. F., & Ostriker, E. C. 2007, *ARA&A*, 45, 565
- Merten, J., Meneghetti, M., Postman, M., et al. 2014, *ArXiv Astrophysics e-prints*, astro-ph/1404.1376
- Moffat, A. F. J. 1969, *A&A*, 3, 455
- Moore, B., Katz, N., Lake, G., Dressler, A., & Oemler, A. 1996, *Nature*, 379, 613
- Navarro, J. F., Frenk, C. S., & White, S. D. M. 1995, *MNRAS*, 275, 720
- Oegerle, W. R., & Hill, J. M. 2001, *AJ*, 122, 2858
- Peng, Y., Maiolino, R., & Cochrane, R. 2015, *Nature*, 521, 192
- Popesso, P., Biviano, A., Böhringer, H., & Romaniello, M. 2006, *A&A*, 445, 29
- . 2007, *A&A*, 461, 397
- Postman, M., Coe, D., Benítez, N., et al. 2012, *ApJS*, 199, 25
- Press, W. H., & Schechter, P. 1974, *ApJ*, 187, 425
- Quadri, R. F., Williams, R. J., Franx, M., & Hildebrandt, H. 2012, *ApJ*, 744, 88
- Quilis, V., Moore, B., & Bower, R. 2000, *Science*, 288, 1617



Rines, K., Geller, M. J., Diaferio, A., & Kurtz, M. J. 2013, *ApJ*, 767, 15

Rozo, E., Rykoff, E., Koester, B., et al. 2011, *ApJ*, 740, 53

Rozo, E., Rykoff, E. S., Koester, B. P., et al. 2009, *ApJ*, 703, 601

Rykoff, E. S., Koester, B. P., Rozo, E., et al. 2012, *ApJ*, 746, 178

Salim, S. 2014, *Serbian Astronomical Journal*, 189, 1

Sandage, A., & Binggeli, B. 1984, *AJ*, 89, 919

Schechter, P. 1976, *ApJ*, 203, 297

Schlegel, D. J., Finkbeiner, D. P., & Davis, M. 1998, *ApJ*, 500, 525

Stoughton, C., Lupton, R. H., Bernardi, M., et al. 2002, *AJ*, 123, 485

Struble, M. F., & Rood, H. J. 1999, *ApJS*, 125, 35

The Sloan Digital Sky Survey. 2015, Measurements of Flux and Magnitude — SDSS-III DR12, <http://www.sdss.org/dr12/algorithms/magnitudes>, accessed: 04-06-15

Thompson, L. A., & Gregory, S. A. 1980, *ApJ*, 242, 1

—. 1993, *AJ*, 106, 2197

Tinsley, B. M. 1980, *FCPh*, 5, 287

Tonnesen, S., Bryan, G. L., & van Gorkom, J. H. 2007, *ApJ*, 671, 1434

Tovmassian, H. M., & Andernach, H. 2012, *MNRAS*, 427, 2047

Vader, J. P., & Sandage, A. 1991, *ApJl*, 379, L1

Williams, R. E., Blacker, B., Dickinson, M., et al. 1996, *AJ*, 112, 1335

Yee, H. K. C. 1991, *PASP*, 103, 396

Yee, H. K. C., Ellingson, E., & Carlberg, R. G. 1996, *ApJs*, 102, 269

Zwicky, F. 1933, *Helvetica Physica Acta*, 6, 110